

COUPLING OPTICAL AND THERMAL DIRECTIONAL RADIATIVE
TRANSFER TO BIOPHYSICAL PROCESSES IN VEGETATED CANOPIES

Joris Timmermans

Examining committee:

Prof. Dr. F.D. van der Meer
Prof. Dr. A.K. Skidmore
Prof. Dr. J.-P. Gastellu Etchegorry
Prof. Dr. M. Menenti
Prof. Dr. H. Dolman
Dr. L. Jia

University of Twente
University of Twente
CESBIO
University of Delft
University of Wageningen
University of Wageningen



ITC dissertation number 192
ITC, P.O. Box 6, 7500 AA Enschede, the Netherlands

ISBN 978-90-6164-313-5
Cover designed by Benno Masselink
Printed by ITC Printing Department
Copyright © 2011 by Joris Timmermans

COUPLING OPTICAL AND THERMAL DIRECTIONAL RADIATIVE
TRANSFER TO BIOPHYSICAL PROCESSES IN VEGETATED CANOPIES

DISSERTATION

to obtain
the degree of doctor at the University of Twente,
on the authority of the Rector Magnificus,
Prof.dr. H. Brinksma,
on account of the decision of the graduation committee,
to be publicly defended
on Wednesday 06 July 2011 at 1445 hrs

by

Joris Timmermans

born on 12-01-1979

in Nijmegen, the Netherlands

This thesis is approved by
Prof. Dr. Ir. Zhongbo (Bob) Su, promotor
Prof. Dr. Ing. Wouter Verhoef promotor
Dr. Ir. Christiaan van der Tol, assistant promotor.

Preface

The road culminating in this thesis was neither straight nor flat. It greatly influenced my professional and personal life, and has shaped me into the research street fighter I am today. It all started when I was graduating from Montessori primary school in Nijmegen. At that point I was diagnosed as a below-average student and given the advice to follow the easiest educational track available in the Netherlands, 'individueel beroepsonderwijs' (vocational training). What my teachers however failed to recognize was that I had a strong form of dyslexia. Fortunately my parents were convinced that I could do much better and had me tested at the University of Nijmegen. The results showed that I should be able to perform at the schooling level of 'Voorbereidend Wetenschappelijk Onderzoek (VWO)' needed for university entry.

Secondary school at the Canisius College Mater Dei gave me the opportunity to start my academic education. I showed a knack for the exact sciences, as may be expected with a loving father who teaches physics and maths. Although linguistics was still very hard for me, the remedial teaching by Rini Leunissen as well as many painstaking hours of study saw me improving step by step.

My education was interrupted in 1994 due to declining health. My asthma had reached a critical level that could not be cured in the Netherlands. Fortunately I was given the opportunity to stay at the Dutch Asthma Centre Davos (in Switzerland for three months). This place provided the clean air needed for my recuperation, as well as instruction in how to accept and live with my asthma, and the chance to explore ones limits. While I had all the help, physically and mentally, one could wish for, they were not accredited to teach at VWO level. Therefore, my teachers at home faxed instructions and examinations to me every week. Although distractions were plenty (like learning to ski), numerous telephone calls with my father reduced the set-backs so that I could still finish the year and subsequently secondary school successfully.

After completing secondary school I struggled to find a study that suited me, as my interests were (and are) (too) many. Finally I decided to pursue the study of applied physics at the technical University of Twente (UT), mainly because physics forms the universal building blocks for everything, and I am interested in everything). Although I started off badly, passing few exams, I finally found my feet after about half a year. During the study I rediscovered my interest in space science which brought me to the Physics of Fluids department of Detlef Lohse. Here Gerrit de Bruin arranged an

internship at the Von Karman Institute, Belgium. The work I did for the Ariane 5 Space program confirmed that performing research in space science was the career I wanted. However, what I had in mind was not possible at the time at the Physics of Fluids group, where I finished my thesis on the dynamics of micro bubbles under the influence of ultrasound forcing.

Still full of ambition to pursue a career in space science I was fortunate to have Bob Su, my promoter at the ITC, provide me with the chance to prove myself in the NWO-SRON project on remote sensing and radiative transfer. Although it was hard for me at the start, due to the differences between remote sensing research and physics of fluids research (remote sensing dealing with more real-life problems), Ambro Gieske, my first supervisor, and later on Wout Verhoef, guided me through this period. In the summer of 2007, through another unwanted twist of events, I ended up in hospital with acute anaphylactic shock. The realisation of the immediate threat I had faced hit me later with the sudden death of my good friend, Dan Omolo, due to heart failure. Fighting these unwanted and unexpected twists of fate has finally led to the creation of this dissertation.

All of the setbacks showed me that not only should we fight for the things we want, but we should also enjoy the path they take us, even though this might involve some unexpected turns.

Acknowledgements

The research described in this thesis was supported by the Netherlands Institute for Space Research (SRON), which is financed by the Netherlands Organisation for Scientific Research (NWO). The research was carried out at the Water Resources (WRS) department of the Faculty for Geoinformation Sciences and Earth Observation (ITC) at the University of Twente (UT). I gratefully acknowledge the support of these institutions for their financial contributions.

During the years I performed my PhD research I worked together with a lot of people within and outside the institute, and I could not have completed this research without their continuous support. I therefore would like to thank all these people, as well as the following people in particular:

First of all I would like to thank my promoters Bob Su and Wout Verhoef, and “my Postdoc” Christiaan van der Tol for sharing their knowledge on evapotranspiration and radiative transfer. I would also like to thank them for their patience during the numerous discussions at the ITC and at the different workshops, such as the 1st Dragon Workshop in Beijing.

During this research field campaigns have been undertaken and papers have been published. The massive acquisition of data to be used in the different papers could not have been accomplished without the immense help of Ambro Gieske prior to the 2005 SEN2FLEX campaign in Spain, and of Wim Timmermans, who organised the 2006 EAGLE in the Netherlands. In their support for a nice readable manuscript I would like to acknowledge Eva Skidmore (English writing) and Dolly Heitman (stereo-photography of the cover).

I would also like to thank my countless roommates: Rogier van de Velde, Marcel van Helvoirt, Xuelong Chen, Mireia Romaguera, Changbo Qin, Jennifer Kinoti, Mohammad Abouali, and Laura Oosterhold. During the creation of the SCOPE model and several other algorithms my loud typing and “heated” arguments with my computer must have been quite bothersome at times. I would like to apologize for this and thank you very much for your patience and advice with the programming.

In addition, I would like to thank my sailing friends: Ivo Heitman, Sabine ter Berge, Anita Bouma, Rogier Oudshoorn, David Elsing, Nelleke Beerman, Freark van der Bos; my roommates: Tom Hesta,

Anouk Vorselman, Lea Goedhart, Tiemon Dokter, Wilma de Groot; my ITC buddies: Dan Omolo (you are sorely missed), Mila Luleva, Juan Fransisco Sanchez, Juan Pablo (Jipi) Ardila Lopez, Sabrina Carvalho, Nick Hamm (and the rest of the PhD community); and all my hockey friends (too numerous to name), for all their friendship.

I would like to give special thanks my family. My parents, Piet and Jeanette, who have given me their love and support over the years, which has given me the confidence to believe in myself and to keep fighting when the setbacks were bigger than I expected. It cannot be a coincidence that your four children all have pursued (or are pursuing) a doctorate degree: my older sister Anne, who has been an inspiration, although I do not show it all the time; my (three minutes!) younger sister Sarah, whom I could always call for mental support; and finally my little brother Lucas, who has taught me to take life a little bit less seriously.

Finally, I would also like to thank my girlfriend Ingrid for her continuous love and patience. You tease me when I am down, you cheer me up when I am sad, you massage me when I am injured again through hockey, and put me in my place when I am too cocky ;-). You make me complete!

Joris Timmermans
2010.

Table of Contents

Preface	i
Acknowledgements	iii
Table of Contents	v
1 Introduction	1
1.1 Biophysical vegetation processes	2
1.1.1 Biophysical process modelling	2
1.2 Vegetation radiative transfer	4
1.2.1 Radiative transfer models	6
1.3 Research Objective	8
1.4 Structure of this thesis	9
2 Experimental Setup	11
2.1 Introduction	12
2.2 Original Goniometric Setup	13
2.2.1 Improvements	14
2.2.2 Automated Control	15
2.2.3 Viewing Angles	15
2.2.4 Operational calibration	15
2.2.5 Sensors	16
2.3 Contact measurements	17
2.4 Field sites	18
2.4.1 SEN2FLEX	20
2.4.2 EAGLE	21
2.4.3 AGRISAR	22
2.5 Results and Discussion	24
2.5.1 Reflectance variation in different grass canopies	25
2.5.2 Reflectance variation in different maize canopies	27
2.5.3 Directional variation in different crop types	27
2.6 Conclusions and outlook	29
3 Identification of Land surface components	30
3.1 Introduction	31
3.2 Methodology	32
3.2.1 Directional radiative signatures	33
3.2.2 Land surface components identification	35
3.2.3 Component brightness temperature extraction	35
3.3 Results	37
3.3.1 Directional radiative signatures	37
3.3.2 Land surface component skin temperatures	38
3.3.3 Extraction of component temperatures	40
3.4 Discussion	42
3.5 Conclusion	43
4 The SCOPE model	45
4.1 Introduction	46

4.2	Model description	47
4.2.1	Atmospheric optical inputs.....	49
4.2.2	Direct and diffuse radiation fluxes.....	49
4.2.3	Internally generated thermal radiation	51
4.2.4	Net radiation	53
4.2.5	The energy balance	53
4.2.6	Leaf biochemistry	55
4.2.7	Top of canopy radiance spectra	56
4.3	Output of SCOPE	57
4.3.1	Spectra.....	57
4.3.2	Directional radiance.....	59
4.3.3	Vertical profiles.....	61
4.4	Discussion and Conclusion	62
5	Validation of radiative transfer in SCOPE.....	65
5.1	Introduction.....	66
5.2	Methodology.....	68
5.2.1	Laser scanning.....	70
5.2.2	SAIL.....	72
5.2.3	DART.....	72
5.2.4	Simulation Parameters	73
5.3	Results.....	76
5.3.1	Structural parameter retrieval.....	76
5.3.2	SCOPE and SLC comparison.....	78
5.3.3	BRDFs of SCOPE, SLC and DART.....	79
5.3.4	DART scenarios, a comparison	82
5.3.5	DART and SCOPE, a comparison.....	86
5.3.6	DART and SLC, a comparison.....	89
5.4	Conclusion.....	92
6	Retrieval of skin temperatures from directional observations	95
6.1	Introduction.....	96
6.2	Methodology	97
6.2.1	Traditional retrieval algorithms.....	98
6.2.2	Sensitivity analysis	101
6.2.3	Field measurements	107
6.3	Results.....	107
6.3.1	Sensitivity study	107
6.3.2	Inversion of goniometric measurements	110
6.4	Conclusion.....	114
7	Applying SCOPE for SEBS evaluation.....	116
7.1	Introduction.....	117
7.1.1	Methodology.....	119
7.1.2	Surface Energy Balance.....	120
7.1.3	Evaporative Fraction	122
7.2	Experimental Setup	122
7.3	Results.....	123

7.3.1	Roughness heights	123
7.3.2	Instantaneous heat fluxes	126
7.3.3	Evaporative fraction.....	128
7.4	Conclusions	130
8	Concluding Remarks	133
8.1	Synthesis	133
8.2	Field measurements.....	134
8.3	Modelling.....	135
8.4	Validation	135
8.5	Applications	136
8.6	Limitations	138
8.7	Related to the Objectives	139
8.8	Outlook.....	139
9	Bibliography	141
10	Summary	157
11	Samenvatting.....	160
12	ITC Dissertation List	161

1 Introduction

Remote sensing of biophysical processes is rapidly developing into a very important tool for extending the knowledge of the earth's biosphere. Knowledge about biophysical processes is very important for a wide range of applications, such as weather forecasting (Wetzel and Chang, 1988; Choudhury, 2000), climate change monitoring (Destouni *et al.*, 2009) and irrigation management (Allen *et al.*, 1998). Because of the large scale of such applications, field measurement, of the interactions, like FLUXNET (Baldocchi *et al.*, 2001), can not be used

Remote sensing is probably the only tool that can provide measurements at regional to continental scales. Using orbiting satellites, radiation measurements at the top of the atmosphere (TOA) are acquired with different temporal, spatial and spectral resolutions as well as sometimes observations with different viewing angles.

The problem with remote sensing is that the physical process of interest cannot always be measured using radiation alone. In the majority of cases only indirect relationships between the observed radiation and the biophysical processes exist. Remote sensing algorithms therefore use biophysical parameters, like leaf area index (LAI), albedo and fractional vegetation cover (f_c). However, in many cases these parameters are retrieved using only a fraction of the available data (Sobrino *et al.*, 1994; Gitelson *et al.*, 2007) (limited use of spectral bands, single view nadir observations). Using more detailed spectral and angular information demands the use of a detailed transfer radiative transfer model (RTM).

Over the past years the variety and application of these models have increased significantly (Kuusk, 1998; Wang *et al.*, 2000; Meroni *et al.*, 2004; Tang *et al.*, 2007; Verhoef, 2007). However, these RTMs can not be used to characterize actual biophysical processes like evapotranspiration. Even though Surface-Vegetation-Atmosphere Transfer (SVAT) models (Norman, 1979) exist that allow for such an approach, their low level in terms of radiative transfer modelling limits their applicability with present and future satellites. An integrated model, that combines the detailed simulation of biophysical and biochemical processes with a radiative transfer model, and has the possibility of using directly observed hyperspectral, multidirectional remote sensing observations, does not

exist at present (Glenn *et al.*, 2007; Kalma *et al.*, 2008). This thesis encompasses efforts to develop and evaluate such a model.

1.1 Biophysical vegetation processes

Vegetation processes play a very important role in climate change. Vegetation absorbs net radiation (Babatunde *et al.*, 2009), assimilates carbon dioxide, and feeds water vapour into the atmosphere (Pielke, 2001). Hence it influences the regional and global climate (Seneviratne and Stöckli, 2007) and precipitation patterns (Koster *et al.*, 2000). However, in the past this role has been underestimated (Entekhabi *et al.*, 1999) because the land surface was only considered to be a sink term for the water and carbon cycle. However land cover should be viewed as an active component (Easterling *et al.*, 2000; Seneviratne and Stöckli, 2007). It has even been reported (IPCC report 2001) that the effects of land cover change on the climate may be larger than the effect of atmosphere composition change. The impact of biophysical processes on the water, carbon and energy cycle should therefore be investigated further.

Among all processes involving vegetation, photosynthesis and transpiration are the most important ones for climate change. Photosynthesis assimilates carbon dioxide from the atmosphere (Farquhar *et al.*, 1980) to glucose, and transpiration controls the transfer of water vapour from the soil through the vegetation to the atmosphere (Monteith, 1973). These two processes cannot be separated because of the control that the stomatal pores (Figure 1-1) have on the exchange of carbon dioxide, water vapour, and water stress (Yin and van Laar, 2005). The leaf photosynthetic rate is affected by leaf temperature (Leuning, 1995), which in itself is controlled by the cooling effect of transpiration.

1.1.1 Biophysical process modelling

Several attempts have been made to parameterize the interactions between the land surface and the atmosphere (Olioso *et al.*, 1999), creating crop growth models, remote sensing algorithms and Soil-Vegetation-Atmosphere Transfer (SVAT) models. Crop Growth models, such as GECROS (Yin and van Laar, 2005), are designed to estimate crop growth based on environmental impact and management practices as well as physiological descriptions. They are too complex for any regional application, because of the large number

of input variables required and the computational demands of such a model.

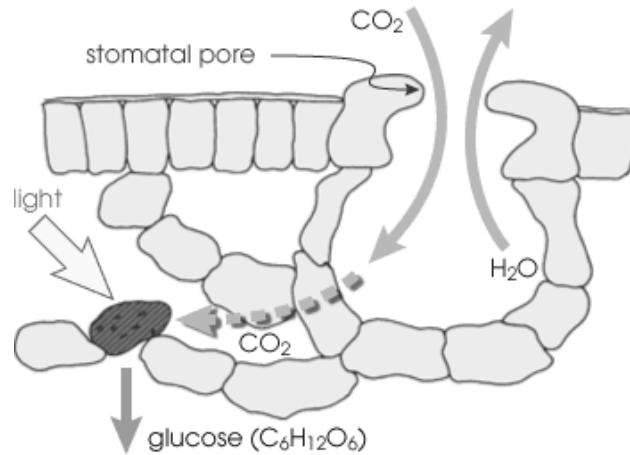


Figure 1-1: Stomatal control of photosynthesis and transpiration.

Remote Sensing algorithms

Remote Sensing (RS) algorithms are widely used to estimate land surface fluxes such as net radiation, ground heat flux, sensible heat, and latent heat. Traditionally these remote sensing algorithms, *e.g.* SEBS (Su, 2002) and SEBAL (Bastiaanssen *et al.*, 1998), require a limited number of bio-geophysical input variables to characterize the land surface processes. These input parameters, such as emissivity, LAI , and f_c , are estimated *a priori* based on single view (nadir) observations (Sobrino *et al.*, 1994; Knyazikhin *et al.*, 1998b; Jimenez-Munoz *et al.*, 2006), assuming the land surface is homogeneous.

However, the pixel sizes of the commonly used satellite sensors, such as the Advanced Along Track Radiometer (AATSR), the Moderate-Resolution Imaging Spectroradiometer (MODIS), and Landsat-TM, are larger than the characteristic length of the surface processes and consequently the biophysical parameters are aggregates of their sub-pixel components (Gowda *et al.*, 2007). For example, the SEBS model does not distinguish between soil and vegetation and hence can only estimate evapotranspiration (the sum of evaporation in canopy and soil, and transpiration in the canopy). Hence such RS algorithms oversimplify both the radiative and the biophysical processes. More complex RS models, such as the Two Source Energy Balance (TSEB) model (Norman *et al.*, 1995; Kustas and Norman, 1999) and Alexi

(Anderson *et al.*, 2008), have been developed in order to distinguish between these two components. However, these more complex models still parameterize vegetation as a single slab, and therefore aggregation effects still affect the estimation of land-surface interaction.

SVAT models

SVAT models explicitly model the coupled transport of radiation, heat and carbon through the canopy (Sellers *et al.*, 1997; Verhoef and Allen, 2000; Brunsell and Gillies, 2003; Tuzet *et al.*, 2003). Unlike crop growth models (Yin and van Laar, 2005) they do not take carbon storage or other physiological characteristics of the vegetation into account and are hence slightly less complex. SVAT models therefore form an intermediate approach for estimating photosynthesis and transpiration. Although this intermediate approach should provide a nice balance between detail and large scale application, the use of remote sensing data is hampered by the simplified treatment of radiative transfer within these models. The CUPID (Norman, 1979; Kustas *et al.*, 2007) model was the first to implement a reasonable description of radiative transfer, however it does not use hyper/multi spectral information and only distinguishes between VIS, NIR and TIR radiation. As the canopy spectral reflectance depends on the different biophysical and biochemical components (Asner, 1998), such SVAT models cannot be used directly for the extraction of biophysical parameters from optical remote sensing.

1.2 Vegetation radiative transfer

In addition to the spectral signature of the land surface, four other reflectance signature types can be distinguished (Gerstl, 1990): spatial signatures, angular signatures, temporal signatures and polarization signatures. Of these signatures only the spectral and angular signatures can be used for the retrieval of biophysical parameters using passive remote sensing.

Spectral signatures of the vegetation are primarily a function of leaf optical properties (Jacquemoud *et al.*, 1996), canopy biophysical attributes and soil spectral reflectance (Asner, 1998; Milton *et al.*, 2009). This is illustrated in Figure 1-2A, where the increase in LAI determines the influence of leaf and soil reflectance on the canopy spectral reflectance.

Angular signatures in the optical part of the spectrum, usually calculated as the Bi-directional Reflectance Distribution Function

(BRDF), arise because the land surface is a strong anisotropic reflector of optical radiation (Liang *et al.*, 2000). This creates effects in the surface reflectance such as the hotspot effect (as illustrated in Figure 1-2B). In addition these surfaces also display a strong directional thermal signature due to the distribution of temperatures and emissivities between the different vegetation components, like soil and vegetation (Menenti *et al.*, 2008).

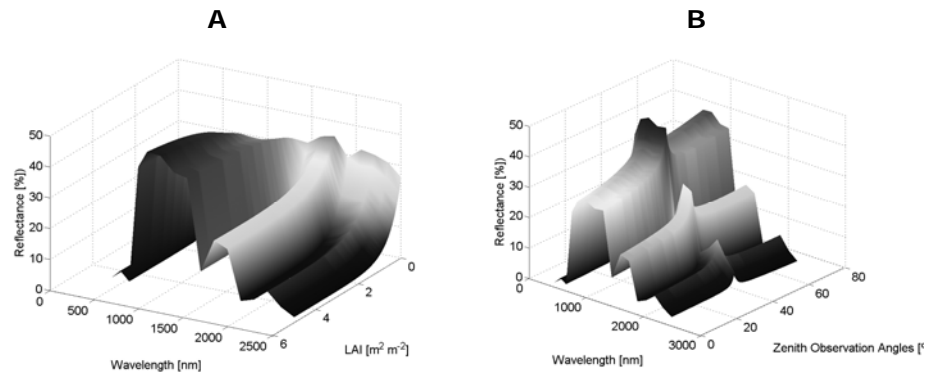


Figure 1-2: Canopy reflectance dependence. In panel A the reflectance dependence for different wavelengths and LAI is shown. In panel B the reflectance dependence for different wavelengths and the observation angles is shown. Both figures are simulations from the Scattering of Arbitrary Inclined Leaves (SAIL) model.

The anisotropic effects can be divided into three classes (Strahler, 1997), which can be modelled using Radiative Transfer Models (RTM). These classes are: specular scattering and shadowing effects, usually arising for sparse vegetation; volume scattering of the aggregated canopy elements, which is important in dense vegetation; and the so called the hotspot effect, which in vegetation is caused by shadowing and in soil caused by coherent superposition of scattered incident radiation (Hapke, 1981). As each of these process classes influences the directional behaviour of exiting radiation in a unique way, inversion of these RTMs is used in multi-angular remote sensing to retrieve biophysical parameters at sub-pixel scale (Widlowski, 2001; Milton *et al.*, 2009).

However, the accuracy of estimations using such physical methods is highly sensitive to agreement of the model parameters with the actual parameters (Widlowski *et al.*, 2007). This implies that although complex models, like discrete anisotropic radiative transfer (DART) (GastelluEtchegorry *et al.*, 1996; Gastellu-Etchegorry *et al.*, 2004;

Gastellu-Etchegorry, 2008), may be more accurate, the need for a high number of detailed (structural) parameters limits their applicability in comparison with medium complexity models such as Scattering of Arbitrary Inclined Leaves (SAIL) (Verhoef, 1984; Verhoef and Bach, 2003; Verhoef *et al.*, 2007). The choice for a RTM consequently depends on the constraints posed by the application.

1.2.1 Radiative transfer models

The radiative transfer theory for modelling canopy scattering was introduced by (Suits, 1972). Since then a large array of radiative transfer models has been created. Each of these models differs both in modelling terms (analytical and numerical) and in degree of complexity.

Analytical models, such as the SAIL model (Verhoef, 1984), describe the surface as a number of infinitely extended layers of a turbid medium (Figure 1-3). This turbid medium approach has been widely used (Verhoef, 1984; Qin and Liang, 2000; Meroni *et al.*, 2004) due to the modelling effectiveness of photon transport. Analytical models are fast and easy to implement but may have larger uncertainties for more complex 3D canopies.

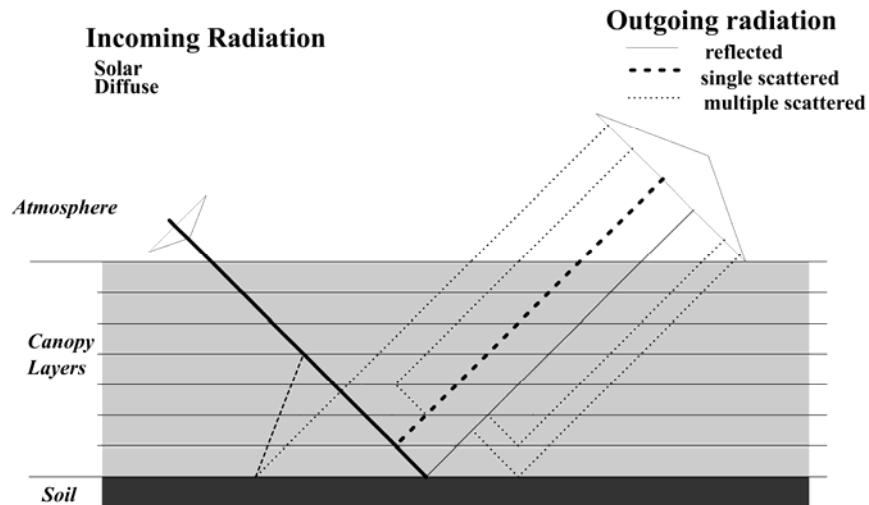


Figure 1-3: Analytical radiative transfer in a turbid medium.

Complex numerical models, such as Radiosity (Liu *et al.*, 2007a) and DART (Gastellu-Etchegorry *et al.*, 2004), are able to simulate the radiative transfer of three dimensional scenes, using the detailed

information on spatial variability of the land cover, and the path of (individual) photons through this scene. Scenes are built with large amounts of cells, each with their own phase function (Figure 1-4). Therefore these models are in general computationally very demanding, as each cell has its own interaction with the cell's entering rays.

In general the (analytical and numerical) models perform similarly for 1D vegetation types (Pinty *et al.*, 2001) but display significant differences for more complex 3D land covers (Pinty *et al.*, 2004). In general the accuracy of an estimation using RTMs is highly sensitive to agreement of the model parameters with the actual parameters (Widlowski *et al.*, 2007). The choice for a RTM consequently depends on the constraints posed by the application. Especially if the model needs to be inverted, a faster RTM with relatively few input parameters is preferable. The larger the amount of variables that needs to be retrieved, the larger the amount of independent observation data necessary for the accurate retrieval of these variables (Verhoef, 2008). This is called the ill-posedness of the inversion problem.

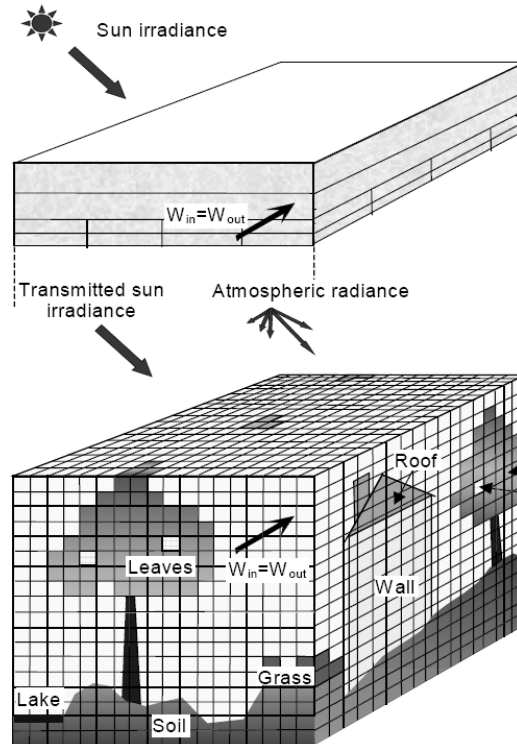


Figure 1-4: DART scene construction with different cell types.

1.3 Research Objective

The problem with highly accurate estimations of surface-atmosphere processes is that current SVAT models oversimplify the radiative transfer within the canopy and radiative transfer models are only used to estimate biophysical parameters, but not the process itself. Combining a detailed RTM and a biophysical/biochemical model will enable direct estimation of the processes. This will result in a reduction of uncertainties in the estimation of photosynthesis and evapotranspiration. At present only the CUPID model approximates such a combination. Other efforts in this direction were not found.

The objective of this research therefore is to

1. Develop a new SVAT MODEL that integrates directional radiative transfer and complex biophysical/biochemical processes; a model able to estimate the exchange of heat,

water vapour and carbon fluxes at the land-atmosphere interface from remotely observed directional observations.

In order to achieve this objective, several sub-objectives have been defined, as listed below. Each of these objectives is tackled in the corresponding chapters.

2. Acquisition of a complete database with both directional observations and measurements of heat, water vapour and carbon fluxes over different land surface types.
3. Investigation of the directional behaviour of reflection and emission in different canopies.
4. Creation of a detailed SVAT model that combines radiative transfer model with a detailed biophysical/biochemical model.
5. Evaluation of both components of the new SVAT model. The evaluation needs to be performed separately for both the radiative transfer model and the biophysical/biochemical model component, using forward simulations and field measurements.
6. Investigation into the retrieval capability of the SVAT model for estimating the biophysical processes. This will be performed by inversion of the new model using multi-directional radiative measurements.
7. Evaluation of the SVAT model using model inter-comparison with a remote sensing algorithm.

1.4 Structure of this thesis

The research described in this thesis follows the objectives noted above. Each of the objectives is discussed in its own chapter. These chapters are all based on peer reviewed papers, which either have been published or submitted.

The acquisition of the datasets will be described in the second chapter. Both the experimental setup for the acquisition of directional radiative observations and the different field campaigns and the various land surface types will be discussed. In the third chapter the "Investigation of the directional behaviour of reflection and emission in different canopies" will be examined using the directional signatures obtained from the field campaigns. In the fourth chapter a detailed description is given of the new SVAT model. The evaluation of the different components is then described in chapter 5. In chapter 6 a retrieval algorithm for the estimation of sub-pixel canopy component temperatures is described. Finally, in chapter 7, the model is compared to a remote sensing algorithm to show the advantage of using the newly created SVAT model.

2 Experimental Setup

Based on

Timmermans, J., Gieske, A.S.M., van der Tol, C., Verhoef, W. and Su, Z. (2009) Automated directional measurement system for the acquisition of thermal radiative measurements of vegetative canopies. In: *Sensors*, 9 (2009)3 pp. 1409-1422.

Abstract

In this chapter the experimental setup for measuring vegetation optical and thermal directional radiative signatures is presented. This experimental setup consisted of a goniometric system upon which several sensors had been placed. In order to reduce dynamical effects the goniometer was modified to run in automated mode for both the zenith and the azimuthal direction. Directional measurements were performed over various crops with different levels of heterogeneity. Concurrently with the directional radiative measurements, contact measurements of the skin temperature were taken. These measurements were used to validate the retrieval of the component temperatures from the directional radiative thermal signatures.

The differences in thermal directional radiative signatures were studied to discover the effects of phenological changes in the different types of vegetation. These measurements were taken during three field campaigns (SEN2FLEX, EAGLE and AGRISAR) and in total covered 8 vegetation types: low and tall grass, young and mature maize, sugar beat, barley, wheat and vineyard. The preliminary results of this study confirmed the potential for automation of the system.

2.1 Introduction

Directional remote sensing has the potential to produce higher accuracy retrieval of surface parameters than nadir-only remote sensing (Verhoef, 2007; Milton *et al.*, 2009). Reduction of signal to noise ratios (SNR) can be achieved by averaging multiple images, and differences in measured spectra for different viewing angles can be exploited (Gobron *et al.*, 2000). (Knyazikhin *et al.*, 1998b) and (Tang *et al.*, 2007) showed how radiation reflected by a sparse canopy varies a great deal between oblique and nadir viewing angles. They were able to take advantage of these directional variations to retrieve the leaf area index with higher precision.

The use of optical directional imagery requires the knowledge of reflectance factors (Bruegge *et al.*, 2000; (Malenovsky *et al.*, 2008) such as the hemispherical-directional reflectance factor (HDRF) and the Bi-directional reflectance factor (BRDF). Analogous to research on optical directional signatures, proof was given that vegetation also displays a thermal directional signature (Martonchik *et al.*, 2000). A dataset with both optical and directional radiative measurements over vegetated surfaces however does not exist at present.

Directional viewing of the ground can be achieved using a goniometer (Li *et al.*, 2004; Schopfer *et al.*, 2008). Sensors such as field spectrometers (Devices, 2000), and thermal radiometers (Legrand *et al.*, 2000) can be attached to such a goniometer. A difficulty with most of the present goniometric setups is that they are non-automated and their operation is tedious and time-consuming. This causes a lot of problems when measuring thermal directional signatures.

One of the most important boundary conditions for directional thermal observations is the time constraint. Thermal characteristics of vegetation are influenced by dynamic (Giorgi and Avissar, 1997) and spatial (McCabe *et al.*, 2008) effects. The dynamic effects consist of changing environmental parameters, such as light intensity, sun angle and wind speed (Su *et al.*, 2008). As surface temperature is one of the dominant parameters in land surface dynamics (Yin and van Laar, 2005) a change in the underlying processes will directly have an impact on the accuracy of the measurement of the temperature. In order to reduce the dynamic effects during measurements, the directional thermal measurements need to be acquired in a short time span. To understand the diurnal behaviour of the land surface thermal dynamic processes, directional thermal

measurements need to be acquired at a frequent, e.g. hourly, interval for at least a whole day.

The objective of this chapter is to present a fast methodology for measuring both optical and thermal directional radiative patterns. The goniometric setup was therefore adapted to perform (semi) automatically using a variety of sensors such as a (thermal) camera and various radiometers. In addition to the goniometric experimental setup a cheap method for measuring the skin temperatures of the different land surface components is presented. These measurements are needed for validation of the inversion scheme presented in chapter 5.

2.2 Original Goniometric Setup

A goniometer consists of a rotating arm where upon sensors can be mounted. Some of the goniometers used in the field can only change their zenith viewing angle (Sobrino *et al.*, 2005) while other goniometers also can set their azimuth angle at an arbitrary value. The additional dimension of rotation is either obtained by a moving train (Devices, 2000; Legrand *et al.*, 2000; Li *et al.*, 2004), or by a boom rotating along a fixed elevated point (Schneider *et al.*, 2004).

The advantage of a goniometer that can only change its zenith viewing angle is that the construction does not need to be very robust or heavy. The disadvantage is that the user has to manually move the system to obtain a complete hemispherical coverage. The advantage of a hemispherical system is therefore obvious, although the extra train/boom can make these systems rather heavy.

The goniometer used has the same layout as described in (Li *et al.*, 2004), see Figure 2-1 and Figure 2-2. This system is one of the smallest goniometers available and therefore considered very mobile. As a result, several field sites can be measured at a high frequency, while retaining the option of easily sampling a complete hemisphere. The goniometer consists of two parts: (1) a set of rotating rods, connected to (2) a train that runs on a circular track. The rods are rotated by a motor. The system of rotating rods controls the zenith angle whereas the train controls the azimuth angle. The rail forms two-thirds of a circle. The 120° gap was purposely constructed to reduce the weight of the goniometer.

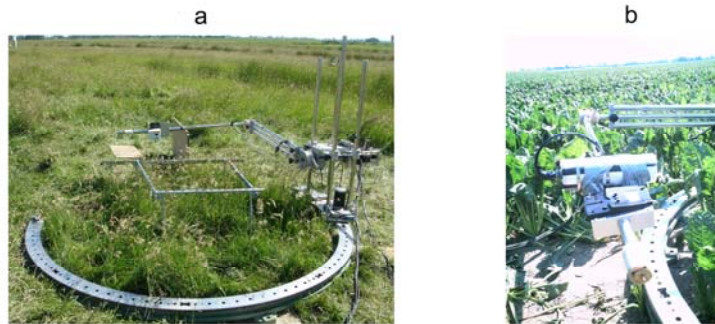


Figure 2-1: Goniometric system over different fields. Panel A shows the goniometer in the grassland (tall) during the EAGLE2006 field campaign, Cabauw (The Netherlands). The goniometer, the Irisys thermal camera and the Everest radiometer are shown. Panel b shows the CIMEL312-1 radiometer attached to the goniometer in the sugar beet field during the AGRISAR2006 field campaign, Görmin (Germany).

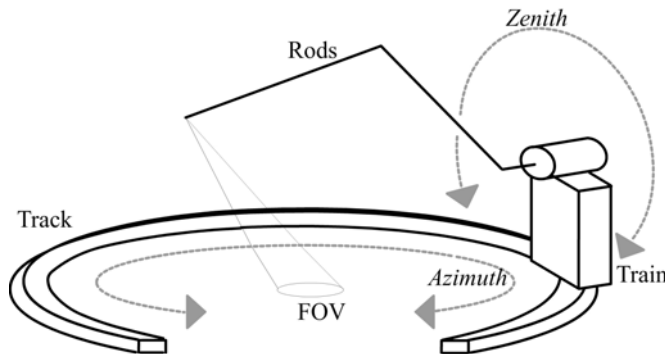


Figure 2-2: Schematic picture of the goniometer.

2.2.1 Improvements

The original goniometer did not have the option of an automated running mode. For each orientation, zenith and azimuth angles had to be measured manually as the instrument did not have a system to calculate the zenith/azimuth viewing angle operationally. The improvements to the original goniometric setup included the controlling of the goniometer by laptop and the operational calibration of the motor positions in relation to the viewing angles.

2.2.2 Automated Control

The goniometer is controlled by a control box with sufficient memory to upload a measuring program. This control box only accepts machine code as input. An algorithm was written to control the positioning of the goniometric system and translate these commands to initiate movement into machine code.

The program allows the user to choose between selecting the viewing angles manually and selecting computer-generated viewing angles (Figure 2-3). Manually selecting the viewing angles is performed by choosing the orientations on a top-down representation of the goniometer. Selecting the viewing angles by computer-generation can be done for random or uniformly separated angles. In the computer-generated method a predefined offset can be included, which can either be a solar angle, or a north orientation.

The program calculates two trajectories for the goniometer. The first trajectory is optimized for the least movement of the arm; the second trajectory is optimized for least movement of the train. As the rotation of the arm is managed by the slowest and weakest motor the arm-optimized trajectory is recommended.

At the selected viewing angle a delay (with user defined duration) is used to give the sensors time to reach equilibrium. At the same time a feedback trigger signal is given to the computer. This trigger can be used to start image acquisition, or to store a timestamp.

2.2.3 Viewing Angles

When performing thermal measurements, a short acquisition time is critical. In order to reduce the duration of a single measurement, 25 viewing angles were chosen (Figure 2-4). The measurement had to be split into two runs as the number of measuring points to be programmed was limited due to the limited memory capacity of the control box. The two runs were programmed with an offset of 45 degrees. The start and end position, and the nadir viewing angle were used to compare changes in temperatures.

2.2.4 Operational calibration

In this study the gap in the track was used to track the position of the train and thus to calibrate the azimuth angle of the

measurement. This is done by running the train from end to end, and recording the number of turns the sprockets had to make. This can be repeated for each run.

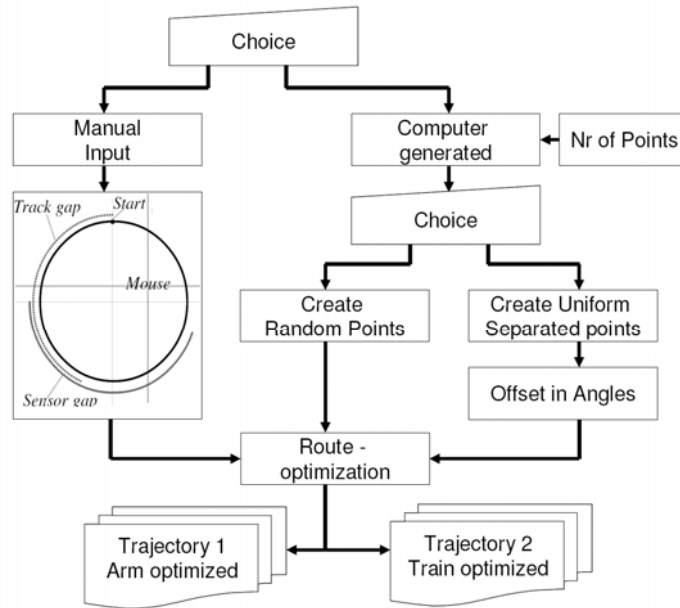


Figure 2-3: Flowchart of the Route-calculation program.

2.2.5 Sensors

A variety of sensors were placed on the goniometer. These sensors varied from multi-spectral instruments (CIMEL (Legrand *et al.*, 2000)) to thermal cameras (Irisys 1010 (Sobrino and Jimenez-Munoz, 2005; Timmermans *et al.*, 2008)). The complete set of thermal instruments used on the goniometer is listed in Table 2-1. In addition to the thermal instruments, a Digital Camera was placed on the goniometer. The only restriction for sensors placed on the goniometer was their weight, as the motor controlling the arm-rotation was not strong.

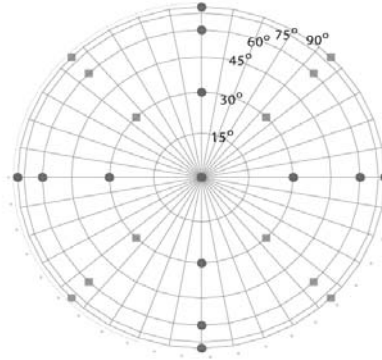


Figure 2-4: Viewing angles of the goniometer (top view). The squares denote the first run and the circles denote the second run.

Table 2-1: Optical and thermal Sensors used on the goniometer.

	Accuracy	Spectral Res.	IFOV (°)	Specifics	
Optical spectrometers					
ASD	0.7 μm	5%	3.0 nm	25	300 Bands
FieldSpec Pro	1.4 μm	5%	8.5 nm		
	2.1 μm	7%	6.5 nm		
GER3700	0.7 μm	5%	1.5 nm	25	704 Bands
	1.4 μm	5%	6.5 nm		
	2.1 μm	7%	9.5nm		
Optical Cameras					
Olympus digital camera	-	-	25	3 MPixels	
Thermal Radiometers					
CIMEL 312-1	± 0.5 K	0.05 K	10	4 Bands	
CIMEL 312-2	± 0.5 K	0.05 K	10	6 Bands	
Everest 3000	± 0.5 K	0.10 K	20	broadband	
Thermal Cameras					
Thermal Irisys 1010	± 0.5 K	0.10 K	20.0	128 pixels	
Thermotracer TH9100P	± 2.0 K	0.06 K	~ 21.7	75 kpixels	

2.3 Contact measurements

The strong directional thermal signature of the vegetation rises from differences in skin temperature and emissivity between the different vegetation components (shaded/sunlit; soil/leaves) (Menenti *et al.*,

2008). For example, the thermal SAIL model (Verhoef *et al.*, 2007) requires the contact temperature of 4 components (soil/leaves, sunlit/shaded) to simulate directional brightness temperatures. The distribution of skin (or contact) temperatures therefore needs to be measured in order to validate the retrieval technique explained in chapter 5.

Calculating the contact temperatures from the radiative measurements requires the knowledge of the emissivity of the components. Techniques such as the temperature emissivity separation (TES) method, (Gillespie *et al.*, 1998), and the “box measurement” (Sobrino and Caselles, 1993), are usually used to determine emissivity. However, for long term measurements of component temperatures, both these methods are limited as to their applicability. TES methods require the use of expensive multi-band radiometers, while the box method relies on the assumption of a homogeneous flat land cover and hence cannot be used to separate between soil and canopy emissivity.

Contact probes provide a useful tool in addition to current techniques, such as radiative measurements with pyrometers, for measuring these component temperatures. They are cheap, easy to use and provide a continuous measurement of the contact temperatures. Another benefit is that they can provide the researcher with continuous in-canopy leaf thermodynamic temperatures, without the need to determine the emissivity.

The measurements were performed using SEMI 833 ET negative temperature coefficient (NTC) probes. These probes are extremely small (6 mm) and combine a high sensitivity (0.07°C at 37°C) with a very small heat capacity (1.42 °C/mW). The maximal heating up of the individual probes has been calculated as 6×10^{-3} °C/s for an illumination of 750 W/m². As this is very little compared to the heating up of a leaf, the thermodynamic properties of the leaves are affected only minimally by the probes. These probes were attached to the leaves using plastic paperclips (Figure 2-5). A Campbell C23 logger was used for storing the measurements of the probes.

2.4 Field sites

Three datasets were created during three field different campaigns: SEN2FLEX2005, EAGLE 2006 and AGRISAR 2006. Work undertaken during these field campaigns will be explained in detail in the following subsections. During each campaign optical and thermal

radiative measurements were taken from a variety of crops, see Figure 2-6.



Figure 2-5: Leaf Skin measurement during the SEN2FLEX2005 campaign.

The measurement was performed with a SEMI 833 ET probe held in place with a paperclip.

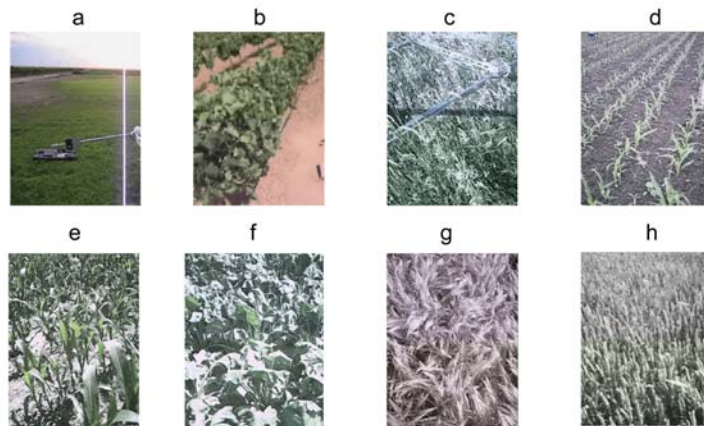


Figure 2-6: Crops investigated with goniometric setup.

(a) shows a grassfield (short), (b) a vineyard, (c) a grassfield (tall), (d) maize (young), (e) maize (mature), (f) sugarbeet, (g) barley and (h) wheat. The measurements in (a) and (b) were taken during SEN2FLEX 2005, those in (c) and (d) during EAGLE 2006, and those in (e) to (h) during AGRISAR 2006.

2.4.1 SEN2FLEX

In 2005 an intensive field campaign was organized in Barrax, Spain, by the European Space Agency (ESA) in the framework of the Earth Observation Envelope Programme (EOEP). The SENTinel-2 and FLUorescence EXperiment (SEN2FLEX) campaign combined different activities for testing and validation of the fluorescence measurements (AIRFLEX) and Sentinel2 spectral and spatial resolutions prototyping. The first objective of the campaign was the preparation of a future Vegetation Fluorescence Mission, based on the AIRFLEX flights. The second objective of the campaign was the preparation for the Sentinel Missions, the Global Monitoring for Environment and Security (GMES) component of future operational missions. In total 29 groups from different countries in Europe participated in the field campaign. More details about the SEN2FLEX measurements can be found in (Sobrino, 2007 ; Su *et al.*, 2008) and in the experimental handbook¹ (University of Valencia 2005).



Figure 2-7: Land cover of the agricultural test site of Barrax, Spain.

In panel A the land cover at Barrax, Spain is shown. Panel B shows the grass and 'las Tiasas' vineyard, where goniometric measurements have been taken. Both images were taken by the INTA institute from the AHS airplane in July 2005

The agricultural test site in Barrax consisted of various large plots, shown in Figure 2-7, with different agricultural crops. The test site was situated at a plateau 700m above sea level within the La Mancha region in the south of Spain, in the western part of the Albacete province, 20km away from the capital town Albacete. The area is characterized by a flat morphology and large, uniform land use units and consists of approximately 65% dry land and 35% irrigated land

¹ www.uv.es/leo/sen2flex/

with different agricultural crops and fruits. The climatic conditions are Mediterranean with precipitation in spring and autumn, but little in summer. With an annual rainfall average of about 400mm, La Mancha is one of the driest regions of Europe. The regional groundwater table is about 20–30m below the land surface. The site is maintained by the Instituto Técnico Agronómico Provincial (ITAP).

During the field campaign, the Water Resources group from the International Institute for Geo-Information Science and Earth Observation (ITC) measured the optical and thermal directional signatures and contact temperatures of short grass (10cm) and vineyard (1.5m). In total 24 runs were performed at during day time with an average sampling time of 1 hour. The measuring protocol during the SEN2FLEX campaign consisted of only a single run. Concurrent to these measurements, fluxes between the surface and the atmosphere were measured, using standard meteorological sensors, eddy-correlation sensors and a large aperture scintillometer (Su *et al.*, 2008).

2.4.2 EAGLE

In 2006 an intensive field campaign in the Netherlands was organised by the ITC with the support of the ESA. The general objective of the field campaign was to improve the understanding of bio-geophysical parameter retrieval from optical, thermal and Radar data, with special emphasis on multi-angular multi spectral observations. In total, 16 different groups from 6 different countries participated in the campaign.

The activities during this EAGLE campaign were performed in three different areas in the Netherlands: two forested areas (Loobos and Speulderbos), and the Cabauw agricultural site. A short description of each of these sites is provided below, more detailed information can be found in (Su *et al.*, 2009) and in the EAGLE data acquisition (ITC, 2006)

1. **Loobos.** The Loobos site is located about two kilometres from the village of Kootwijk. Land cover mainly consists of pine trees. Continuous micrometeorological measurements have been collected there since 1997 at 23 m above the surface by Wageningen University. More detailed information can be found on the ALTERRA website².

² www.loobos.alterra.nl

2. **Cabauw.** The Cabauw site (van Olden and Wiring, 1996; Su *et al.*, 2009) is located about one kilometre from the village of Cabauw. The area is characterised by a flat morphology with dominantly grass and agricultural land cover. The ground water level is kept artificially low (40cm beneath the surface) by a narrow-spaced set of ditches. A 213 meter tall mast was built at the site in 1972 by the Koninklijk Nederlands Meteorologisch Instituut (KNMI) for measuring the atmospheric boundary layer.
3. **Speulderbos.** The Speulderbos site is located about two kilometres from the village of Garderen (Bosveld *et al.*, 1999). The area is slightly undulating, varying between 10 to 20 meters in height, with a land cover consisting of different tree types, such as Douglas fir, Lark, Scotch pine and Beech, planted in 1962. A 46 meter high tower, operated by the National Institute for Public Health and the Environment (RIVM) is situated at the centre of the study area. The trees around the tower (Douglas fir) had a height of 32 meters in 2006. Measurements at this site are performed using standard meteorological instruments, eddy correlation instruments at different levels on the tower and a large aperture scintillometer (Hartogensis, 2006) on the top of the tower.

In addition to the long term measurements collected at the different towers, optical and thermal radiative multi directional measurements were taken over tall grassland and young maize at the Cabauw site. In total 29 runs were performed at day time with an average sampling time of 45 minutes. At the Speulderbos site optical hyperspectral multi-directional (non goniometric) measurements were taken as well.

2.4.3 AGRISAR

In 2006 a long duration field campaign in Görmin, Germany, was organised by the ESA to support geophysical algorithm development and validation of the different Sentinel satellites. The Agricultural Bio-/Geophysical Retrievals from Frequent Repeat SAR and optimal imaging (AGRISAR) field campaign lasted from the 18th of April to the 2nd of August, 2006, with several periods of intensive measuring. In the context of Sentinel-1, the AGRISAR field campaign placed special emphasis on algorithm development for the Synthetic Aperture Radar (SAR) sensor over agricultural vegetation. By also including optical measurements the campaign provided an important role in the sensor prototyping of the Sentinel-2 spectral requirements. Overall, 15 institutes from different countries were involved in AGRISAR. More

details about the SEN2FLEX measurements can be found in (Sobrino, 2007 ; Su *et al.*, 2009), and in the experimental handbook³ (German Aerospace Centre (DLR), Oberpfaffenhofen).

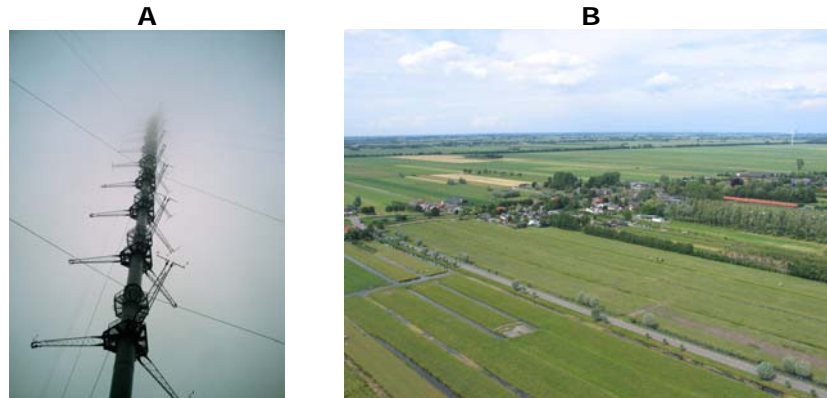


Figure 2-8: KNMI Measurement site at Cabauw, the Netherlands.

In panel A, the 213 meter tall atmospheric boundary layer measurement tower is shown. At each of the booms several instruments are located. In panel B the surrounding area, including the village of Cabauw, is shown.

³ <http://www.docstoc.com/docs/19623545/AgriSAR-2009-Campaign-Overview-Early-Results-and-Analysis-Plan>

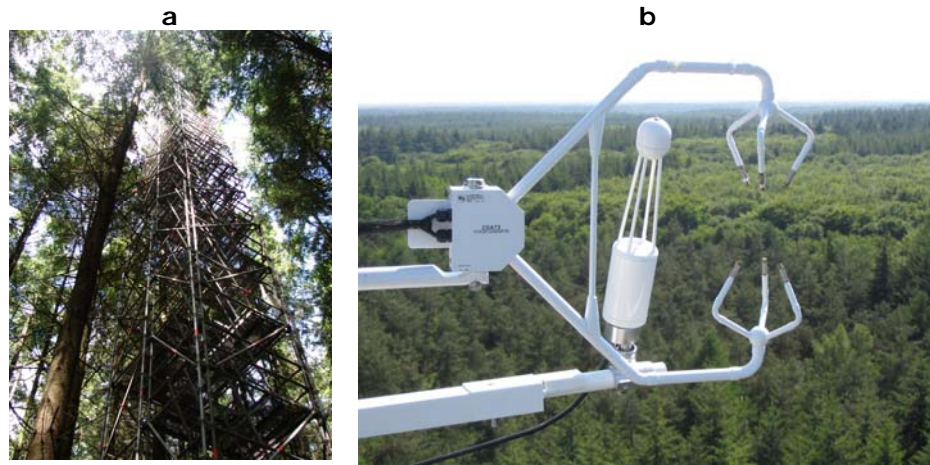


Figure 2-9: Measurement site at Speulderbos, the Netherlands.

In the panel A, the measurement tower is shown; in panel B the instruments (3D-Sonic Anemometer and a gas analyser) used for eddy-covariance measurements are shown at 46m altitude.

The Durable Environmental Multidisciplinary Monitoring Information Network (DEMMIN) test site in Görmin, Germany, consists of four large-area farms covering over 25.000 ha of agricultural land. The main crops grown are winter wheat, winter barley, winter rape, maize and sugar beet. The area is very flat with a topographic range between 0 and 37m.

During the last intensive measurement period (6 to 13 July) the Water Resources group measured the optical and thermal directional signatures of the vegetation over mature maize (0.3m), wheat (1.2m), barley (1.2m) and sugar beet (0.3m). The total number of measurements taken was 15, with only a few runs per crop. Concurrently the fluxes (Pauwels *et al.*, 2008) between the surface and the atmosphere were measured using standard meteorological sensors and a large aperture scintillometer. No contact temperatures were measured during this campaign.

2.5 Results and Discussion

A large number of measurements were taken in the different field campaigns. The results focus on within-species variations and

interspecies differences. In section 3.1 species are compared at different growth stages (tall grass vs. short cut grass and mature maize vs. young maize). In section 3.2 different species are compared to one another.

Each of the figures contains a top down schematic of the goniometric positions of the sensor in order to illustrate the azimuthal positions. The colours in the plot correspond to the colours in the schematic. In this schematic representation the suns position is shown as a star and the dominant orientation of the vegetation by a line.

2.5.1 Reflectance variation in different grass canopies

The grassland phenological stages of interest are: short cut (SEN2FLEX) and tall grasses (EAGLE). The brightness temperatures of these stages are shown in Figure 2-10. The directional variations are low in both short and tall grassland. This is to be expected, as both crops are dense and homogeneous in nature. In tall grassland the nadir-looking brightness temperature is slightly lower compared to other viewing angles. The explanation for this is that at nadir, the viewing angle is parallel to the grass leaves. The effective cross-section of the grass is therefore at its lowest, and the contribution of the soil to the observed radiation at its highest. At the time of acquisition, the sun had a low elevation angle, and consequently most of the solar radiance was absorbed by the overlaying canopy. The low variation in brightness temperature is in agreement with contact temperature measurements taken at the time of acquisition.

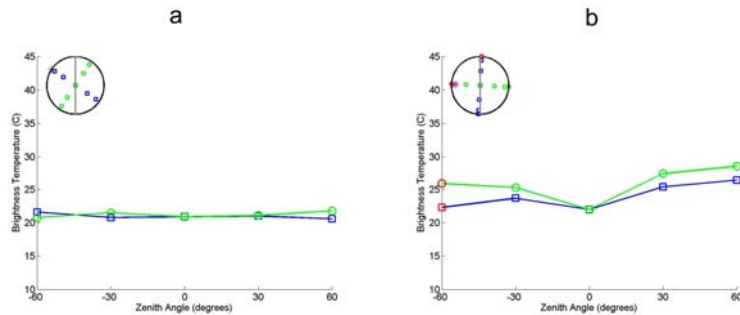


Figure 2-10: Directional Thermal Brightness temperatures of grass.

In panel (a) the directional brightness temperature of low grass (0.1m) is shown (measurements at 20h43 during the SEN2FLEX campaign), as acquired by Everest Radiometer. In panel (b) the directional brightness temperature of high grass (0.8m) is shown (measurements at 17h35 during the EAGLE campaign), as acquired by Everest Radiometer.

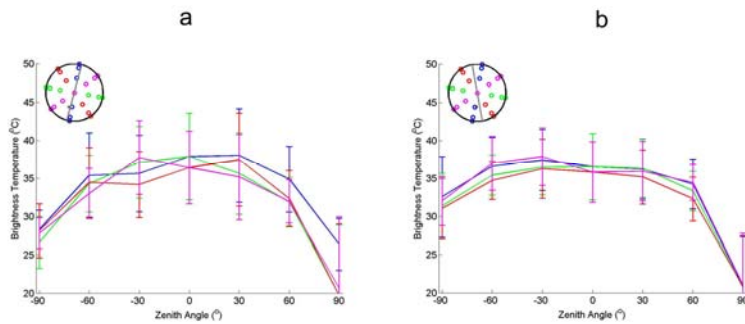


Figure 2-11: The directional brightness temperature of maize. In panel (a) the directional thermal brightness temperature of young maize is shown (measurements at 12h47 during the EAGLE campaign), as acquired by Irisys thermal camera. The error bars denote the standard deviation of the brightness temperatures in the image to the mean brightness temperatures. In panel (b) the directional thermal brightness temperature of mature maize is shown (measurements at 13h01 during the AGRISAR campaign), as acquired by Irisys thermal camera.

2.5.2 Reflectance variation in different maize canopies

Maize phenological stages of interest are defined as: young (EAGLE) and mature (AGRISAR). The brightness temperatures of these stages are shown in Figure 2-11.

The directional variations in the brightness temperature are present in both young and mature maize. The directional behaviour for young maize is only pronounced at very high viewing zenith angles (-90° and $+90^\circ$). At these angles the individual maize plants appear to form a closed canopy, whereas at normal viewing angles the maize canopy appears more open. As the soil temperature at the time of acquisition was higher than the canopy temperature, the brightness temperature was higher when more soil was observed. Variations in measured contact temperature of the different components are in agreement with the above explanation.

2.5.3 Directional variation in different crop types

A comparison between the directional signatures of brightness temperature for different canopies was also performed. Figure 2-12 shows the results for barley, wheat, sugar beet and vineyard. The canopies are presented in order of structural complexity.

Barley and wheat display the same directional thermal behaviour as the tall grassland, with very moderate directional behaviour. Similar to tall grass, barley and wheat consist of long stems and slim leaves. The only difference between grassland and these two crops is the mean temperature. This is caused by the higher canopy temperature at the time of acquisition during the AGRISAR campaign and the EAGLE campaign.

Sugar beet displays more directional thermal behaviour than barley and wheat, but less than maize. This is caused by the severe drought that occurred during the AGRISAR campaign, causing wide leaves to rest horizontally on the ground. The horizontal orientation of the leaves and the coverage of the soil reduced the directional thermal signature.

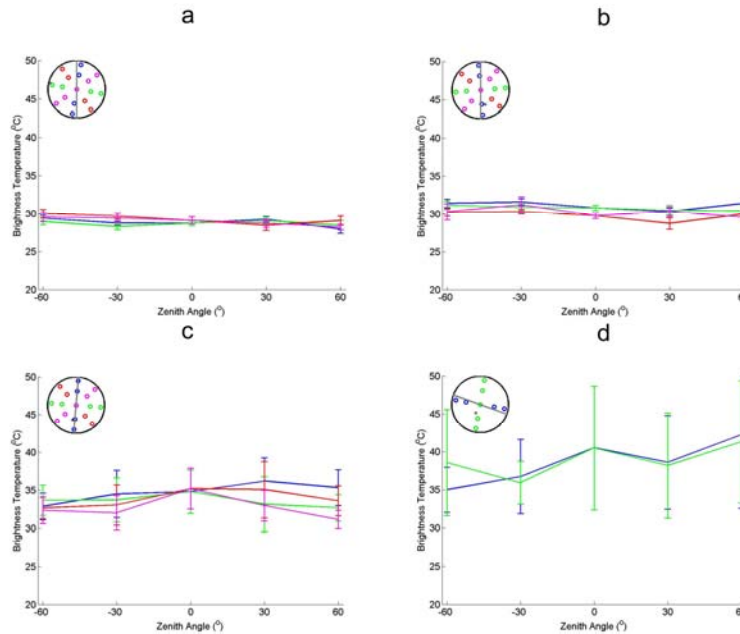


Figure 2-12: Directional brightness temperatures over different crops. Panel (a) shows barley at 18h08 (AGRISAR). Panel (b) shows wheat at 11h30 (AGRISAR). Panel (c) shows sugar beet at 12h43 (AGRISAR). Panel (d) shows the vineyard at 16h30 (SEN2FLEX). The error bars denote the standard deviation of the brightness temperatures in the image to the mean brightness temperatures. All observations shown were acquired by the Irisys 1011 thermal camera

The vineyard displays large but inconsistent directional variations in the thermal emission. The reason is that the spatial scale of the variations in the crop is larger than the field of view of the sensor. As a result the ratio of soil/canopy in the image is not constant. This is mainly caused by variations in soil-canopy ratio and will be discussed further in the next paragraph.

In addition to the measurements performed with a single band radiometer/ thermal imager, measurements using the CIMEL multi-band radiometer were performed over the vineyard. These results are shown in shown in Figure 2-13-A.

The variations in the directional signature of vineyard observed by the single band thermal imager (Figure 2-12d) do not correspond to

the variations found by the CIMEL multiband radiometer. This is because the orientation of the CIMEL camera was modified for each angle. Consequently the ratios of vegetation to soil are different for the single band instruments and the CIMEL instrument

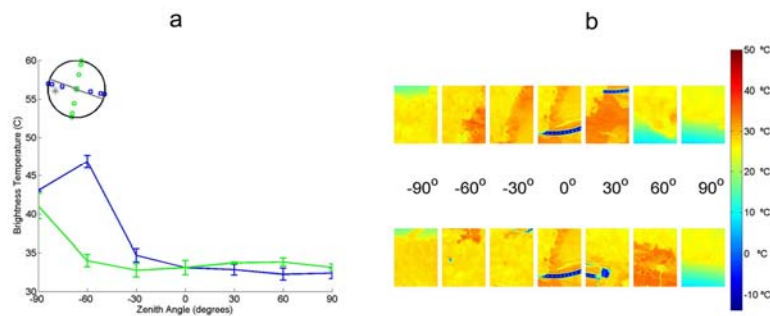


Figure 2-13: Variation in thermal brightness temperatures. In panel (a) the directional brightness temperatures acquired at 16h30 by the CIMEL 312-1 (band 1: 8-14 μ m) is shown. The error bars denote the difference of band 1 to the other bands. In panel (b) the brightness temperatures at different angles by is shown; as acquired by Thermotracer at 18 h 89.

2.6 Conclusions and outlook

This chapter presents a technique to obtain directional measurements fast using a goniometer. Taking measurements fast is made possible by automating the goniometric system and the attached sensors. The goniometer is able to complete a run within four minutes. This acquisition time is within the timeframe normally posed for kinematic temperature changes in canopies. Therefore this goniometer is suited for making thermal directional measurements.

The results of the thermal directional measurements taken over different crops have been shown. These crops are: short and tall grassland, young and mature maize, barley, wheat, sugar beet and vineyard. The directional radiative thermal signatures corresponded very well with expectations. The results can be used to retrieve the component brightness temperatures of soil and leaves.

In addition a method was also presented for measuring the skin temperature of the different land surface components with contact probes. The advantage of using these probes is that they are very cheap, can measure at high temporal resolutions, and do not require knowledge about the emissivity.

3 Identification of Land surface components

Based on

Timmermans, J., van der Tol, C., Verhoef, W., and Su, Z., 2008, 'Contact and directional radiative temperature measurements of sunlit and shaded land surface components during the SEN2FLEX 2005 campaign', *International journal of remote sensing*, 29 (2008)17-18, pp. 5183-5192

Timmermans, J., van der Tol, C., Weligepolage, K., Vekerdy, Z., Jia, L., and Su, Z., 2007, 'BRDFs acquired by directional radiative measurements during EALE and AGRISAR', In: *Proceedings of the AGRISAR and EAGLE campaigns, final workshop*, 15-16 October, 2007. ESA/ESTEC, Noordwijk, The Netherlands. ESA Proceedings WPP-279, 6 p.

Abstract

This chapter describes the identification of different land surface components based on differences in skin temperature. This identification is based on contact temperature measurements of the different components combined with a simple inversion of multi-angular radiometric measurements.

The land surface consists of different components, such as sunlit and shaded soil, and sunlit and shaded leaves. The temperature of these components can be estimated by inversion of radiative transfer models. Such estimation is troublesome because of the ill-posedness of the inversion problem, restricting the number of skin temperatures that can be retrieved successfully. Consequently the most important land surface components need to be identified.

Firstly, the most complex land surface type is identified using directional radiative signatures. In order to provide an objective indicator two parameters are defined (optical and thermal). Secondly, the most important land surface component is identified based on contact measurements on skin temperature. A simple method was used to retrieve the temperature of these components.

In total seven land cover types were investigated: vineyard, sugar beet, wheat, barley, mature corn, young corn and forest. The vineyard was the most complex vegetation type in this study, with sunlit and shaded soil, and sunlit and shaded leaves forming the dominant components.

3.1 Introduction

A problem with remote sensing is how to interpret observed radiation reflected or emitted by the land surface. This interpretation is difficult, because of the scale difference between the observations by the (satellite) sensor and the land surface components of interest (Giorgi and Avissar, 1997), as illustrated in Figure 3-1. Here the sensor samples have a lower resolution than the individual land surface components, making interpretation of the brightness temperatures from the different viewing angles difficult.

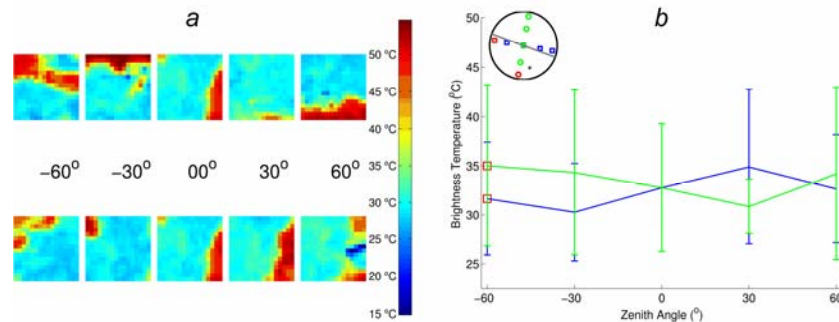


Figure 3-1: Thermal brightness temperatures of the vineyard. Panel (a) shows the thermal brightness temperatures for different viewing angles acquired at 12h13 on 13-07-2005. Panel (b) shows the average temperature as a function of the zenith viewing angles. The error bars denote the standard deviation.

The observed radiation by a (remote sensing) sensor is an aggregate of the emitted/reflected radiation by the different components of the land surface (Su *et al.*, 1999; Kustas *et al.*, 2003). This aggregation is one of the biggest sources of uncertainty within remote sensing algorithms. For example, the observed thermal radiation at sensor level is the sum of the thermal radiation emitted by each of the canopy components, such as soil and canopy, within the viewing field. The land surface temperature and evapotranspiration estimated from thermal radiation therefore might not be accurate (Anderson *et al.*, 2004).

Detailed radiative transfer models like SAIL (Verhoef, 1984) and DART (Gastellu-Etchegorry, 2008) simulate this aggregation using surface variables as input parameters (Jacquemoud *et al.*, 2000). Simulation of this reflected optical radiation by radiative transfer

models requires variables such as chlorophyll and water content, Leaf Angle Distribution (LAD) as well as the sun and observation angles. The simulation of emitted thermal radiation by the land surface requires extra information such as emissivity and skin temperature of the different components.

Inversion of these radiative transfer models yields the surface variables from remote sensing observations (Combal *et al.*, 2002; D'Urso *et al.*, 2004; Meroni *et al.*, 2004). Inversion of a radiative transfer model is always troubled by ill-posedness of the inversion problem. In other words, there are mostly not enough linearly independent measured data to estimate the total number of desired variables. Consequently only a small subset of the total number of desired variables can usually be retrieved.

Multi-directional remote sensing provides unique extra data (Jia *et al.*, 2003a), thus enhancing the retrieval potential compared to traditional single view nadir observations (Jia, 2004). Not only higher accuracy can be achieved using multiple viewing observations, but also sub-pixel characteristics can be estimated (Widlowski, 2001). Although the potential of directional observations is very large, it can not solve the inversion problem completely.

In this chapter the identification of the most important land surface components is investigated. The directional radiative observations in the optical and thermal domain are used, together with the skin-temperatures of the different components. All data were collected during the three field campaigns described in Chapter 2.

3.2 Methodology

An inversion algorithm was applied to estimate sunlit and shaded vegetation and soil temperatures separately. The algorithm was applied and validated for a complex canopy.

Not all land cover types are equally heterogeneous: in dense grass the difference between sunlit and shaded soil temperatures will be less than in a clumped vegetation type such as a forest or a row crop. For the latter, retrieval of component temperatures is relevant. The most complex canopy was selected based on an analysis of the directional signatures using indicators that describe the directionality of the vegetation type.

A simple retrieval method was performed to identify specific land surface components. The method was based on (Leinonen and Jones,

2004), and combined optical and thermal observations. Measured skin temperatures of sunlit and shaded soil and vegetation were used for the final validation.

3.2.1 Directional radiative signatures

Optical directional radiative signatures are usually described by the bidirectional reflectance distribution function (BRDF), as shown in Figure 3-2 for hyperspectral measurements over trees. In order to visually enhance the directionality of the measurements a Normalized Reflection Ratio (NRR) is defined. This NRR is calculated by equation (3-1).

$$NRR = \frac{R_{\theta} - R_{nadir}}{R_{\theta} + R_{nadir}} \quad (3-1)$$

Here R_{nadir} and R_{θ} are the reflectance at, respectively, nadir observation angle and arbitrary observation angle. Note that the hyperspectral measurements were first pre-processed to reduce the noise and sensor errors.

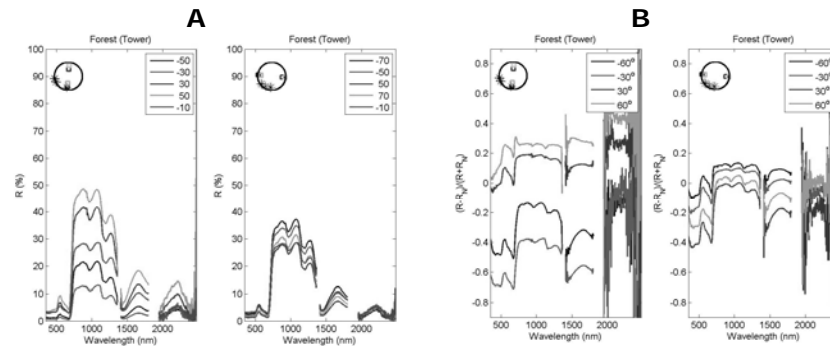


Figure 3-2: VNIR radiative directional measurement (one transect only) of forest. In figure A the reflections per angle are given. In figure B the corresponding normalized reflection ratio is shown.

In order to facilitate the distinction between the most simple and the most complex canopies an objective parameter is defined. This Optical Structural Parameter (OSP) is calculated as the maximum standard deviation of the NRR for three parts of the spectrum: VIS

Identification of Land surface components

(400 nm - 800 nm), NIR (800 nm - 1000 nm), MWIR (1500 nm - 1700 nm).

The methodology for calculating the OSP is unsuitable for the thermal domain, as reflection in the thermal domain contributes only a little to the total radiative signal. The larger part is emission. This emission is highly variable over time, and consequently a single BRDF valid for a complete day can not be constructed.

Instead a Separation Parameter (TSP) and Thermal Directional Parameter (TDP) are defined. First we calculate the average temperature ($\bar{T} = \text{mean}(T_{ij})$) of the image pixels and standard deviation of the image pixels ($\hat{T} = \text{std}(T_{ij})$).

The Thermal Separation Parameter (TSP) is set to the ratio between these two variables, equation (3-2).

$$TSP = \max\left(\frac{\hat{T}}{\bar{T}}\right) \quad (3-2)$$

The ratio of \bar{T} and \hat{T} provides a normalized indication of the variability within an image. Using the maximum of the different observations a single value is found determining the variation in all observations.

However the TSP does not take into consideration variation per observation angle, and the potential of retrieving component temperatures through a combination of angles. Therefore the TDP is defined so that it focuses on angular variation, equation 3-3 **Error! Reference source not found.**)

$$TDP = \max\left(\frac{\hat{\bar{T}}}{\bar{\bar{T}}}\right) \quad (3-3)$$

Similar to the TSP the TDP is defined as the ratio of the variation and the average temperature, with the average 'Lambertian' brightness temperature ($\bar{\bar{T}} = \text{mean}(\bar{T}(\theta_o))$) and the angular variation in the average temperature ($\hat{\bar{T}} = \text{std}(\bar{T}(\theta_o))$).

3.2.2 Land surface components identification

It is worthwhile to take the effort to separate soil and vegetation, because the processes in each of these components differ (Jia *et al.*, 2003a). In soil the transfer of water to the atmosphere is a completely physical process, whereas in vegetation it is a biophysical process.

Further separations should be made based on the individual temperature of the different components. Processes like evaporation, transpiration and photosynthesis are non-linearly dependent on this variable (Yin and van Laar, 2005). Hence a distinction between sunlit/shaded canopy and sunlit/shaded soil is justified (Verhoef *et al.*, 2007). The leaf temperature varies within the canopy due to differences in absorbed radiation. Not only does the amount of incident radiation on the leaves vary within the canopy, differences in leaf absorption also exist, for example old leaves may have a lower absorption than young leaves, as they have a higher leaf albedo. Therefore the measurements also been applied to identify old and young leaves, and high and low leaves, as shown in Table 3-1.

Table 3-1: Land Surface Components measured in the Vineyard

Nr	Specification	H (m)	Label
1	Sunlit young leaves	1	L_{syh}
2	Sunlit old leaves	1	L_{s0h}
3	Shaded young leaves	1	L_{dyh}
4	Shaded old leaves	1	L_{d0h}
5	Sunlit young leaves	0.5	L_{sym}
6	Sunlit old leaves	0.5	L_{s0m}
7	Shaded young leaves	0.5	L_{dym}
8	Shaded old leaves	0.5	L_{d0m}
9	Sunlit soil	0	S_{sl}
10	Shaded soil	0	S_{sdl}

3.2.3 Component brightness temperature extraction

A combination of thermal and optical imagery can be used to identify the skin temperatures of the different land surface components (Leinonen and Jones, 2004). Although the Irisys thermal camera has

Identification of Land surface components

a too low resolution to identify individual leaves, a similar method, based on object classification, was used to retrieve canopy and soil brightness temperatures. The following scheme was used to separate the pixels from each other.

1. Erroneous pixels were identified by investigation of the digital and thermal images. These pixels were removed from the image.
2. The remaining pixels were each classified as belonging to a component. Color filtering of the digital image was used to discriminate the classes (Figure 3-3), in order to create a land component mask.
3. The mask was adjusted to account for the difference in viewing angle between the digital camera and the thermal camera.
4. A histogram was created for both the masked pixels and the non-masked pixels. The mask was adjusted to reduce the outliers in the histogram.
5. The brightness temperatures of soil and canopy were extracted.

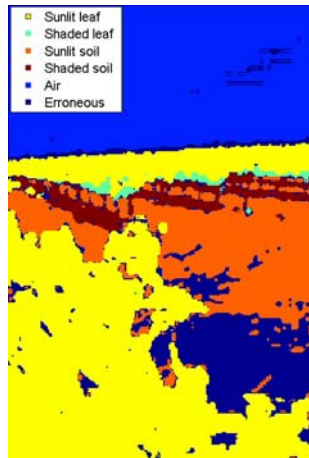


Figure 3-3: Extracted surface components in the Las Tiasas Vineyard.

The extraction of the various surface components was performed based on color filtering using a digital camera.

3.3 Results

3.3.1 Directional radiative signatures

The measurements were collected successfully with the hyperspectral spectrometers over all the land surface types listed in Chapter 2, except for barley. All measurements were converted to BRDFs, NRRs and finally the OSPs, which are given in Table 3-2.

Inspection of the OSPs learns that the vineyard shows the largest directional behaviour, followed by sugar beet, wheat, tall grass and mature corn, young corn, and forest.

The vineyard, tall grass and wheat display the largest directional behaviour in the VIS region, young and mature corn in the NIR region, and wheat and sugar beet in the MWIR. The overall directionality in the VNIR part of the forest seems low. This is caused by the smoothing effect of the large field of view under low viewing angles.

Table 3-2: Optical Structural Parameter for different land cover types.

Vegetation	VIS	NIR	MWIR	Full spectrum
Vineyard	26.85	11.99	16.49	18.40
Sugar beet	24.12	11.87	16.73	17.57
Wheat	25.59	7.54	17.28	16.80
Grass (tall)	20.98	09.76	16.56	15.77
Mature Corn	15.39	18.38	08.00	13.92
Young Corn	13.63	12.29	11.58	12.50
Forest	9.18	10.79	14.53	11.50

The measurements with the thermal imager were carried out successfully over all land cover types, with the exception of forest. The TDP and the TSP are given for each land cover type in Table 3-3.

Table 3-3: Thermal Directional and Separation Parameter (TDP and TSP).

The vegetation is sorted depending on the separation parameter.

Vegetation	TDP Irisys	TSP Irisys
Vineyard	98.6	13.12
Mature Corn	67.9	12.47
Young Corn	69.6	09.30
Sugar beet	46.69	07.15
Grass (tall)	48.7	04.17
Wheat	56.4	02.29
Barley	20.7	01.59

Inspection of the TDP of the different land surface types shows that the vineyard has the largest radiative directionality. The other land surface types, in order of decreasing TDP, are mature corn, young corn, sugar beet, tall grass, wheat and barley. Comparison of the TDP and the TSP shows similar results.

Although the TDPs of the various measurements show slight variations with respect to the OSP, both confirm that the Las Tiesas Vineyard displays the highest directionality. This land surface type is therefore used for the identification of the different canopy components.

3.3.2 Land surface component skin temperatures

The skin temperatures of the different components of the vineyard were measured from 13h17 on 13 July 2005 until 19h32 on 15 July 2005. In Figure 3-4 the skin temperatures of the different canopy components are shown.

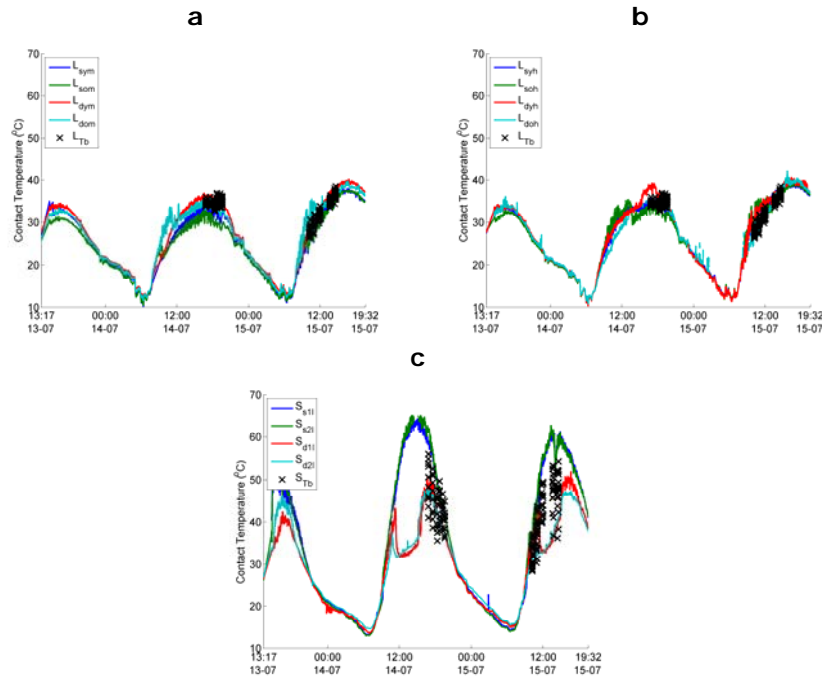


Figure 3-4: Skin temperatures from contact probes and the Irisys thermal imager.

The leaf (L) temperatures are shown in (a) and (b), respectively, for leaves at the top (h) and in the middle (m) of the canopy. The soil (S) temperatures are shown in (c). Other subscripts denote sunlit soil/leaves (s), shaded soil/leaves (d), young leaves (y), and old leaves (o). The colored lines represent the skin temperature values that were measured with the contact probes. The black crosses represent the brightness temperature values that were acquired with the thermal camera.

The leaf temperatures show a considerable variation between the different classes, with unexpected results. In particular, shaded old leaves have higher temperatures than sunlit (old and young) leaves. This occurs because shaded leaves can still be sunlit for specific sun orientations. The probes are attached in such a manner that maximizes the possibility of a leaf falling within the classes defined by Table 3-1. However the sun rotation during the day influences if and when a leaf is shaded or not. This is most clearly observed on July 14 in the shaded young leaf high in the canopy, which has a large increase (>4K) in skin temperature after 13h00. Likewise the probe that measures the shaded soil component becomes sunlit after

16h00, as is concluded from the large increase (>12K) in skin temperature. The importance of the illumination therefore justifies the division between sunlit and shaded components. The temperature difference between components high and low in the canopy and between young and old leaves is much smaller than the difference between sunlit and shaded components.

It is clear from the skin temperature measurements that the most dominant components are the sunlit and shaded soil, followed by the sunlit and shaded leaves. In the next section these temperatures will be retrieved from the directional brightness temperatures of the Irisys Thermal camera.

3.3.3 Extraction of component temperatures

The directional thermal brightness temperatures were measured from 11h59 on 13 July 2005 until 14h34 on 16 July 2005 quasi continuously using the Irisys thermal camera (Figure 3-1). Digital images were acquired with a Canon Powershot camera at 14h34 on 16 July 2005.

Histograms of the thermal images (Figure 3-5) show two distinct peaks in the brightness temperatures. The temperature difference between the central parts of the peaks is larger than the difference of 4K found for canopies with only leaves (Shimoda and Oikawa, 2006). It is clear that this difference originates from large patches with high values of brightness temperatures, caused by the sunlit/shaded soil.

Because only two peaks were observed in the thermal brightness temperature images, only soil and leaf temperature were retrieved. Although in the visible image more components could be identified (Figure 3-3), clearly the resolution of the thermal images did not allow for further separation of their component temperatures. The brightness temperatures of the soil and canopy components are shown in Figure 3-4.

The extraction of the components resulted in a mean standard deviation for canopy brightness temperatures of 1.30K and for soil brightness temperatures of 3.07 K. The brightness temperatures of these components are compared to the contact temperatures of the 10 components in Figure 3-4. The soil contact temperature has a similar amplitude and time variability to the soil brightness temperature (Figure 3-4 c). The spread in the soil brightness temperature is caused by the fact that sunlit soil and shaded soil are not separated. The canopy contact temperature has the same

amplitude and time variability as the canopy brightness temperature (Figure 3-4 A and B).

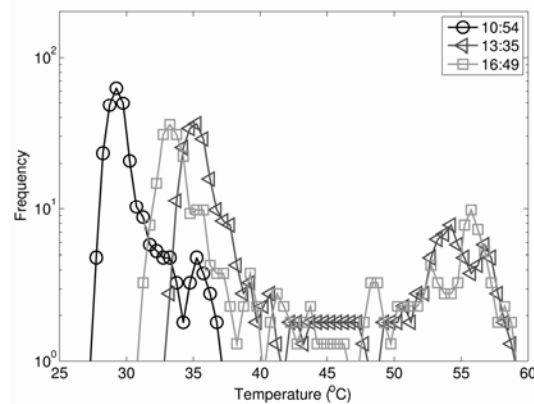


Figure 3-5: Temperature variation in the thermal images. In the histogram of the nadir thermal images, two distinct peaks are observed at each time step. The first peak is the canopy temperature; the second peak is the soil temperature. At 10h54 the soil peak has just formed.

In Figure 3-6 the brightness temperatures of both the leaves and the soil are plotted against the corresponding (mean) contact measurements. The slope and offset parameters of the scatter plot were calculated for all angles (Table 3-4). These parameters are a measure of the agreement between contact and brightness temperatures. The slopes have similar values for most angles. The extraction scheme successfully resolved the angular difference of the fraction soil–canopy pixels, except for viewing angles 4 ($\theta_o = 30^\circ, \varphi_o = 0^\circ$), and 9 ($\theta_o = 30^\circ, \varphi_o = 90^\circ$). The slopes and the offset for the soil scatter plot for viewing angles 4 and 9 are larger than expected. The reason is the larger fraction of shaded soil compared with the other images.

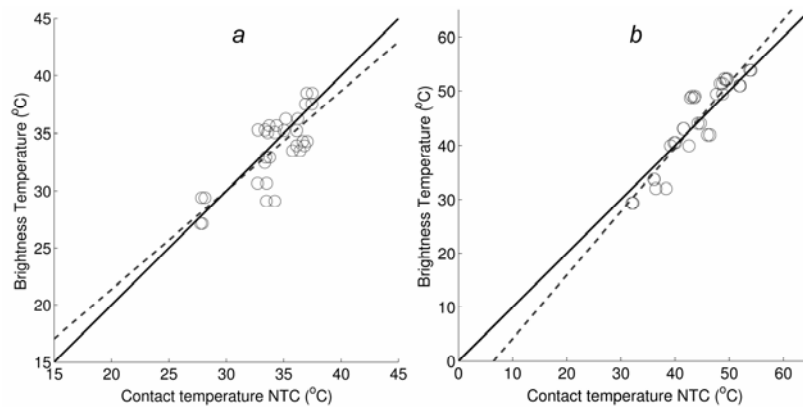


Figure 3-6: Scatter plots of the nadir brightness temperatures and contact temperatures for canopy and soil (open circles). The best fit to the measured points is shown by a dotted line. The best fit for soil was achieved with $0.86x + 4.08$ and the best fit for leaves was achieved with $1.18x - 7.66$.

Table 3-4: Statistics of component temperature extraction. The component brightness temperatures were plotted against the component contact temperatures.

Nr	Angles		Leaves		Soil	
	Zenith [°]	Azimuth [°]	Slope [K/K]	Offset [K]	Slope [K/K]	Offset [K]
1	Nadir	-	0.86	4.08	1.18	-7.66
2	-60	0	0.97	0.35	1.11	-6.13
3	-30	0	0.94	1.2	1.11	-5.59
4	30	0	0.76	7.67	0.6	14.79
5	60	0	0.69	10.04	0.99	2.53
6	-60	90	0.97	0.35	1.12	-4.52
7	-30	90	0.94	1.2	0.58	13.6
8	30	90	0.76	7.67	0.63	12.58
9	60	90	0.69	10.04	0.74	12.13

3.4 Discussion

In theory, the emissivity of the components can be retrieved from the slope of the scatter plot between the skin temperature and the brightness temperature. The brightness temperature of the component should be less than or equal to the skin temperature as the emissivity is ≤ 1 . In practice, the scatter of the contact temperatures and brightness temperatures of soil and canopy is too large to estimate the emissivity with sufficient certainty. The high

value of the scatter originates from the large spread in brightness temperatures and is most dominant in the soil scatter plot.

The slope in the soil scatter plot between the contact temperature and the brightness temperature is greater than unity. On average, soil has an emissivity much less than 1. The difference between the slope and expected values of the emissivity originates from the averaging of the soil (contact/brightness) temperature. The value of the soil temperature is calculated as a weighted average of the sunlit and shaded soil temperatures. For the contact measurements the sunlit soil and shaded soil are given equal weights. For the brightness temperature the weights represent the fraction of sunlit or shaded pixels in a single image. This fraction was not calculated because no separation between sunlit and shaded soil was made in the extraction scheme. The retrieval of the soil emissivity from the images could not be performed using this method and requires more detailed measurements and more elaborate statistical methods.

3.5 Conclusion

In this chapter identification of the most important land surface components was attempted based on directional optical (hyperspectral) and thermal radiative measurements, as well as contact temperatures of the different land surface components. The directional radiative observations in the optical and thermal domain were used to find the most complex land surface type. Two indices (optical and thermal) were defined to provide an objective indicator for the most complex vegetation. It was found that the vineyard land surface type was the most complex vegetation in the database of directional measurements.

Concurrently to these directional radiative measurements the skin temperature of twelve components was measured. The twelve components were sunlit, shaded, high, low, young and old leaves, as well as sunlit and shaded soil. It was observed that for both leaves and soil the solar illumination provided the largest temperature differences. Therefore these will be used later on in this dissertation.

Finally a simple algorithm was tried and tested for the extraction of the component temperature. The extraction scheme successfully identified the canopy and soil brightness temperatures from the thermal images. No further separation of sunlit and shaded canopy was possible because the standard deviation of the average brightness temperature values of the canopy was very low. Although the standard deviation of the soil brightness temperatures was high,

Identification of Land surface components

no further separation on the basis of object classification was possible because the resolution of the thermal imager was too low. The fraction of sunlit/shaded pixels could therefore not be determined. A more detailed retrieval method needs to be implemented for the extraction of the different component temperatures.

It is also noted that the contact probes provided a good addition to radiometric techniques used to measure thermodynamic temperature values. The goniometric setup performed very well for the extraction of the brightness temperatures of the canopy and to a lesser extent for those of soil. The contact probes performed very well for the extraction of contact temperatures.

4 The SCOPE model

Based on:

Van der Tol, C., Verhoef, W., Timmermans, J., Verhoef, A., Su, Z., 2009. An integrated model of soil-canopy spectral radiances, photosynthesis, fluorescence, temperature and energy balance. *Biogeosciences* 6, 3109-3129.

Abstract

In this chapter a new Surface Vegetation Atmosphere Transfer model is presented. This Soil Canopy Observation, Photochemistry and Energy fluxes (SCOPE) model is able to estimate the radiative transfer and the biochemical processes simultaneously and in detail.

It integrates several models to accomplish this: the unified SAIL model for detailed radiative transfer, a detailed biochemical model for photosynthesis, and a resistance model for surface-atmosphere interaction. The integration of all these models is performed with a leaf/soil energy balance, allowing for feedback between leaf temperatures, leaf chlorophyll fluorescence and radiative fluxes. On the basis of the identification of the skin surface components, in chapter 3, a distinction is made between sunlit and shaded soil, and sunlit and shaded leaves at different vertical positions within the canopy. This differentiation is also needed for energy balance purposes, as shaded components receive only diffuse light while sunlit components also receive energy from the sunrays.

Model simulations were evaluated against observations reported in the literature and against data collected during field campaigns. These evaluations showed that SCOPE is able to reproduce realistic radiance spectra, directional radiance and energy balance fluxes.

4.1 Introduction

Knowledge of biophysical processes at land surface level is relevant for a wide range of applications including weather and climate prediction, agriculture, and ecological and hydrological studies. Of particular importance are processes that govern the exchange of energy, carbon dioxide and water vapour between land and atmosphere.

In the past several efforts have been made to quantify the biophysical processes. These efforts have resulted into algorithms using remote sensing data (Bastiaanssen *et al.*, 1998; Glenn *et al.*, 2007; Gowda *et al.*, 2007; Kalma *et al.*, 2008), and detailed SVAT models (Sellers *et al.*, 1997; Verhoef and Allen, 2000; Tuzet *et al.*, 2003) using data from ground stations, like the FLUXNET (Baldocchi *et al.*, 2001; Baldocchi, 2003) does. Furthermore, remote sensing data have also been used as input for SVAT models to estimate surface energy balance (Su, 2002; Anderson *et al.*, 2008).

However the full potential of remote sensing data has still not been exploited. Remote sensing data usually have a spatial resolution several times lower than required by SVAT models (Hall *et al.*, 1992). Additionally the relation between radiative transfer parameters and SVAT parameters is often indirect (Norman and Becker, 1995).

In order to make effective use of available remote sensing data, integrated models are needed for the interpretation of observed radiance spectra with respect to physical processes on the ground. The CUPID model (Norman, 1979; Kustas *et al.*, 2007) was the first model that combined both radiative transfer modelling and a characterisation of the heat, water (vapour) and CO₂ exchange in canopies. CUPID is able to estimate the directional brightness temperature of canopies where leaves and soil have different temperatures. The model calculates directional radiance and energy fluxes in forward mode. As this model was not built for inversion observed spectra as it works with only three broadband spectral regions.

The objective of this chapter is to present a model that incorporates the complete spectrum for high accuracy estimation of water, carbon dioxide and energy fluxes at the earth's surface. Such a model will need to have the capability of simulating and using both optical and thermal directional radiation (0.4 to 50 μm) with high spectral resolution.

In this framework the Soil Canopy Observation of Photochemistry and Energy fluxes (SCOPE) model is presented. SCOPE was originally designed to simulate optical and thermal directional signatures of the biophysical processes, including photosynthesis and fluorescence. It accomplished this by integrating a unified version of the 1D SAIL radiative transfer model (Verhoef, 1984; Verhoef *et al.*, 2007) with an energy balance model and a leaf photosynthesis model. It calculates the spectral radiation regime and the energy balance of a vegetated surface at single leaf as well as at canopy level, and the spectrum of the outgoing radiation in the viewing direction at a high spectral resolution over a range from 0.4 to 50 μm , thus including the visible, near and shortwave infrared, as well as the thermal domain.

4.2 Model description

The SCOPE model is based on existing theory about radiative transfer, micrometeorology and plant physiology. The strength of the model is the way in which interactions between the different model components are modelled. Four features of the model make it particularly relevant for future applications:

1. The use of the model PROSPECT (Jacquemoud and Baret, 1990; Jacquemoud *et al.*, 2009) for optical properties of leaves in combination with a photosynthesis model;
2. The calculation of heterogeneous canopy and soil temperatures consistent with the energy balance at component level;
3. The calculation of chlorophyll fluorescence as a function of irradiance, canopy temperature and other environmental conditions (in previous models, chlorophyll fluorescence was only a function of irradiance);
4. The incorporation of the SAIL directional radiative transfer model into the SVAT model enables detailed estimation of radiative transfer within the canopy and correct estimation of the outgoing Top Of Canopy (TOC) radiance

The model consists of a structured cascade of distinct modules. These modules can be used separately, or as an integrated model. Depending on the application, certain modules may be left out or replaced by others.

Figure 4-1 shows schematically how the main modules interact. The model distinguishes between modules for radiative transfer (of incident light, internally generated thermal radiation, and chlorophyll fluorescence), and the energy balance. The modules are executed in the order from top to bottom in the figure:

1. RTMo, a semi-analytical radiative transfer module for incident solar and sky radiation, based on SAIL(Verhoef, 1984), calculates the TOC outgoing radiation spectrum (0.4 to 50 μm), as well as the net radiation and absorbed Photosynthetically Active Radiation (PAR) per surface element.
2. RTMt, a numerical radiative transfer module for thermal radiation generated internally by soil and vegetation (Verhoef *et al.*, 2007), calculates the TOC outgoing thermal radiation and net radiation per surface element for heterogeneous leaf and soil temperatures.
3. A new energy balance module estimates the latent, sensible and soil heat flux per surface element, as well as photosynthesis, chlorophyll fluorescence and skin temperature at leaf level.
4. RTMf, a radiative transfer module for chlorophyll fluorescence based on the FluorSAIL model (Miller *et al.*, 2005), calculates the TOC radiance spectrum of fluorescence from leaf level chlorophyll fluorescence (calculated in step 3), and the geometry of the canopy.

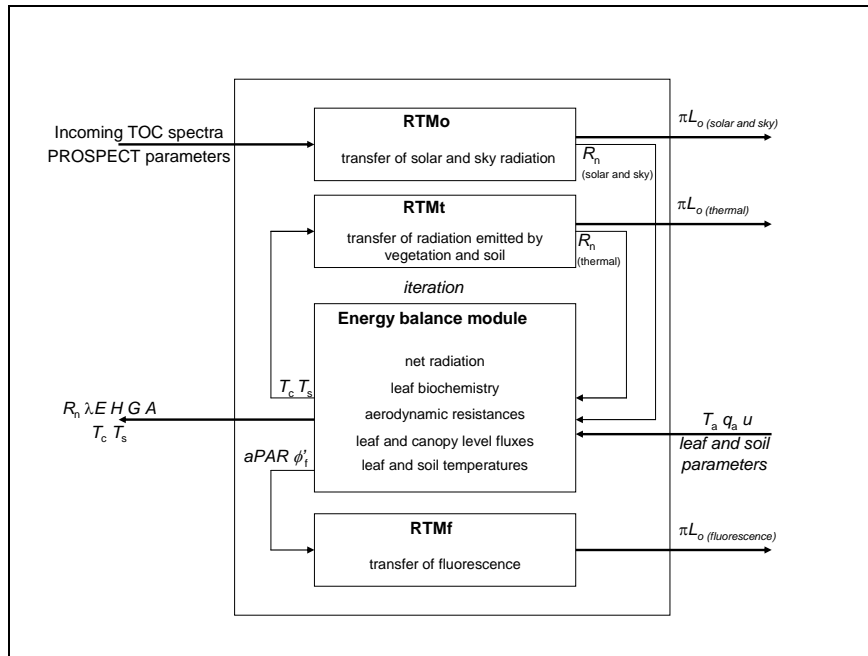


Figure 4-1: Schematic overview of the SCOPE model structure.

In the following sections, the different modules of the model are described in more detail. The modules are presented in an order,

which facilitates the conceptual understanding of the model and (with very few exceptions) is also the order in which they are executed by the model (Figure 4-1).

4.2.1 Atmospheric optical inputs

The SCOPE model requires TOC incident radiation as input, at a spectral resolution high enough to take the atmospheric absorption bands properly into account. For the top of the canopy the incident fluxes from the sun and the sky are to be obtained from the atmospheric radiative transfer model MODTRAN (Berk *et al.*, 1998).

Ideally, the calculation of TOC incident fluxes is performed using the actual values of solar zenith and azimuth angle and atmospheric conditions. However this is computationally very demanding. Instead an alternative approach is used. A library of several spectra of incoming radiation was created by MODTRAN. SCOPE then extracts a typical spectrum for specific conditions.

The examples in this study use only one example spectrum. Figure 4-2 shows the spectra of E_{sun} and E_{sky} (in $\text{W m}^{-2} \mu\text{m}^{-1}$) for a surface albedo of zero. From these results it can be concluded that at $2.5 \mu\text{m}$ the diffuse sky irradiance starts to increase due to thermal emission, and at wavelengths longer than $8 \mu\text{m}$ the diffuse sky irradiance is even the dominant source of incident radiation. In spectral regions of low atmospheric absorption (high transmittance, see for instance the $8\text{-}14 \mu\text{m}$ thermal window) the thermal sky radiance is less than in absorption bands. This is caused by the correspondingly lower atmospheric emissivity and the fact that higher and thus colder layers of the atmosphere contribute to the radiance at surface level.

4.2.2 Direct and diffuse radiation fluxes

In the first radiative transfer module of SCOPE, RTMo, only the radiative transfer of the optical spectrum is calculated; the effects of thermal emission by surface elements are ignored. Therefore the analytical solutions for the diffuse and direct fluxes, as obtained by the SAIL model, are used to calculate the vertical profiles of these fluxes inside the canopy layer. In addition, net radiation and absorbed PAR are calculated for soil and leaf elements.

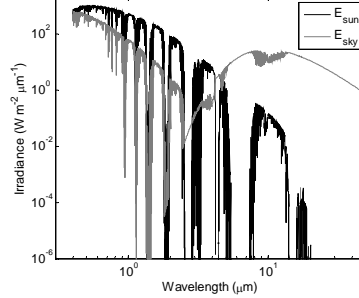


Figure 4-2: Downward direct and diffuse irradiances by MODTRAN simulations.

These radiances (respectively E_{sun} and E_{sky}) are calculated for zero albedo with a solar zenith angle of 30 degrees.

For the diffuse upward (E^+) and downward (E^-) fluxes ($W m^{-2} \mu m^{-1}$), use is made of numerically stable analytical solutions, as provided in the more recent 4SAIL model (Verhoef *et al.*, 2007). The direct solar flux is described by equation (4-1):

$$E_s(x) = E_s(0)P_s(x) \quad (4-1)$$

where $E_s(0)$ is the direct solar flux incident at the top of the canopy (E_{sun}), and $P_s(x)$ is the probability of leaves or soil being sunlit (or the gap fraction in the solar direction), which is given by $P_s(x) = \exp(-kLx)$, where x is the relative optical height ($[-1, 0]$, where -1 is at the soil surface and 0 at TOC), k is the extinction coefficient in the direction of the sun, and L is the LAI

For diffuse upward and downward fluxes the relationship is slightly more difficult because they are highly intertwined, as is shown in equation (4-2):

$$\frac{d}{Ldx} \begin{pmatrix} E^- \\ E^+ \end{pmatrix} = \begin{pmatrix} a & -\sigma \\ \sigma & -a \end{pmatrix} \begin{pmatrix} E^- \\ E^+ \end{pmatrix} + \varepsilon_v \begin{pmatrix} -H_c \\ H_c \end{pmatrix} \quad (4-2)$$

where a is the attenuation coefficient, σ the backscatter coefficient, ε_v the emissivity of the leaves (canopy), and H_c the black body emittance. This equation can be simplified into equation (4-3) using the transformed fluxes, $F_1 = E^- - r_\infty E^+$ and $F_2 = -r_\infty E^- + E^+$, with the

infinite reflectance, $r_\infty = (a - m)/\sigma$, and the eigenvalue of the diffuse flux system, m . The advantage of working with transformed fluxes is that these can be directly expressed in the ones of the layer above or below.

$$\begin{aligned}\frac{d}{Ldx} F_1 &= mF_1 - m(1 - r_\infty)H_c \\ \frac{d}{Ldx} F_2 &= -mF_2 + m(1 - r_\infty)H_c\end{aligned}\quad (4-3)$$

The solution of this set of coupled equations can be found when omitting the thermal radiation and adding the direct solar flux. After some rearrangement the analytical solutions are given in equation (4-4). In this equation the modification of (Verhoef and Bach, 2007) is implemented by means of J_1 and J_2 , to ensure numerical stability.

$$\begin{aligned}F_1(x) &= \delta_1 e^{mLx} + (s' + r_\infty s)E_s(0)J_1(k, x) \\ F_2(x) &= \delta_2 e^{-mL(1+x)} + (r_\infty s' + s)E_s(0)J_2(k, x)\end{aligned}\quad (4-4)$$

where s is the backscatter coefficient for solar radiation, s' the forward scatter coefficient for solar radiation, J_1 and J_2 are numerically stable functions as described in (Verhoef and Bach, 2007), and δ_1 and δ_2 boundary constants.

The coefficients m , s , s' and r_∞ in equation (4-4) depend on the leaf inclination distribution, and the transmittance and reflectance of the leaves. The spectral transmittance and reflectance of the leaves are calculated with the model PROSPECT (Jacquemoud and Baret, 1990; Jacquemoud *et al.*, 1996), using the concentrations of leaf water, chlorophyll, dry matter, and brown pigment, as well as the leaf Mesophyll scattering parameter N , as input parameters. The soil's reflectance spectrum is another required input. In this study, a standard spectrum for loamy sandy soil was used.

4.2.3 Internally generated thermal radiation

The incident radiation on leaves should not only include the optical and thermal radiation from sun and sky, but also all thermal radiation generated internally by leaves and by the soil. In (Verhoef *et al.*, 2007) the thermal domain was treated by means of an analytical solution, which assumed distinct, but otherwise constant, temperatures of sunlit and shaded leaves, as well as sunlit and

shaded soil. As shown in Chapter 3, it is to be expected that in reality all leaves will each have a different temperature, depending on their orientation with respect to the sun, and their vertical position in the canopy layer. Therefore, a numerical solution allowing more temperature variation is preferred. To accomplish this, the energy balance equation is solved at individual leaf level.

For the numerical solution of this problem, the coupled set of transformed differential equations, is again used as a starting point but without omitting the thermal component. In this case the average hemispherical fluxes from leaves and soil are presented in the equations (4-5) and (4-6), respectively:

$$H_c(x) = [1 - P_s(x)]H_{cd}(x) + P_s(x) \frac{1}{N_{\varphi_l} \sum_{N_{\theta_l}}^{N_{\varphi_l}} f(\theta_l) H_{cs}(x, \theta_l, \varphi_l)} \quad (4-5)$$

$$H_s(-1) = [1 - P_s(-1)]H_{sd} + P_s(-1)H_{ss} \quad (4-6)$$

where N_{φ_l} is the number of azimuthal leaf orientations, N_{θ_l} is the number of zenith leaf orientations, H_{cs} is the thermal flux emitted by individual sunlit leaves and H_{cd} is the thermal flux emitted by individual shaded leaves, H_{ss} is the thermal flux emitted by sunlit soil and H_{sd} is the thermal flux emitted by shaded soil. By default, the number of leaf azimuth angles is set to 36 and the number of leaf zenith angles is set to 13.

Using the diffusive fluxes reflected by the soil, $E^+(-1) = r_s E^-(-1) + (1 - r_s)H_s$, a numerical solution can be found for equation (4-4). The coupled set of equations (4-7) and (4-8), with boundary conditions (4-9) and (4-10), respectively, at the top ($x = 0$) and at the bottom ($x = -1$) are used for this.

$$F_1(x - \Delta x) = (1 - mL\Delta x)F_1(x) + m(1 - r_\infty)H_c(x)L\Delta x \quad (4-7)$$

$$F_2(x + \Delta x) = (1 - mL\Delta x)F_2(x) + m(1 - r_\infty)H_c(x)L\Delta x \quad (4-8)$$

$$F_1(0) = -r_\infty F_2(0) \quad (4-9)$$

$$F_2(-1) = \frac{(r_s - r_\infty)}{(1 - r_s r_\infty)} F_1(-1) + \frac{(1 - r_\infty^2)}{(1 - r_s r_\infty)} (1 - r_s)H_s \quad (4-10)$$

This set of coupled equations can be solved through iteration, with the initial assumption of absence of incoming thermal radiation $F_1(0) = 0$. Note that incoming thermal radiation from the sky has not been neglected but has been dealt with by the semi-analytical solution described in section 4.2.2.

4.2.4 Net radiation

The net radiation R_n of a leaf is equal to the total absorbed incident radiation minus its total emission from both sides. The leaf's emitted fluxes are defined for leaves in the shade and in the sun. For leaves in the shade the emittance depends only on the vertical position. Leaves in the sun will each have a different temperature and thermal emittance, depending on their orientation and vertical position. The equations for shaded and sunlit leaves are shown in, respectively, equation (4-11) and (4-12).

$$R_n(x) = (1 - \rho - \tau) [E^-(x) + E^+(x) - 2H_{cd}(x)] \quad (4-11)$$

$$R_n(x, \theta_\ell, \varphi_\ell) = (1 - \rho - \tau) [f_s |E_{\text{sun}} + E^-(x) + E^+(x)| - (1 - \rho - \tau) [2H_{cs}(x, \theta_\ell, \varphi_\ell)]] \quad (4-12)$$

where ρ and τ are the reflectance and the transmittance of the leaf, which are used to calculate the emissivity and the absorption according to Kirchoff's Law, $\varepsilon = \alpha = 1 - \rho - \tau$; and f_s is the leaf area projection factor in the direction of the sun, which can be calculated using the solar zenith angle and the leaf orientation angles (slope and azimuth)

4.2.5 The energy balance

The available energy, as characterised by the net radiation, drives the biochemical processes, such as transpiration and the exchange of heat. An energy balance model distributes net radiation over turbulent air fluxes and heat storage. The energy balance equation for each element i is given by:

$$R_n^i - G^i - H^i - \lambda E^i = 0 \quad (4-13)$$

where H is sensible heat flux [W m^{-2}]; λE is latent heat flux [W m^{-2}]; G is the change in heat storage [W m^{-2}]. In this equation, energy involved in the melting of snow and freezing of water is not

considered, and energy involved in chemical reactions is neglected, since it is usually one or two orders of magnitude smaller than net radiation. Heat storage is considered for the soil only (the heat capacity of leaves is neglected).

Soil heat flux at the surface is calculated with a discrete version of the force restore method (Bhumralkar, 1975). The other fluxes are calculated from the vertical gradients of temperature and humidity for soil or foliage in analogy with Ohm's law for electrical current:

$$G = \frac{\Gamma}{\sqrt{2\omega\Delta t}} \left(|T_s(t + \Delta t) - T_s(t)| + \omega\Delta t [T_s(t) - \bar{T}_s] \right) \quad (4-14)$$

$$H = \rho_a c_p \frac{T_s - T_a}{r_{ak}} \quad (4-15)$$

$$\lambda E = \lambda \frac{q_s(T_s) - q_a}{r_{ak} + r_{ck}} \quad (4-16)$$

where ω is the frequency of the diurnal cycle [rad s^{-1}], Γ the thermal inertia of the soil [$\text{J K}^{-1}\text{m}^{-2}\text{s}^{-1/2}$], \bar{T}_s the average annual temperature, ρ_a the air density [kg m^{-3}], c_p the heat capacity [$\text{J kg}^{-1}\text{K}^{-1}$], λ the evaporation heat of water [J kg^{-1}], T_s the temperature of an element [$^{\circ}\text{C}$], T_a the air temperature above the canopy [$^{\circ}\text{C}$], q_s the humidity in stomata or soil pores [kg m^{-3}], q_a the humidity above the canopy [kg m^{-3}], r_c the stomatal or soil surface resistance [s m^{-1}], and r_a the aerodynamic resistance. This aerodynamic resistance is calculated with the two-source model (Wallace and Verhoef, 2000), as illustrated in Figure 4-3.

The energy balance is closed by iteration over the skin temperatures of the different components. The aerodynamic and stomatal resistance are both included in the iteration, since atmospheric stability and biochemical processes are affected by leaf temperature. For numerical stability, a weighted average of the estimates for T_s of the two previous iteration steps is used in the next iteration step. Iteration continues until the absolute difference in net radiation between two consecutive iterations is less than the required accuracy for all surface elements.

4.2.6 Leaf biochemistry

Leaf biochemistry affects biophysical processes, such as transpiration, photosynthesis, stomatal resistance, and chlorophyll fluorescence. The associated biophysical variables do not only depend on the chemical composition of the leaf, but also on environmental constraints such as illumination, leaf temperature, and air humidity.

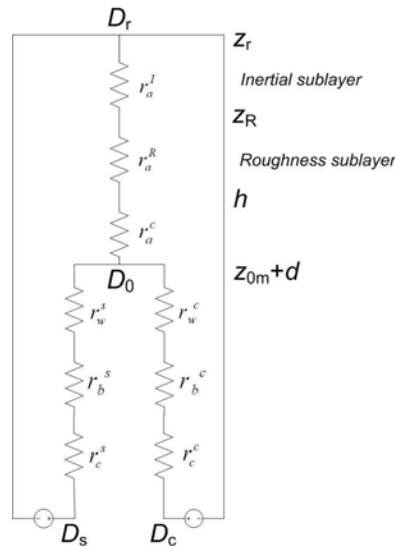


Figure 4-3: Schematic representation of a two-source resistance model.

This model takes into account the resistance to water vapour and heat transport in and above the canopy. The letter 'D' refers to either temperature (T) or absolute humidity (q). Other symbols are defined in Table 1.

The nonlinear response of these biophysical variables to environmental constraints is calculated with the biochemical model of (van der Tol *et al.*, 2009b). This model simultaneously calculates the photosynthesis of C3 (Farquhar *et al.*, 1980) or C4 vegetation (Collatz *et al.*, 1992), stomatal resistance (Cowan, 1977), and chlorophyll fluorescence.

The four most important parameters of the biochemical model are the carboxylation capacity $V_{c,max}$, the electron transport capacity J_{max} , the dark respiration rate R_d (all in $\mu\text{molm}^{-2}\text{s}^{-1}$), and the marginal water cost of photosynthesis λ_c . The first three of these parameters are temperature dependent (Farquhar *et al.*, 1980) and consequently the

biophysical model is also incorporated into the skin temperature iteration.

Note that currently the parameters of the biochemical model are defined independently from the PROSPECT parameters. The number of dimensions in parameter space could be reduced by relating PROSPECT parameters for the optical domain, such as chlorophyll content, to biochemical parameters, such as photosynthetic capacity. This would make it possible to extract information about photosynthetic capacity from the optical domain.

4.2.7 Top of canopy radiance spectra

Finally hyperspectral TOC spectral radiance is calculated for each component (sunlit/shaded soil/leaf), using the direct and diffuse radiances, the skin temperature of the different components, and the fluorescence of the photosynthesis. These are obtained from the spectral radiance of single leaves by integrating the latter over canopy depth and leaf orientation. The TOC radiance contribution is given for sunlit leaves, equation (4-17); shaded leaves, equation (4-18); and sunlit and shaded soil, equation (4-19):

$$\pi L_{\ell d} = \frac{LAI}{N_{layers}} \frac{1}{N_{\varphi_l}} \sum_{\substack{N_{\theta_l} \\ N_{\varphi_l} \\ N_{layers}}} \left\{ \begin{array}{l} 0 \\ + K(\theta_l, \varphi_l) \varepsilon_c H_{cd}(x) [P_o(x) - P_{so}(x)] \\ + [vE^-(x) + v'E^+(x)] P_o(x) [1 - P_s(x)] \end{array} \right\} f(\theta_l) \quad (4-17)$$

$$\pi L_{\ell s} = \frac{LAI}{N_{layers}} \frac{1}{N_{\varphi_l}} \sum_{\substack{N_{\theta_l} \\ N_{\varphi_l} \\ N_{layers}}} \left\{ \begin{array}{l} wE_s(0)P_{so}(x) \\ + K(\theta_l, \varphi_l) \varepsilon_c H_{cs}(x, \theta_l, \varphi_l) P_{so}(x) \\ + [vE^-(x) + v'E^+(x)] P_o(x) P_s(x) \end{array} \right\} f(\theta_l) \quad (4-18)$$

$$\pi L_s = [r_s E^-(-1) + \varepsilon_s H_{sd}] P_o(-1) + [r_s E_s(0) + \varepsilon_s (H_{ss} - H_{sd})] P_{so}(-1) \quad (4-19)$$

where N_{layers} is the number of layers (by default 60); K is the extinction coefficient in the observation direction; v and v' are the scattering coefficients in the observation direction due to the contributions from downward and upward diffuse flux; w is the bi-directional scattering coefficient for solar incident radiation; $P_o(x)$ is the gap fraction in the observation direction and $P_{so}(x)$ is the bi-directional gap fraction (the probability of viewing sunlit leaf or soil elements at level x).

In the final result, the analytical SAIL model is used for the contributions from solar and sky irradiance, excluding the internally generated thermal radiation. Using the canopy-level directional reflectances for direct and diffuse radiation in the observation direction r_{so} and r_{do} , the formulation becomes:

$$\begin{aligned} \pi L_o(0) = & r_{so} E_{\text{sun}} + r_{do} E_{\text{sky}} + \\ & K \varepsilon_c \sum_{Nx} H_{cd}(x) [P_o(x) - P_{so}(x)] + \\ & \frac{LAI}{N_{\text{layers}}} \frac{1}{N_{\varphi_l}} \varepsilon_c \sum_{\substack{\theta_l \\ \varphi_l \\ \text{layers}}} K(\theta_l, \varphi_l) H_{cs}(x, \theta_l, \varphi_l) f(\theta_l) P_{so}(x) + \\ & \varepsilon_s H_{sd} P_o(-1) + \varepsilon_s (H_{ss} - H_{sd}) P_{so}(-1) \end{aligned} \quad (4-20)$$

4.3 Output of SCOPE

A case study over a maize field in Sonning, United Kingdom, has been performed to show the full potential of the SCOPE model. This study area not only provides a lot of input data, but validation measurements as well. The site consists of two maize fields: a typical fully grown maize crop (LAI = 3.22) and a sparse maize crop (LAI = 0.25). In this study data from The University of Reading were used. The input data are listed in Table 4-1. The input spectra of Figure 4-2 were used, albeit linearly scaled to make the total incoming shortwave (0.4-2.5 μm) radiation match the measured value of 646 W m^{-2} .

4.3.1 Spectra

Figure 4-4 shows the output spectrum (in nadir direction) over the maize field. The upper graph shows the results for the optical range (excluding fluorescence), the middle graph the results for the thermal range, and the lower graph shows chlorophyll fluorescence.

The optical spectrum of the fully grown canopy is typical for green vegetation (Carter and Knapp, 2001), whereas the spectrum for the sparse canopy represents a mixture of bare soil and vegetation. In the thermal spectrum, the presented scenarios closely resemble Planck's curve. This is because the emissivity was not differentiated spectrally. The differences between the two scenarios are the

combined result of differences in reflected thermal radiation, and canopy and soil temperatures. In the sparse canopy a larger portion of the soil is visible. Soil has a lower emissivity than leaves, thus reducing the radiance of the sparse canopy compared to that of the fully grown canopy. This is compensated for by both soils and leaves having higher temperatures in the sparse canopy than in the fully grown canopy.

Table 4-1: The SCOPE input variables for the Sonning Maize simulations.

Parameters C_{ab} , C_{dm} , C_s and N are PROSPECT parameters and refer to chlorophyll content, dry matter content, senescent material, and leaf structure, respectively. $LIDF_a$ and $LIDF_b$ are leaf angle distribution parameters. The values in the table refer to a spherical distribution of leaves.

Vegetation Parameters	Value	Unit	Parameter	Value	Unit
C_{ab}	60	$\mu\text{g cm}^{-2}$	$V_{c\text{max}}$	50	$\mu\text{mol m}^{-2} \text{s}^{-1}$
C_{dm}	0.012	g cm^{-2}	V_{pmo}	220	$\mu\text{mol m}^{-2} \text{s}^{-1}$
C_w	0.009	cm	J_{max}	120	$\mu\text{mol m}^{-2} \text{s}^{-1}$
C_s	0.0		λ_c	700	
N	1.4		h	1.0	m
$LIDF_a$	-0.35		ρ (ther.)	0.01	
$LIDF_b$	-0.15		τ (ther.)	0.01	
LAI	3.22 , 0.25		ρ_s (ther.)	0.06	
Meteor. variables					
U	2.9	m s^{-1}	q_a	9.3	kg
T_a	21.4	$^{\circ}\text{C}$	R_{in}	646	W m^{-2}

The chlorophyll fluorescence spectra show two peaks, one in the red (690 nm) and one in the far red (730 nm). The ratio between the first and the second peak usually decreases with increasing chlorophyll content due to re-absorption within the leaf (Buschmann, 2007). In the current simulations, the increased re-absorption within the leaf is not included, as the same fluorescence matrices for the up- and downside of a leaf were applied as input. However, the (minor) effect of re-absorption by other leaf layers is included, which causes the ratio of the first over the second peak to be slightly higher in the

sparse canopy than in the fully grown canopy. The order of magnitude of the fluorescence fluxes agrees well with recent measurements: (Campbell *et al.*, 2008) found peak values of 2 to 5 $\text{W m}^{-2} \mu\text{m}^{-1} \text{sr}^{-1}$ for a maize crop.

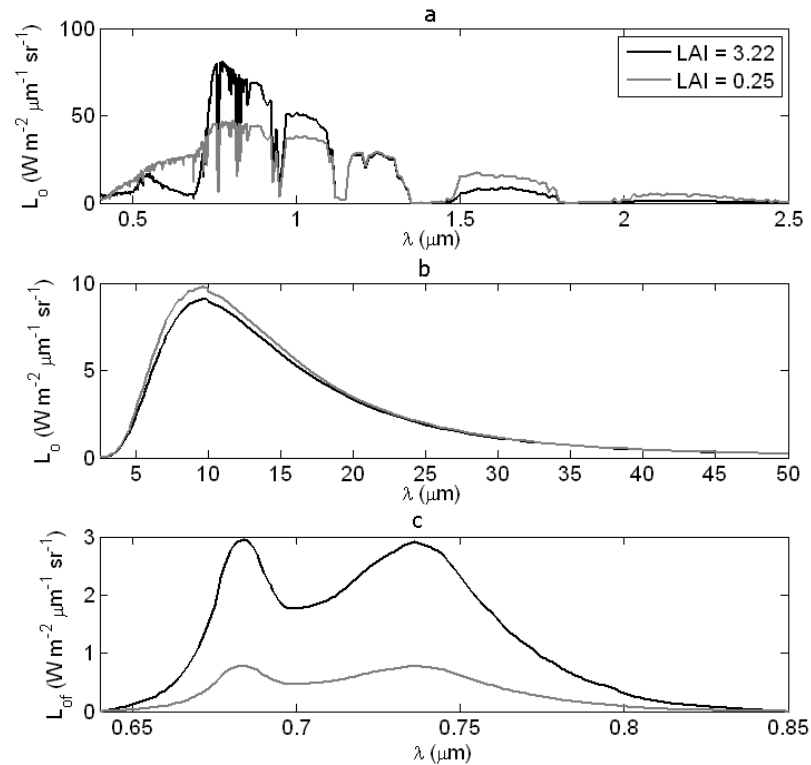


Figure 4-4: Nadir outgoing TOC optical and thermal radiance. In (a) the outgoing optical radiation is shown; in figure (b) outgoing thermal radiance is shown; and in (c) the outgoing radiation from fluorescence is shown. Two scenarios of a C4 canopy are shown: low LAI and high LAI. The relevant parameters are listed in Table 4-1.

4.3.2 Directional radiance

SCOPE was designed to simulate directional signatures. Figure 4-5 shows the directional behaviour of reflectance, brightness

temperature and fluorescence for the two scenarios presented in Figure 4-4.

Both the sparse and the fully grown canopy show a large directional signature. In the optical spectrum, the BRDF in the NIR decreases between fully grown maize and sparse maize. This is because the soil has a lower reflection (800nm) than the leaves. In the thermal region the brightness temperature increases with the viewing angle, the reason being that at horizontal viewing angles the largest fraction of (relatively warm) sunlit vegetation becomes visible. This effect is most pronounced in the sparse vegetation, because there the differences in temperature between sunlit and shaded vegetation are the largest (Figure 4-6). In the fluorescence spectrum the directional effect is also present because the upper leaves contribute more to the total chlorophyll fluorescence than the lower leaves. This causes the observed fluorescence to increase with increasing viewing angles.

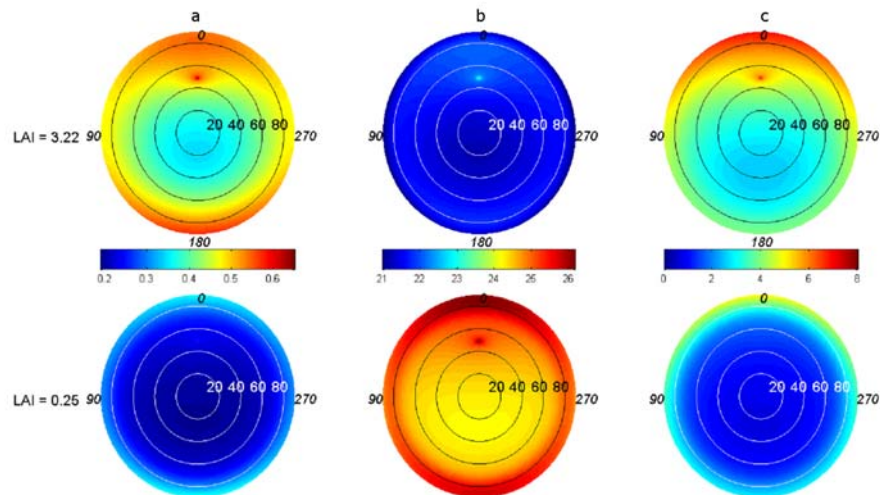


Figure 4-5: Directional signatures of Reflectance, Fluorescence and Emission.

In (a) the BRDF is shown in the NIR, in (b) the directional brightness temperature is shown; and in (c) the chlorophyll directional fluorescence radiance is shown. Observation zenith angle varies with the radius; the azimuth angle (in italic) increases while rotating anticlockwise from north. These graphs are based on the same scenarios as Figure 4-4 with a solar zenith angle of 48 degrees

4.3.3 Vertical profiles

The full potential of the SCOPE model is best illustrated by plotting the within canopy vertical profiles of temperature, Figure 4-6. Values represent the average temperature per layer for the sunlit fraction, the shaded fraction, and the weighted average temperature.

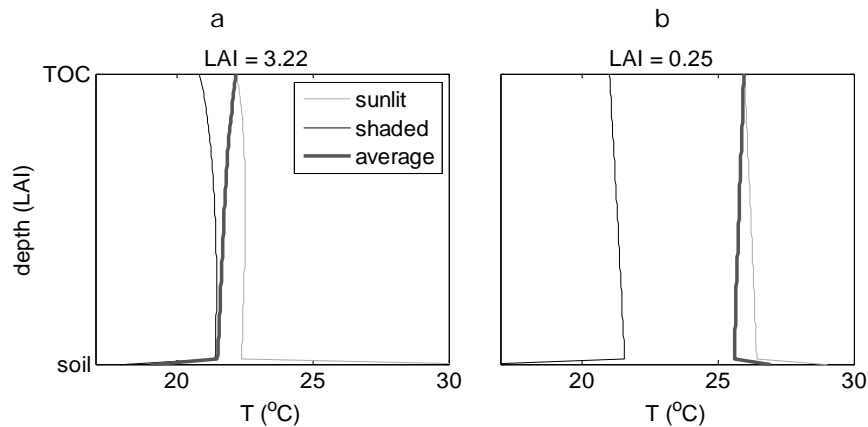


Figure 4-6: Vertical profiles of skin temperatures of leaves and soil.

Here TOC denotes top of canopy. Temperatures are averages over a single layer, with the exception of the soil temperatures. The vertical axis scales linearly with leaf area index. These graphs (a and b) are based on the same scenarios as Figure 4-4.

The temperature of both sunlit and shaded leaves increases with the depth into the canopy (from top to bottom of the graph), whereas the weighted mean temperature decreases with depth. This is caused by shaded leaves being more abundant than sunlit leaves lower in the canopy, and the weighted temperature approaching this value.

The sparse canopy has higher leaf temperatures than the fully grown canopy, both for the shaded and the sunlit fraction. This effect is caused by the high net radiation of the soil, resulting in higher soil contact temperatures, which then also affect the canopy layer above through a higher emittance received from below.

The vertical profiles are sensitive to variations in irradiance regime as well as weather conditions. Different vertical profiles of the fully grown maize field resulted from (1) a fivefold increase in wind speed

(15 ms⁻¹), and (2) replacement of all direct radiation with diffuse radiation (Figure 4-7). Not only the vertical profiles of temperature change, but there is also considerable variation in the vertical profiles of photosynthesis and latent heat.

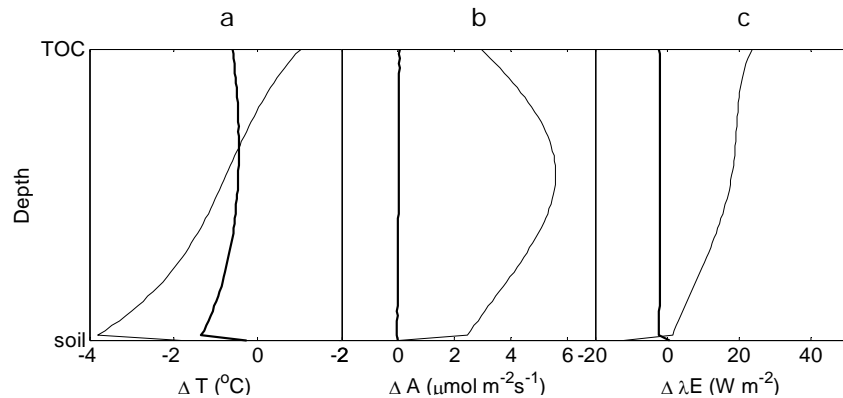


Figure 4-7: Sensitivity of vertical profiles of biophysical processes.

The effect of increasing wind speed from 2.9 m s⁻¹ to 15 m s⁻¹ (bold line), and the effect of replacing all direct radiation by diffuse radiation -with total radiation remaining unchanged- (fine line), for the fully grown maize canopy of Fig. 3. The graphs show the difference in the vertical profiles of leaf and soil temperatures (a), net photosynthesis (b) and latent heat flux (c) compared to the reference scenario.

Wind speed has a significant effect on temperature, but only a minor effect on the fluxes; the decrease in aerodynamic resistance as wind speed increases is counterbalanced by a simultaneous decrease in the vapour and carbon dioxide gradient. The distribution of radiation over direct and diffuse radiation has a significant effect on both the temperature and the fluxes. This result confirms that photosynthetic light use efficiency is higher for diffuse than for direct radiation, also if the magnitude of incident radiation is the same

4.4 Discussion and Conclusion

In this chapter the Soil Canopy Observation of Photochemistry and Energy fluxes (SCOPE) model is presented. This new model integrates detailed radiative transfer, based on the SAIL model, with different biophysical processes, such as evapotranspiration and photosynthesis. The coupling between the models is performed by an

energy balance at leaf level. The modular structure of SCOPE makes it possible to add new features by simply sharing input, output and parameters with other models.

This model is able to simultaneously simulate both the optical and the thermal spectrum at hyperspectral resolutions and at different viewing angles. It is also the first model that includes the modelling of chlorophyll fluorescence in relation with leaf photosynthesis and physiology. Inverting the measured values of these (directional) spectra will dramatically reduce the inversion problem and increase our understanding of the biophysical processes on the earth's surface.

In addition, SCOPE is able to interpolate fluxes between satellite overpasses. The model can run in the absence of remote sensing information, which makes it possible to not only scale from instantaneous data to diurnal cycles, but also to calculate the fluxes for cloudy days, when reliable remote sensing data are not available.

5 Validation of radiative transfer in SCOPE

Based on

Timmermans J., Gastellu-Etchegorry J.P., van der Tol C., Verhoef W., Vekerdy Z., and Su, Z., Directional radiative transfer by SCOPE, SLC and DART using laser scan derived structural parameters of forest (in preparation).

Abstract

In this chapter the radiative transfer of the SCOPE model is evaluated. This SCOPE radiative transfer component is estimated using a discrete version of the SAIL model. Although the analytical SAIL model has been validated several times, the discrete version of this RTM has never been validated. The evaluation of the discrete unified SAIL model in SCOPE is therefore compared with different simulations by the DART 3D radiative transfer model. The DART simulations represent several scenarios with increasing complexity, from very simple 'Bare soil', 'Plot' and 'Homogeneous crown' scenarios, through medium complexity 'Layered crown' and 'Elevated layered crown', to complex 'Multiple crown' scenarios. The scenarios were created using structural parameters acquired on the basis of terrestrial laser scan data of the Speulderbos forest.

A comparison was also performed between the Soil Leaf Canopy (SLC) and the SCOPE model. SLC is an RTM based on the analytical SAIL model with extra parameterizations for crown clumping. The comparison revealed that the SCOPE model employed an older version of the hotspot characterisation and that a correction term for the finite height of the layers was not applied either. After modification the difference between the two models was less than 1% for all but the most oblique viewing angles.

The comparison between SCOPE and DART showed good agreement for crown covers larger than 0.93, with maximum errors of 6.77% and 5.96% for 750nm and 1750nm, respectively. The largest contribution to this error occurred near the hotspot viewing angle. Scenarios with a crown cover smaller than 0.93 showed errors larger than the threshold value of 7.5%. The comparison between SLC and DART showed that better agreement for more complex scenarios; for a crown cover of 0.87 the results were 6.66% and 7.12%. For smaller crown covers DART showed a large increase in azimuthal dependence and consequently the differences with SLC increased. The validation showed that SCOPE is applicable to a large set of canopies, but must be updated to resemble SLC for more complex canopies.

5.1 Introduction

In the previous chapter the SCOPE model (van der Tol *et al.*, 2009c) was presented for the estimation of land atmosphere fluxes and directional radiative transfer. Validation of this model is required before this SVAT model can be used for real life applications. The model consists of several components modelling different processes within the canopy: photosynthesis (Farquhar *et al.*, 1980; Collatz *et al.*, 1992), radiative transfer (Verhoef *et al.*, 2007) and leaf fluorescence (van der Tol *et al.*, 2009b). Each of the biochemical model components has been validated separately. In addition the original SAIL model has been validated several times (Pinty *et al.*, 2001; Pinty *et al.*, 2004; Widlowski *et al.*, 2007).

However, the SAIL RTM component of the SCOPE model is different from the original method (Verhoef *et al.*, 2007). In SCOPE a discrete version of the unified SAIL model is used, which needs to be re-evaluated. The main objective of this research was to investigate the limitations of the RTM part of the SCOPE model over complex canopies.

Accurate estimation of the radiative transfer (RT) over complex vegetation is extremely important in SVAT models, as radiation is both a forcing element and employed as an observation medium in such models. This dualism causes uncertainties in the estimation to propagate into the biochemical model and consequently to have a huge impact on the characterization of the biophysical processes. Note that in the recent SVAT models, like CUPID, this is circumvented by using other models for RS observation. However these models each have their own uncertainty and combined use of several satellites can not be performed.

The accuracy of the estimation of the biophysical processes and land surface properties is influenced by the complexity of the retrieval methods. Rautiainen (Rautiainen, 2005) divided biophysical parameter retrieval methods into two groups: statistical (like vegetation indices) and physical radiative transfer models (RTM). The advantage of RTMs over statistical methods is that they are able to capture the underlying radiative processes that are directly linked to the canopy architecture through the directional reflectance/emittance signatures. In addition, most statistical methods depend on one particular sensor, while RTMs do not suffer this drawback. The

application of RTM instead of statistical models is therefore apparent. However, the accuracy of a RTM is highly dependent on agreement of the model parameters with the real-life scenarios (Widlowski *et al.*, 2007). For example, complex models, like Radiosity (Liu *et al.*, 2007a) and DART (GastelluEtchegorry *et al.*, 1996; Gastellu-Etchegorry *et al.*, 2004; Gastellu-Etchegorry, 2008) that rely on detailed descriptions of Earth scenes are expected to be very accurate, and thus can be considered as reference models. However, their need for a high number of detailed (structural) parameters limits their applicability. Thus, for many remote sensing applications, there is a clear need of medium complexity models, like the SAIL and SLC models (Verhoef, 1984; Verhoef & Bach, 2007), which are able to simulate remote sensing measurements with a much smaller set of input parameters. Consequently, these medium complexity RTMs are easier to handle and to invert. Unfortunately, they tend to be less valid when canopy complexity increases. The choice for a RTM consequently depends on the constraints posed by the application.

An important point is to be able to assess the domain of validity of medium complexity RTMs. In this investigation the domains of validity of two medium complexity radiative transfer models in the case of complex vegetation canopies is explored. Although an independent model comparison was achieved in the RAMI framework (Pinty *et al.*, 2001; Pinty *et al.*, 2004; Widlowski *et al.*, 2007), only a limited number of scenarios was investigated. Thus, there is a real need to assess the domain of validity of the SCOPE model, especially in the case of structurally complex canopies.

In order to simulate BRDFs over structurally complex canopies a dataset of structural parameters is required. Measuring techniques are usually very time-consuming, as they involve measuring to scale and a protractor. Modelling approaches, such as L-systems (Lindenmayer.A, 1968) and plant growth models (Disney *et al.*, 2006) may also be used, but rely on data unavailable in this research. Laser scanning is a new measuring technique that is both fast and safe. The technique in past researches was used for urban planning (Oude Elberink and Vosselman, 2006), but more recently others have used this technique for, for instance, biomass surveys (Naesset, 1997), soil roughness modelling (Perez-Gutierrez *et al.*, 2007) and canopy structure retrieval (Pfeifer *et al.*, 2004; Pfeifer and Briese, 2007; Wehr, 2008).

In addition, a comparison between the Soil Leaf Canopy (SLC) (Verhoef and Bach, 2007) RTM and SCOPE was performed. Although both SCOPE and SLC are based on the SAIL RTM, the SLC model is

able to estimate the radiative transfer over clumped vegetation and for different shape factors. Also, the SCOPE model incorporates a discrete version of the SAIL RTM, whereas the SLC model incorporates the original analytical solution. The comparison between the SLC and the SCOPE model therefore provides an estimation of the errors introduced by this discretization.

The methodology of the research is described first, explaining the comparison, theoretical background of the parameter retrieval algorithm and the RTM models in detail. Secondly, the results of the comparison between SCOPE and SLC simulations are discussed. Thirdly, different DART scenarios are compared to each other, and finally the SCOPE and SLC simulations are compared with the DART scenarios.

5.2 Methodology

Ideally the validation of a radiative transfer model is performed with ground measurements. However during the directional measurements in the field not all the structural parameters are usually measured. Cross validation between the RTMs is therefore the preferred option. DART was chosen as preferred RTM for the comparative study, as it is able to simulate different types of canopies and multiple trees. It should be noted that cross validation between the models will not provide the absolute accuracy of the SAIL model, but only the relative difference between the two models.

The approach in this research, see Figure 5-1, was as follows:

1. Estimation of the 3D structural parameters: the structural parameters were estimated using point cloud data from a terrestrial laser scanner. This data was fed through a series of reconstruction algorithms and filters to estimate tree positions, crown size, and the vertical leaf area distribution. This is explained in more detail in section 5.2.1.
2. Radiative transfer simulations: DART, SLC and SCOPE scenarios were considered.
 - a. Different DART scenarios: the structural parameters estimated using terrestrial laser scanning were used to create different DART scenarios. The scenarios ranged from bare soil, and very homogeneous canopies, through to structural complex canopies (section 5.2.3.1).
 - b. The SCOPE canopy scenario was simulated using two different versions of the bidirectional gap fraction for both bare soil and canopy covered land surfaces.

- c. The SLC scenario was simulated for non-clumped and clumped crowns. Clumping was executed using crown cover (from DART simulations) and the shape factor (a priori calculated) as input.
3. Inter and cross comparisons between the different models were performed using the relative root mean square difference (equation (5-1)), correlation coefficients and biases. The comparison focussed on different classes: Nadir (N) observing viewing angles, Hotspot (H) and Near-hotspot (NH) viewing angles, as well as Cross principle Plane (CP) and Along principle Plane (A) viewing angles (without the previous classes). First the SCOPE model was compared with the SLC model (section 5.3.2). Then, in section 5.3.4, DART scenarios were compared with each. Finally, the different DART scenarios were compared with the SCOPE (section 5.3.5) and SLC (section 5.3.6) simulations.

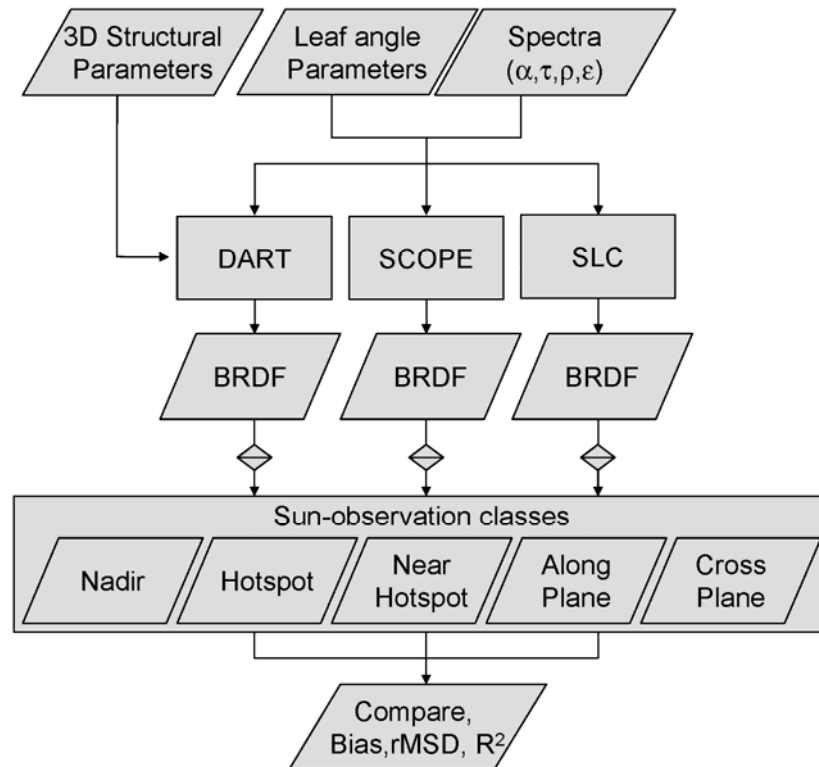


Figure 5-1: Flowchart of the Simulations

The reflectance spectra and leaf inclination distribution functions used in the SAIL and SLC models were the same as in the DART simulations.

$$rMSD(\Omega_s, \Omega_i, \lambda) = \left\langle \frac{BRDF_{ref}(\Omega_s, \Omega_i, \lambda) - BRDF_j(\Omega_s, \Omega_i, \lambda)}{BRDF_{ref}(\Omega_s, \Omega_i, \lambda)} \right\rangle^{0.5} \cdot 100\% \quad (5-1)$$

where Ω_s denotes the solar angles in 32 time steps from sunrise to sunset, Ω denotes the different observation angle groups, and λ is the wavelength. For the comparison between SCOPE/SLC and DART a threshold value for the rMSD of 7.5% was used. This threshold was set based on experience.

5.2.1 Laser scanning

Laser scanning is a promising tool for estimating structural parameters with simple reconstruction algorithms (Gorte and Pfeifer, 2004). These reconstruction algorithms use 3D kernels to process the data. The kernels are the 3D equivalent of 2D kernels used in image processing, such as filtering and neighbourhood operators. The structural parameters needed for this research were the detailed crown shapes, the positions of the trees and the leaf area vertical distribution.

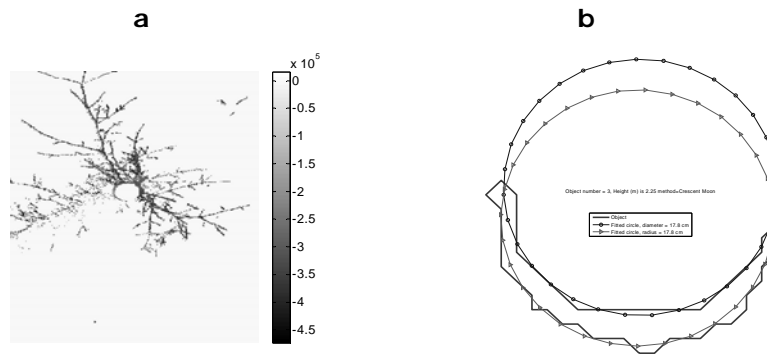


Figure 5-2: Crescent Moon Fitting of on a point cloud acquired by laser scan.

In panel (a) the shadowing effect is illustrated; even after the erroneous-cell filling the tree trunk does not show as a circular object; panel (b) illustrates the algorithm (on a different tree) to retrieve the tree trunk diameter from a partial tree with a crescent moon shape. Two circles are fitted to the crescent moon; the blue circle illustrates the fit to the inner part of the crescent moon, the green circle illustrates the fit to the outer part of the crescent moon.

One of the biggest problems with laser scanning is the filling of erroneous empty cells. These empty cells appear in the data due to the so-called shadowing effect of the laser scanner. The laser scanner cannot see behind objects and instead empty cells appear (similar to shadows). The appearance of empty cells can partially be circumvented through the use of multiple positions for the laser scanner (Pfeifer *et al.*, 2004). This, however, does not remove all shadows from the point cloud, especially at the edge of the area of interest. Small clusters of these empty cells can be corrected using neighbourhood operators to fill them. For larger clusters of erroneous cells crescent-moon fitting (Király and Brolly, 2007) is used to identify the full tree trunk. This method is based on the hypothesis that observed crescent moon shapes correspond to circular tree trunk shapes, as seen in Figure 5-2. The position and trunk diameter can therefore still be retrieved, although only part of the trunk is visible.

Other structural information such as branch-characteristics may be reconstructed (Gorte and Pfeifer, 2004; Pfeifer *et al.*, 2004). This however was not performed in this investigation because the DART RTM can use this information only since the 4.3 release in mid 2010. In addition to the spatial placement of the trees, a vertical profile of the laser scan reflections was extracted. This vertical profile

corresponded to the vertical leaf area distribution, after filtering out the branches (Vekerdy *et al.*, 2007).

5.2.2 SAIL

In addition to the radiative transfer part of the SCOPE model, SLC was incorporated into this comparison. Both the SCOPE (van der Tol *et al.*, 2009c) and SLC (Verhoef and Bach, 2007) models are based on the SAIL RTM (Verhoef, 1984). However SCOPE was created in order to provide high accuracy estimation of water, carbon dioxide and energy fluxes at the earth's surface using a detailed radiative transfer model, while SLC was created as an upgraded version of the SAIL (Verhoef, 1984), that could also simulate directional radiative transfer from the soil and clumped vegetation. Consequently there are two notable differences between the SLC and the SCOPE model.

- The first difference between the SCOPE model and the SLC model is that the SCOPE model uses a discrete form of the SAIL RTM in order to retrieve the biophysical processes at different levels of the canopy (van der Tol *et al.*, 2009c).
- The second difference between the SCOPE and SLC model is that the SCOPE model cannot yet characterize clumped vegetation, while it is possible to use the SLC model over clumped vegetation surfaces, through the use of the nadir crown cover C_v , and the tree shape factor ξ .

5.2.3 DART

The Discrete Anisotropic Radiative Transfer (DART) RTM is a complex model that is able to simulate the radiative transfer over complex structures in natural and urban environments (Liang, 2003). DART was developed by (GastelluEtchegorry *et al.*, 1996) on the basis of the discrete ordinate method (DOM), and is still upgraded regularly (Gascon *et al.*, 2001; Gastellu-Etchegorry *et al.*, 2004; Gastellu-Etchegorry, 2008) since its first release (Gastellu-Etchegorry *et al.*, 1996). It is used extensively in different research fields, (Malenovsky *et al.*, 2008), and has been validated several times (Pinty *et al.*, 2001; Pinty *et al.*, 2004; Widlowski *et al.*, 2007).

5.2.3.1 DART scenarios

In total, nine different scenarios were simulated with the DART RTM. These canopies describe six levels of increasing structural complexity, as illustrated by Figure 5-3. From the most simple to the most

complex the scenarios are 'Bare Soil', 'Plot', 'Homogeneous Crown', 'Layered Crown', '(Elevated) Layered Crown', and 'Multiple Crowns'. In the '(Elevated) Layered Crown' and the 'Multiple Crown' scenarios the layering within the crown was implemented using the vertical leaf area distribution. In order to investigate the clumping effect of the vegetation, 4 different 'Multiple Crown' scenarios were studied. They were implemented through a decrease of the tree crown diameters that were derived from laser measurements. According to the DART manual the 'Plot' and 'Homogeneous Crown' scenarios should provide the same output. In this research still these two scenarios were investigated against each other, to provide consistency between the different scenarios.

5.2.4 Simulation Parameters

In 2006, the EAGLE field campaign took place in the Netherlands (Su *et al.*, 2009). ESA organized this large international field campaign in the framework of the GMES program. This field campaign consisted of satellite, airborne and ground measurements over three field sites: an agricultural site, Cabauw, and two forest sites, Loobos and Speulderbos. Laser scan measurements took place only at the Speulderbos forest site. Therefore, the work that is presented here focuses on this site. The laser scan measurements were performed with a Leica HDS 2500 pulse scanner (Vekerdy *et al.*, 2007).

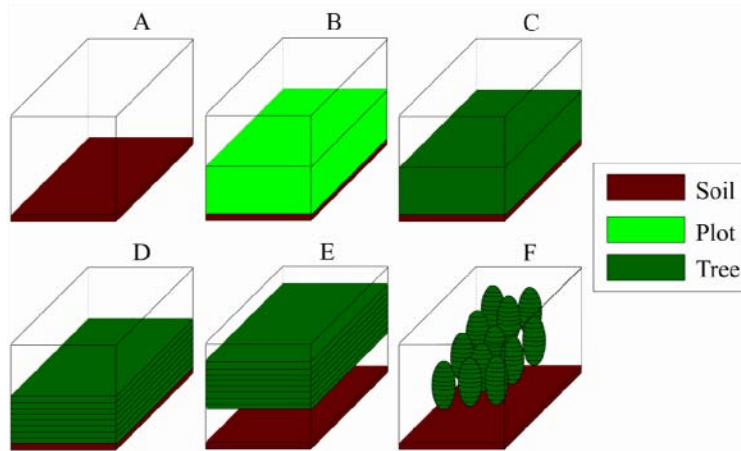


Figure 5-3: DART scenarios with increasingly complex structural characteristics.

Panel A describes the simulation containing 'Bare soil' (with Lambertian reflectance); Panel B shows the 'Plot' scenario; Panel C shows the 'Homogenous crown' scenario; Panel D shows the 'Layered Crown scenario'; Panel E shows the 'Elevated Layered Crown' scenario, and Panel F describes the 'Multiple Crown' scenario with both a vertical and a horizontal distribution.

Here, only the effects of different levels of structurally complex canopies on the BRDF are investigated. Variations in the BRDF caused by variations in leaf angles, single-leaf reflectance, or the non-Lambertian reflection of the soil are not taken into account. The simulations of SCOPE/SLC and DART therefore used the same spectral parameters. SCOPE, SLC and DART all can use the Prospect model for simulating the leaf spectrum. The input parameters common to all the three RTM models are given in Table 5-1.

The single leaf spectral reflectance (calculated by the Prospect model) and the soil spectral reflectance (from the DART database) are shown in Figure 5-4. At 750nm the soil reflectance was lower than the single leaf spectrum, while at 1750nm the soil reflectance was higher than the single leaf spectrum (shown in Figure 5-4 with two lines). These wavelengths were therefore chosen for the comparisons.

Table 5-1: Input parameters for DART, SCOPE and SLC

Leaf Parameters	Symbol	Value	unit
Leaf area index	LAI	5.00	m^2/m^2
Leaf inclination. Distr. Function	$LIDF$	Spherical	-
Hotspot parameter	q	0.0031	m/m
Spectral Parameters			
Soil spectrum	r_s	gravelly ⁴	-
Chlorophyll content	C_{ab}	60	$\mu g/cm$
Dry matter content	C_{dm}	0.012	g/cm
Water content	C_w	0.009	cm
Senescent material	C_s	0.000	-
Thickness parameter	N	1.4	-
SLC specific parameters			
Vertical Crown cover	C_v	1.0, 0.93, 0.87, 0.73, 0.58	-
Shape Factor	ξ	1.0, 0.28, 0.24, 0.20, 0.16	m/m

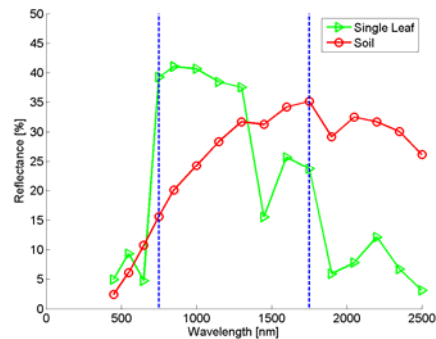


Figure 5-4: Soil and leaf spectrum in the SLC/SCOPE and DART simulations.

The lines denote the 750nm and 1750 nm wavelengths.

Note that, although both SLC/SCOPE and DART compute the hotspot effect according to Kuusk (Kuusk, 1991), there is a small difference in

⁴ From DART spectral database

the implementation. SCOPE/SLC uses the hotspot variable, $q = d_f / h$ as input, with d_f denotes the leaf diameter and h the height of the canopy; while DART uses the leaf diameter to calculate through an apparent leaf dimension the hotspot internally. For a canopy height of 16m and a leaf diameter of 0.05 the hotspot parameter is found to be 0.031.

DART is computationally intensive. A single run of a 'Multiple Crown' scenario takes roughly two hours. Therefore for the 'simple' scenarios ('Bare Soil', 'Plot', 'Homogeneous Crown' and the '(Elevated) Layered Crown') the horizontal spatial dimensions of the scenarios were changed. This could be done as the canopy covered the whole pixel, and a circular boundary condition was used. For the 'complex' scenarios the crown diameter was changed in order to simulate different crown clumpings. In the 'simple' scenarios the horizontal scene dimensions were set to 5.0m x 5.0m and for the complex scenarios the dimensions were set to 18.0m x 15.0m. In all the scenarios a cell horizontal and vertical dimension of 0.5m was used.

5.3 Results

5.3.1 Structural parameter retrieval

The retrieval algorithm produced 65 trees before filtering and 12 trees after filtering. Filtering was performed on the basis of the correlation between the inner and the outer diameter in adjacent levels. In Table 5-1 and Figure 5-5 the final results of the retrieval algorithm are shown. The standard deviation was calculated for different layers. The high standard deviation for trees 11 and 12 was caused by low hanging (dead) branches that could not be removed. Although these were first presumed to be false-positives, manual inspection of the point cloud data concluded otherwise.

Table 5-2: Results of the retrieval tree position algorithms. The table shows the position and the radius of the trunk, as well as the standard deviation of the trunk radius for the different trees.

Nr. Tree	X-coordinate [m]	Y-coordinate [m]	Mean Radius [m]	Std Radius [m]
1	- 06.643	-04.927	0.175	0.016
2	10.042	00.257	0.151	0.010
3	06.419	00.468	0.119	0.024
4	- 05.180	01.322	0.160	0.064
5	07.901	02.334	0.130	0.048
6	01.046	03.767	0.144	0.02
7	06.151	07.577	0.072	0.025
8	02.146	08.156	0.176	0.024
9	- 05.481	08.305	0.059	0.028
10	- 04.213	05.738	0.274	0.503
11	- 05.378	- 02.417	0.328	0.234
12	04.301	- 00.812	0.138	0.083

The leaf area vertical distribution was retrieved (see Figure 5-5) from the point cloud density. The high point density below a tree height of 20m corresponds with the dead branches in the canopy.

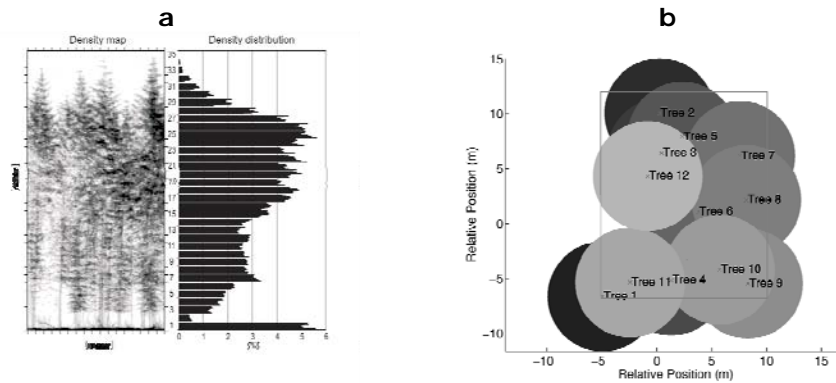


Figure 5-5: Results of the morphological reconstruction of the laser scan data.

Panel (a) shows the vertical density profile of the laser scan data; panel (b) shows the DART scenario 'Multiple Crowns' with a crown cover of 0.93 from a top down perspective.

In the simulation the branches were not taken into account. The crown diameter was obtained by inspection of the nadir viewing point cloud density. A crown diameter of 7.5m was observed. In order to simulate different clumping within the canopy, the crown diameter was changed to 7.5m, 6.5m, 5.5m and 4.5m. This resulted in four scenarios with different crown coverage (C_v) of 0.93, 0.87, 0.73 and 0.58, respectively, and different shape factors (ξ) of 0.28, 0.24, 0.20 and 0.16, respectively, as shown in Table 5-1.

5.3.2 SCOPE and SLC comparison

The original SCOPE implementation (van der Tol *et al.*, 2009c) caused problems at low sun and observation (elevation) angles. The errors were caused because this version of the SCOPE model did not contain a correction term for the thickness of the layers, and also did not include the shadow-length correction term by (Bréon *et al.*, 2002) for the hot spot effect in the bidirectional gap fraction. This was solved in the new version of the SCOPE model and the corrections are shown in equations (5-2) and (5-3). The effect of this correction is shown in Figure 5-6.

$$P_{s,o} = \exp(k_{s,o}LAIx) \frac{1 - \exp(-k_{s,o}LAI\Delta x)}{k_{s,o}LAI\Delta x} \quad (5-2)$$

$$P_{s0} = \frac{1}{\Delta x} \int_x^{x+\Delta x} \exp(k_s + k_o)LAIx + \frac{\sqrt{k_s k_o}LAI}{\alpha} (1 - \exp(\alpha x)) dx \quad (5-3)$$

where P_s , P_o and P_{s0} are the gap fractions for solar, observer, and bidirectional viewing, respectively; x is the height in the canopy; Δx is the finite thickness of the layers; k_s and k_o are the extinction coefficients for solar and observer angles, respectively; LAI is the leaf area index; and $\alpha = 2d_{so}/(q(k_s + k_o))$, with d_{so} denoting the hotspot correlation length and q the hotspot parameter.

The BRDFs estimated with the original SCOPE model showed large differences with the SLC model, with rMSDs around 14% for the near hotspot angles, and errors higher than 1% for the other angles (Figure 5-6). The modifications to the SCOPE model were a great improvement, with rMSDs of below 1% for all angles (Figure 5-6). Figure 5-6 depicts the errors at a wavelength of 750nm. Calculations at other wavelengths were also made and showed similar errors for

the original SCOPE model and similar improvements for the modified SCOPE model.

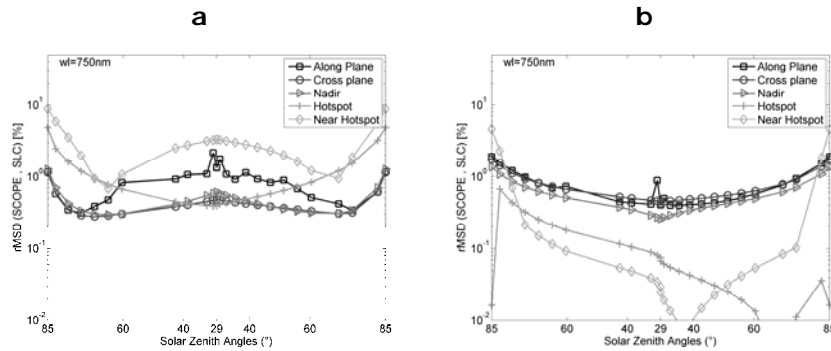


Figure 5-6: Relative BRDF difference between SCOPE and SLC. Panel A shows the difference between SCOPE and SLC before the modifications; Panel B shows the difference between SCOPE and SLC using the modifications to SCOPE for the finite size of the layers.

5.3.3 BRDFs of SCOPE, SLC and DART

Figure 5-7 shows the bidirectional reflectance of SCOPE, SLC and DART for a solar zenith angle of 35.1° and a wavelength of 750nm. The different DART scenarios for increasing structural complexity are shown respectively from panels A to F. The 'Bare Soil' and 'Layered Crown' are not shown, because the 'Bare Soil' scenario does not have an angular dependence, and because the 'Layered Crown' provides the same BRDF as the 'Elevated Layered Crown'.

The differences between the DART and SCOPE/SLC BRDF calculations varied with the increasing structural complexity of the scenarios. The biggest difference between SCOPE and DART occurred for the 'Multiple Crowns' scenario that had a crown coverage of 58%. The BRDF of this DART scenario displayed a deeper bowl shape than the other BRDFs. A more detailed analysis on the comparison between DART and SCOPE/SLC is found in a next section.

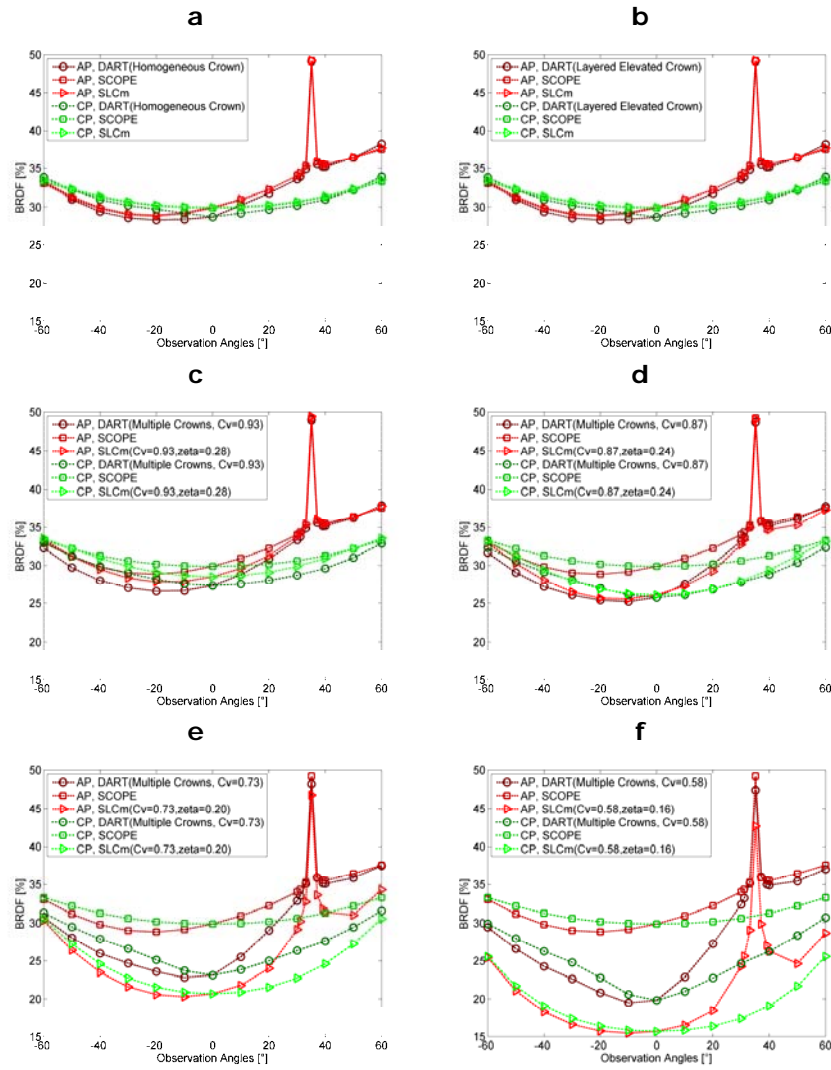


Figure 5-7: SCOPE, SLC and DART BRDFs for a 750nm wavelength.
Panels a-f depict the DART scenarios 'Bare soil' (a), 'Plot' (b), 'Homogeneous Crown' (c), 'Layered Crown' (d), 'Layered Elevated Crown' (e) and 'Multiple Crowns' (f).

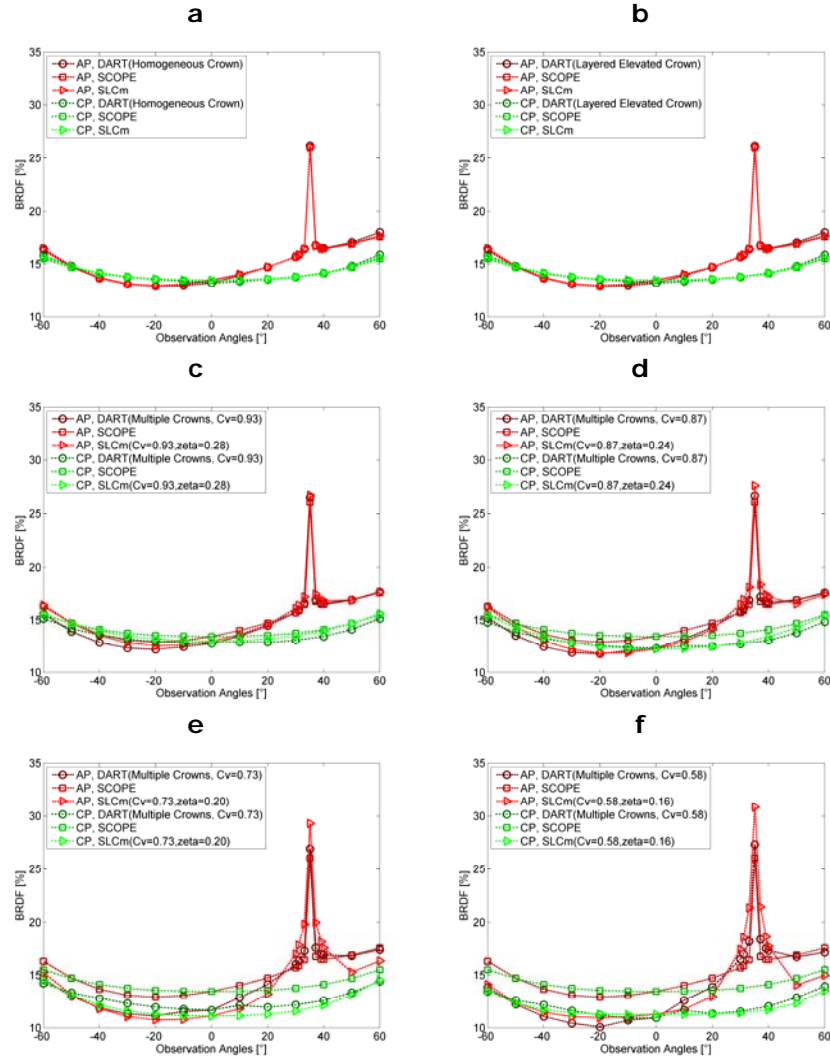


Figure 5-8: SCOPE, SLC and DART BRDFs for a 1750nm wavelength. Panels a-f depict the DART scenarios 'Bare soil' (a), 'Plot' (b), 'Homogeneous Crown' (c), 'Layered Crown' (d), 'Layered Elevated Crown' (e) and 'Multiple Crowns' (f).

5.3.4 DART scenarios, a comparison

In Figure 5-9 and Figure 5-10 the BRDF rMSDs of the different DART scenarios are shown for the wavelengths 750nm and 1750nm, respectively. The 'Plot' scenario was chosen as reference. The 'Bare Soil', and 'Layered Crown' scenarios are not shown.

In general the rMSD increased parallel to the complexity of the scenario. The differences at 750nm and 1750nm were of the same order, with differences slightly larger at 750nm than at 1750nm, which was attributed to the larger reflectance difference of the soil and leaves at 750nm than at 1750nm (Figure 5-4).

A clear variation in rMSD between the different observation angles was observed. Of all the angles' classes the 'hotspot observation' angles displayed the smallest difference between the relatively simple 'Plot' scenario and the complex scenarios. The nadir observation angle showed the largest difference between the 'Plot' and the complex scenarios. In the case of the 'Multiple Crowns' scenario the effect of clumping was more pronounced at nadir than at oblique viewing angles.

For the 'Homogeneous Crown' and the '(Elevated) Layered Crown' scenarios a larger than expected difference was found for the nadir observation angle. This was found to be caused by a small error within the DART program. DART cells at the edge of a scene had a larger LAI for tree cells. This caused a small clumping effect. As the spatial resolution of the 'simple' scenarios was lower than in the 'complex' scenario, the effect of this error was greater; at high resolutions the number of 'erroneous' cells decreased relatively. In the case of 'multiple crowns' the effect was negligible as the spatial resolution was high and single trees did not span the whole scenario. DART software engineers are currently trying to solve this problem. In this research the effect was only small compared to the whole shape of the BRDF (Figure 5-4).

In Table 5-3 the mean rMSDs for the different observation angles (Nadir, Along Principle Plane, Cross Principle Plane, Hotspot and near-Hotspot) are shown. The smallest rMSDs were found for the 'Homogeneous Crown' (0.91% and 0.88% at, respectively, 750nm and 1750nm) and increased parallel with increasing complexity (and decreasing crown cover).

The 'Multiple Crown' scenario with a crown cover of 0.58 produced the largest rMSDs (10.86% and 8.92%). The greatest contribution to this difference was caused by the nadir viewing angle (20.88 and

12.8) and the 'Cross principle Plane' observation angle (12.82 and 12.08). The difference in crown coverage at these viewing angles was most dominant.

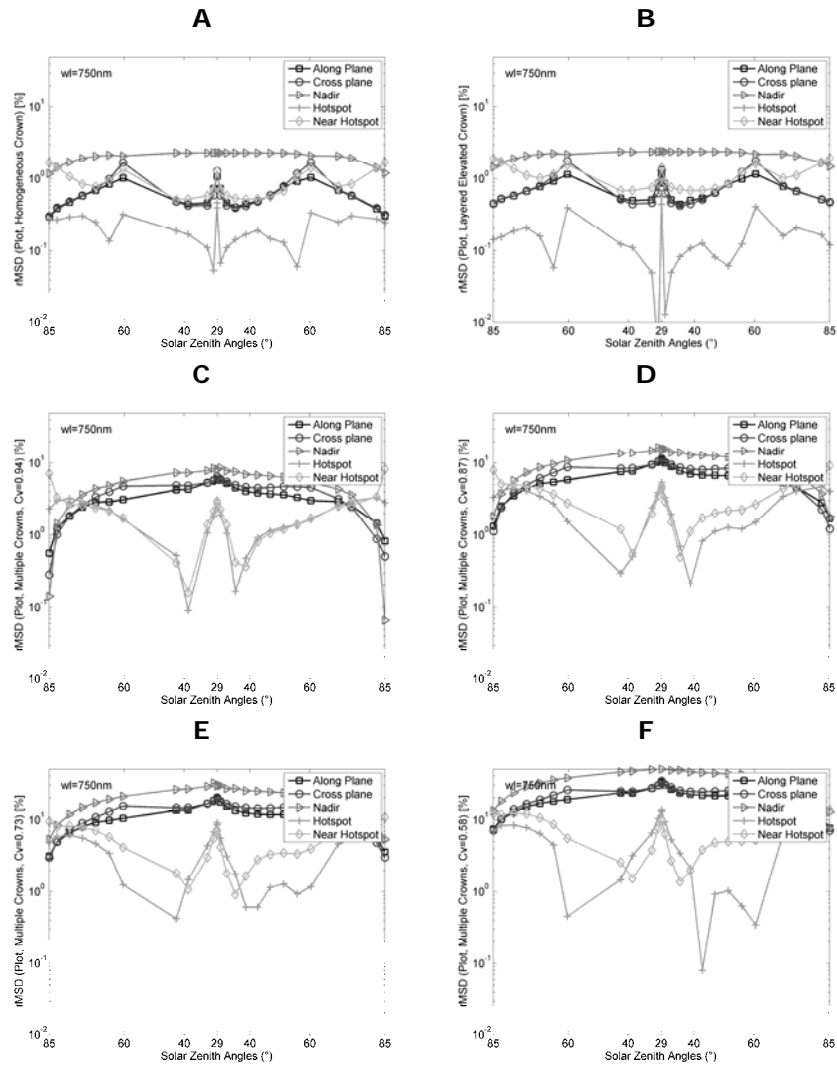


Figure 5-9: The rMSD between different DART scenarios at 750nm wavelength.
 Panels A-F depict the relative differences between the 'Plot' scenario and, respectively, the 'Homogeneous Crown' scenario (A), the 'Layered Elevated' scenario (B), and the 'Multiple Crowns' scenarios with crown coverage's of 0.93 (C), 0.87 (D), 0.73 (E), and 0.58 (F).

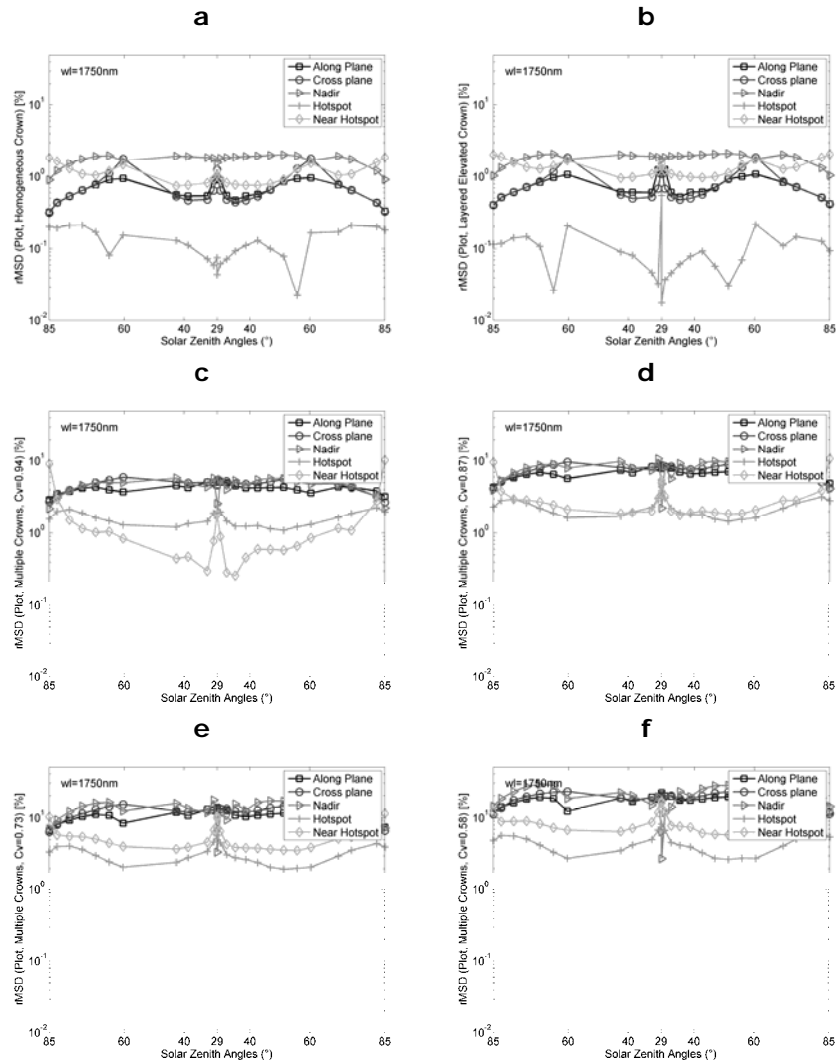


Figure 5-10: The rMSD between different DART scenarios at 1750nm wavelength.

Panels a-f depict the relative differences between the 'Plot' scenario and, respectively, the 'Homogeneous Crown' scenario (a), the 'Layered Elevated' scenario (b), and the 'Multiple Crowns' scenario with crown coverage's of 0.93 (c), 0.87 (d), 0.73 (e), and 0.58 (f).

Table 5-3: Mean relative differences (rMSD) between Dart scenarios.

The rMSD is calculated with the 'Plot' scenario as reference for other DART scenarios, i.e. 'Homogeneous Crown', 'Layered Crown', 'Layered Elevated Crown', and four different 'Multiple Crowns', with crown covers of 0.93, 0.87, 0.73, 0.58, respectively, for 'Multiple Crowns' 1,2,3 and 4.

Mean rMSD (%)	Angles					
	All	N	AP	CP	H	NH
@750nm						
Homogen. Crown	0.91	2.06	0.63	0.70	0.22	0.94
Layered Crown	0.91	2.06	0.63	0.70	0.22	0.94
Elev. Layer. Crown	1.00	2.19	0.72	0.77	0.17	1.15
Multiple Crowns 1	3.41	5.44	3.51	3.95	1.86	2.28
Multiple Crowns 2	3.41	5.44	3.51	3.95	1.86	2.28
Multiple Crowns 3	6.09	10.68	6.40	7.21	2.67	3.51
Multiple Crowns 4	10.86	20.88	11.46	12.82	3.9	5.25
@1750nm						
Homogen. Crown	0.88	1.72	0.68	0.76	0.13	1.13
Layered Crown	0.88	1.72	0.68	0.76	0.13	1.13
Elev. Layer. Crown	0.98	1.81	0.78	0.81	0.11	1.38
Multiple Crowns 1	3.34	4.43	4.22	4.77	1.60	1.68
Multiple Crowns 2	3.34	4.43	4.22	4.77	1.60	1.68
Multiple Crowns 3	5.50	7.55	6.76	7.62	2.33	3.26
Multiple Crowns 4	8.92	12.8	10.79	12.08	3.32	5.61

5.3.5 DART and SCOPE, a comparison

The rMSDs between SCOPE and the different DART scenarios are shown in Figure 5-11 and Figure 5-12 for wavelengths of, respectively, 750nm and 1750nm. The 'Bare Soil' scenario, 'Layered Crown' scenario, and the 'Multiple Crowns' scenarios with crown covers of less than 0.93, are not depicted. Table 5-4 lists the mean rMSDs for the different observation angles (Nadir, Along Principle Plane, Cross Principle Plane, Hotspot and near-Hotspot).

The difference in rMSDs between the SCOPE and DART scenarios increased parallel to the increase in structural complexity (and the decrease in crown coverage) for both wavelengths. The differences at 750nm and 1750nm were of the same order, with slightly larger differences at 750nm than at 1750nm.

A clear division was observed between the 'Multiple Crowns' scenarios and the more simple scenarios. Up to the 'Multiple Crowns' scenario

with $C_v = 0.93$, the total difference between SCOPE and DART was less than 7.5% (4.59% and 3.83% at, respectively, 750nm and 1750nm), with the near-hotspot viewing angle providing the largest contribution (11.64% and 13.14%). Although the value 0.031 provided the best result in the comparison, there was still an overestimation of the reflection near the hotspot. This needs to be investigated more closely in the future. At the point, where the crown coverage became less than one, the behaviour of the rMSD changed.

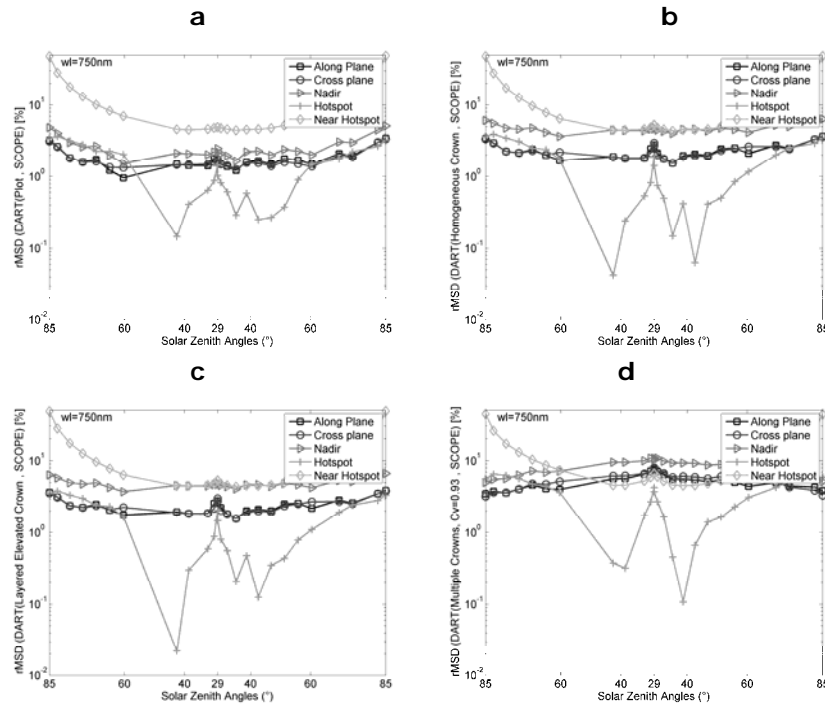


Figure 5-11: The rMSDs between SCOPE and DART scenarios for 750nm.

Panels a-d depict the relative BRDF difference at 750nm between SCOPE and the different DART scenarios ('Plot' (a), 'Homogeneous Crown' (b), 'Layered Elevated Crown' (c), and 'Multiple Crowns' (d)).

In the case of the 'Multiple Crowns' scenarios, the errors increased from values of 6.77% and 5.96% for a crown coverage of 0.93, up to 21.76% and 15.9% for a crown coverage of 0.58. At the same time both the Nadir (41.35% and 21.29%) and the Cross Principle Plane (23.97% and 18.81%) viewing angles started to dominate the rMSD, similarly to in the DART-DART comparison in the previous section.

Clearly the assumption of a homogeneous canopy did not hold any longer for a crown cover below 0.87.

The change in rMSD between the 'Elevated Layered Crown' and the 'Multiple Crowns' with a crown cover of 0.93, was very small. This increased difference was negligible to other uncertainties within the SCOPE model. It could therefore be argued that for small clumping, the SCOPE model might still be used, provided that the researcher acknowledged this shortcoming. Above the threshold of 0.93 the clumping effect became too dominant to neglect.

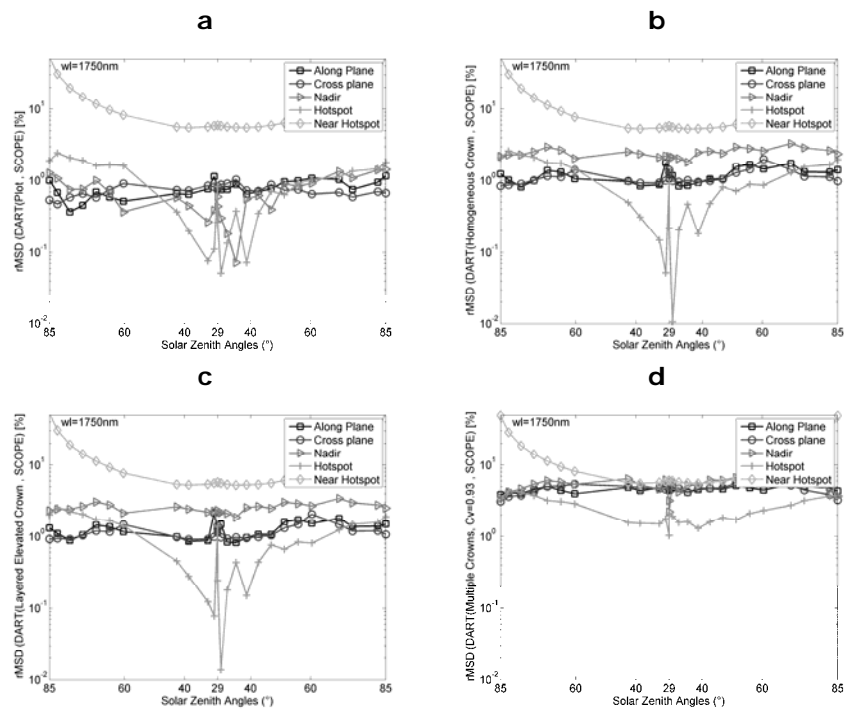


Figure 5-12: The rMSDs between SCOPE and DART scenarios for 1750nm.

Panels a-d depict the relative BRDF difference at 1750nm between SCOPE and the different DART scenarios: 'Plot' (a), 'Homogeneous Crown' (b), 'Layered Elevated Crown' (c), 'Multiple Crowns' (d).

Table 5-4: The rMSDs between SCOPE and Dart simulations. The rMSD is calculated with the DART Scenario as reference. The crown covers of 'Multiple Crowns' 1,2,3 and 4 are 0.93, 0.87, 0.73, 0.58, respectively.

Mean rMSD (%) @750nm	Angles					
	All	N	AP	CP	H	NH
Bare Soil	0.00	0.00	0.01	0.01	0.00	0.00
Plot	3.92	2.64	1.81	1.78	1.53	11.84
Homogen. Crown	4.54	4.75	2.34	2.35	1.60	11.65
Layered Crown	4.54	4.75	2.34	2.35	1.60	11.65
Elev. Layer. Crown	4.59	4.88	2.44	2.43	1.57	11.64
Multiple Crowns 1	6.77	8.20	5.21	5.51	3.29	11.63
Multiple Crowns 2	9.35	13.56	8.16	8.83	4.12	12.10
Multiple Crowns 3	14.03	24.00	13.31	14.54	5.37	12.93
Multiple Crowns 4	21.76	41.35	22.30	23.97	7.09	14.09
@1750nm						
Bare Soil	0.00	0.00	0.01	0.01	0.00	0.00
Plot	3.33	0.72	0.79	0.74	0.97	13.43
Homogen. Crown	3.80	2.44	1.19	1.13	1.05	13.18
Layered Crown	3.80	2.44	1.19	1.13	1.05	13.18
Elev. Layer. Crown	3.83	2.54	1.27	1.15	1.03	13.14
Multiple Crowns 1	5.96	5.18	4.61	4.68	2.46	12.85
Multiple Crowns 2	7.90	8.32	7.15	7.55	3.18	13.29
Multiple Crowns 3	11.05	13.61	11.19	12.01	4.16	14.27
Multiple Crowns 4	15.90	21.29	17.85	18.81	5.54	16.02

5.3.6 DART and SLC, a comparison

The advantage of the SLC model over the current unified SAIL implementation in SCOPE is that it can take the clumping of the vegetation into account. However this model is still a 1D model and therefore cannot take the azimuthal behaviour into account that may occur for relatively small simulated 3D scenes, as SLC would estimate an average for many of these small scenes. In order to find a threshold value the DART 'Multiple Crowns' scenarios were compared against the corresponding SLC simulations. In Figure 5-13 and Figure 5-14 the differences between the 'Multiple Crowns' scenarios by DART and the SLC simulations with clumping are shown. Figure 5-13 shows the rMSD between SLC and DART at 750nm and Figure 5-14 shows the rMSD at 1750nm.

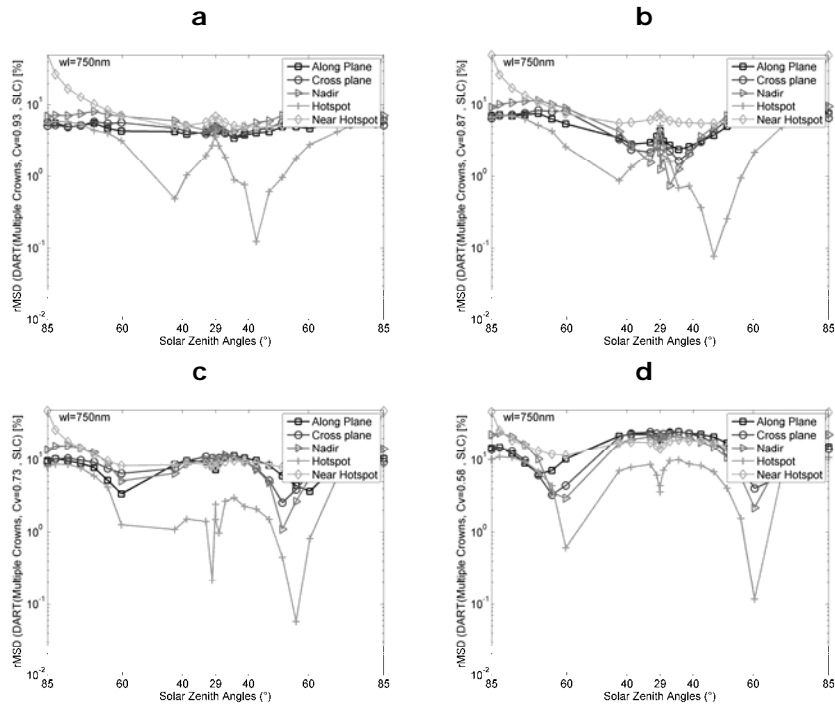


Figure 5-13: The rMSDs for SLC and DART scenarios at 750nm. Panels a-d depict the relative BRDF differences at 750nm between SLC and the different DART Multiple Crowns scenarios with : Cv=0.93 (a), Cv=0.87 (b), 'Cv=0.73 (c), Cv=0.58 (d).

In Table 5-5 the mean rMSDs for the different observation angles (Nadir, Along principle Plane, Cross principle Plane, Hotspot and near-Hotspot) are shown. In this section no attention will be paid to the 'simple' scenarios (as these were discussed in the previous section).

For the 'Multiple Crowns' scenarios with intermediate crown coverage it was observed that the errors were lower using the SLC clumping characterization than using the non-clumped SCOPE simulations. The rMSDs for the 'Multiple Crowns' scenarios with crown coverage's of 0.93 (6.33% and 5.99%) and 0.87 (6.66% and 7.12%) were smaller than 7.5%. Here the rMSD was dominated by the Near Hotspot viewing angles.

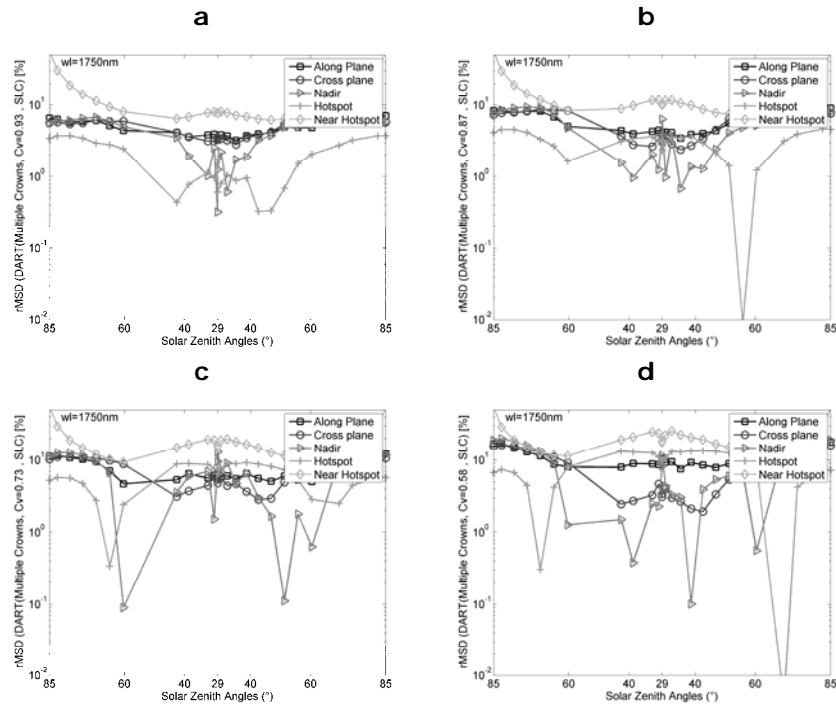


Figure 5-14: The rMSDs for SLC and DART scenarios at 1750nm.
Panels a-d depict the relative BRDF difference at 1750nm between SLC and the different DART Multiple Crowns scenarios with : Cv=0.93 (a), Cv=0.87 (b), 'Cv=0.73 (c), Cv=0.58 (d).

For a crown coverage smaller than 0.73, the rMSD increased above the 7.5% threshold. It was observed that the rMSDs at Nadir, Along principle Plane and Cross principle Plane increased but were still smaller than for the SCOPE simulations. The rMSDs at the Near-Hotspot, and Hotspot viewing angles in these scenarios became larger than the rMSDs acquired by the SCOPE simulations. As can be seen in Figure 5-7 and Figure 5-8, this was caused by SLC overestimating the clumping effect. At low crown coverage the vegetation (according to DART) started to behave like a row canopy, with a clear azimuthal dependence. SLC does not suffer from such artefacts. For crown coverage's above 0.73, the azimuthal dependence of the vegetation was still only minor and consequently the SLC model could be used in these scenarios.

Table 5-5: The rMSD between SLC and Dart simulations. The rMSD is calculated with the DART Scenario as reference. The crown covers of 'Multiple Crowns' 1,2,3 and 4 are 0.93, 0.87, 0.73, 0.58, respectively.

Mean rMSD (%) @750nm	Angles					
	All	N	AP	CP	H	NH
Bare Soil	0.00	0.00	0.01	0.01	0.00	0.00
Plot	4.37	3.22	2.29	2.29	1.48	12.48
Homogen.Crown	5.01	5.35	2.90	2.90	1.54	12.30
Layered Crown	5.01	5.35	2.90	2.90	1.54	12.30
Elev. Layer. Crown	5.06	5.48	2.99	2.99	1.52	12.30
Multiple Crowns 1	6.33	6.30	5.00	5.00	3.16	12.36
Multiple Crowns 2	6.66	6.53	5.38	5.38	3.52	12.68
Multiple Crowns 3	9.07	10.14	8.78	8.78	3.75	14.16
Multiple Crowns 4	15.01	16.63	15.73	15.73	7.14	18.93
@1750nm						
Bare Soil	0.00	0.00	0.01	0.01	0.00	0.00
Plot	3.81	1.48	1.09	1.09	0.88	14.15
Homogen.Crown	4.36	3.22	1.74	1.74	0.97	13.91
Layered Crown	4.36	3.22	1.74	1.74	0.97	13.91
Elev. Layer. Crown	4.39	3.32	1.80	1.80	0.95	13.87
Multiple Crowns 1	5.99	4.12	4.75	4.75	1.94	14.26
Multiple Crowns 2	7.12	5.11	5.76	5.76	3.14	15.64
Multiple Crowns 3	9.44	7.20	7.20	7.20	6.15	19.04
Multiple Crowns 4	11.67	8.75	8.15	8.15	9.03	21.42

5.4 Conclusion

In this chapter the SCOPE and SLC model were successfully compared with the DART radiative transfer model. The SLC radiative transfer model was included to compare the discrete SAIL model incorporated in the SCOPE model with the analytical solution of the SLC model, and to investigate the model's implementation of clumping.

The comparison between the SLC and the SCOPE model showed large differences between the two models. In the original SCOPE model no modification was incorporated to correct for the discrete nature of the layers. A solution has been presented in this chapter taking the finite size of the layers into account. The error after implementation dropped below 1% for all but the extreme oblique (85°) viewing angles.

In total nine scenarios, with varying degrees of structural complexity, were simulated by the DART model. The parameters needed for the creation of these scenarios were obtained by Terrestrial Laser scanning over the Speulderbos. Using 3D filter operations the position of the trees, and the horizontal and vertical crown shapes, were established. The x-y coordinates of 12 trees, their crown diameter, and a vertical distribution of the LAI were retrieved.

The comparison between the DART and SCOPE models showed a good match for the simple scenarios. The comparison produced rMSDs below 7.5% for crown coverage values higher than 0.93. The largest contributors to this rMSD were the Near-Hotspot viewing angles. Although the hotspot effects in DART and SCOPE are based on the same principle (Kuusk, 1991), the rMSD at near-hotspot viewing angles (~12% and ~14% at, respectively, 750nm and 1750nm) was consistently high, while within the hotspot the values were lower (~3% and ~2%). This was attributed to discretization within the DART model. As the discrete and analytical SAIL models showed the same behaviour this will need to be investigated further. In the 'Multiple Crowns' scenarios with a crown coverage below 0.93 the errors were too large to merit the use of the discrete SAIL version.

For the 'Multiple Crowns' scenarios with a crown cover of below 0.93 the DART scenarios were compared with the SLC model. The SLC model showed good agreement for medium crown coverage values (0.93 and 0.87) with figures of respectively 6.33% and 5.99% at 750nm and 6.66% and 7.12% at 1750nm for these two scenarios. In this DART - SLC comparison the main discrepancy was the rMSD at Near-Hotspot viewing angles (12.36% and 14.26%; 12.68% and 15.64%), which was also found in the DART - SCOPE comparison. The errors at the other viewing angles (Nadir, Along principle Plane, Cross principle Plane, and Hotspot) were smaller than in the DART-SCOPE comparison.

At very low crown coverage the comparison between SLC and DART produced too large errors (>9.07% and >9.44%). This was attributed to the azimuthal dependence of the BRDF at such low crown coverage. The effect was an artefact in the form of a kind of row-structuring of the canopy in the DART implementation.

The addition of clumping of the canopy in the SLC model increases the applicability of the model for a wider range of canopies. Incorporating this approach into the SCOPE model is however difficult due to the discrete nature of the SCOPE method. Also at present no

Validation of radiative transfer

thermal version of the SLC model exists. It would be useful to investigate this in the future.

6 Retrieval of skin temperatures from directional observations

Based on

Timmermans, J., Verhoef, W., van der Tol, C. and Su, Z. (2009) Retrieval of canopy component temperatures through Bayesian inversion of directional thermal measurements. In: Hydrology and earth system sciences (HESS), 13 (2009)7, pp. 1249-1260.

Abstract

In this chapter an inversion method is presented for the estimation of skin temperatures of four land surface components. The method inverts the SCOPE model using directional brightness temperatures. In addition a priori (Bayesian) information is used to solve the ill-posed inversion problem.

The method was first tested in a sensitivity analysis, using a large simulated dataset. The dataset contained 3840 scenarios, consisting of 8 skin temperature profiles, 10 solar zenith angles, 8 sensors, and 6 noise profiles. A parameter was defined for the investigation of the success rate. The results of the sensitivity analysis show that the Bayesian approach is able to retrieve skin temperatures of the four components from directional brightness temperatures with good success rates using multi-directional sensors, while no improvement was found when mono-angular sensors were used.

After successful completion of the sensitivity analysis the algorithm was used to estimate the skin temperatures of different crops. For this the datasets of the EAGLE and AGRISAR field campaigns were used. The results of the experimental study show that the approach provides good results for high LAI values ($RMSE_{grass} = 0.50 K$, $RMSE_{wheat} = 0.29 K$, $RMSE_{sugarbeet} = 0.75 K$, $RMSE_{barley} = 0.67 K$); but for low LAI values the results were unsatisfactory ($RMSE_{youngmaize} = 2.85 K$). This discrepancy was found to originate from the metallic construction of the setup. Using masked thermal images will eliminate this discrepancy.

6.1 Introduction

Accurate estimation of skin temperatures of different canopy components is of great importance in the characterisation of biophysical processes. Biophysical processes such as evapotranspiration and photosynthesis are highly sensitive to variations in temperature. Evapotranspiration in remote sensing is usually calculated by applying energy balance models (Glenn *et al.*, 2007; Gowda *et al.*, 2007; Kalma *et al.*, 2008) such as SEBAL (Bastiaanssen *et al.*, 1998), and SEBS (Su, 2002).

In most remote sensing energy balance studies only one single calculation of surface temperature is used (Su, 2002; Jia *et al.*, 2003b), based on the brightness temperature at Nadir viewing and the effective emissivity, which is estimated a priori or calculated using techniques such as temperature emissivity separation (Gillespie *et al.*, 1998; Payan and Royer, 2004). For heterogeneous canopies, the assumption of a single surface temperature does not suffice (Kustas and Norman, 2000; Jia *et al.*, 2001; Yan *et al.*, 2001; Jia *et al.*, 2003a). The temperatures of the individual canopy components differ significantly, as was shown in chapter 3, and consequently applying a single land surface temperature for the estimation of biophysical processes leads to high uncertainties. Therefore a method to retrieve the skin temperatures should be investigated.

Retrieval of multiple independent skin temperatures is most easily achieved using multi-directional observations. Such retrieval is possible due to the angular behaviour of brightness temperature, as shown in chapter 3. The advantage of using multiple images is that the number of independent observations increases and consequently the ill-posed inversion problem is reduced (Combal *et al.*, 2002; Verhoef, 2007).

Most of the parameter retrieval studies (Jacquemoud *et al.*, 2000) deal with only the optical part of the spectrum (Knyazikhin *et al.*, 1998a; D'Urso *et al.*, 2004; Meroni *et al.*, 2004; Tang *et al.*, 2007). Only a few studies have investigated the retrieval of skin temperatures of different land surface components (Yan *et al.*, 2001; Jia *et al.*, 2003a; Timmermans *et al.*, 2008) and the application of these temperatures for the estimation of biophysical processes (Norman *et al.*, 1995; Anderson *et al.*, 2008). In these approaches only the skin temperatures of two components, i.e. soil and leaves, were retrieved. However the variation in temperature between sunlit and shaded, soil and leaves is large, as was shown in chapter 3, and

these differences should not be ignored in the retrieval. Chapter 4 illustrated that skin temperature of the components varied depending on height and leaf-transpiration rate. The SCOPE model created the possibility to estimate skin temperatures for a large number of components, by integrating all the biophysical and biochemical processes.

The objective of this chapter is to create an inversion scheme to retrieve skin temperatures of different land surface components. The research was limited to four (sunlit soil, shaded soil, sunlit leaves and shaded leaves) components (chapter 3), in order to reduce computation time. The inversion scheme was tested on the forward simulated brightness temperatures. A sensitivity analysis was performed with various satellite configurations, from single view and single band to multiple view and multiple bands. Finally a case study was performed using data from the EAGLE and AGRISAR field campaigns.

6.2 Methodology

Retrieval algorithms can be divided into three major classes (Kimes *et al.*, 2000): neural networks, look-up tables and optimization schemes. The accuracy of neural networks and look-up tables depends on the number of pre-computed "training" values and on the interpolation between these "trained" values (Picton, 2000). This interpolation cannot be performed over singularities such as the hot spot, despite recent advances (Gastellu-Etchegorry *et al.*, 2003). Optimization methods do not have this limitation, and are only limited by the shortcomings of the radiative transfer model. Optimization methods are inherently suitable to handle arbitrary viewing and observing angles. Therefore the optimization method is still the most used inversion technique in directional remote sensing (Meroni *et al.*, 2004; Rautiainen, 2005; Nikolov and Zeller, 2006).

Recently an optimization method was proposed (Verhoef, 2007) that incorporates both directional observations and a priori (Bayesian) information. The addition of these two extra data sources reduces the inversion problem significantly. Therefore this method is used in this research. A more detailed description of the algorithm is provided in paragraph 6.2.1.

The inversion method was tested over simulated and measured scenarios:

1. A sensitivity analysis was performed using simulated scenarios. In time-limited field campaigns the chance of encountering all the scenarios needed for a thorough sensitivity analysis is very small. In order to explore the performance of the algorithm under different conditions, forward simulated brightness temperatures were used. The advantage of forward simulations is that one can also simulate future satellites like SPECTRA (Sobrino and Jimenez-Munoz, 2005; Verhoef and Bach, 2007). Consequently this methodology enabled both the testing of the retrieval algorithm and investigation into the full potential of multi directional observations instead of Nadir only remote sensing. This is explained in section 6.2.2.
2. Next, the algorithm was run using the multi-directional radiative observations acquired in the EAGLE and AGRISAR field campaigns. Skin temperatures measured during the EAGLE campaign were used for validation. The measurements are described in detail in chapter 2.

Note that research was limited to four components (sunlit soil, shaded soil, sunlit leaves and shaded leaves), as identified in chapter 3. Retrieval of the full vertical profile of sunlit/shaded leaf temperatures would require the incorporation of the energy balance iteration. This would lead to a very high computation time. For the research objective this was not necessary, and consequently not performed.

6.2.1 Traditional retrieval algorithms

The most simple optimization is based on the Gauss-Newton method (Tarantola, 2005). The update rule in this iteration is shown in equation (6-1).

$$\Delta p = (J^T J)^{-1} J^T \Delta r \quad (6-1)$$

where Δp denotes the changes in the parameters for retrieving the correct parameter set, Δr denotes the difference between the observed variables and simulated variables, and J denotes the local sensitivity of the model.

Newtonian methods are relatively easy to implement and converge fast. To further improve upon this convergence the Newton method was modified independently by Levenberg and Marquardt (Fox, 1997). The Levenberg-Marquardt (LM) algorithm (shown in equation

(6-2)), is a modification of the Gauss-Newton algorithm (Moré and Wright, 1993).

$$\Delta p = (J^T J + \mu I)^{-1} J^T \Delta r \quad (6-2)$$

where μ is a scalar that controls the numerical stability of the algorithm (Verhoef, 2000). This (non-negative) scalar is updated per iteration. When μ is small the LM method approaches the quadratic Newton convergence; when μ is large the LM method approaches the steepest descent method. This LM method is still used in current research (North, 2002). Both methods, however, may still lead to instability as can be shown when using singular value decomposition.

If the input parameters of the model are linearly dependent on each other, the input-output relationship will be non-unique. This results in an ill-posed inversion scheme, making it impossible to retrieve unique sets of parameters. Single Value Decomposition (SVD) will not only diagnose this problem but will give a useful numerical answer (Press *et al.*, 2007). The SVD method states that a Jacobian matrix J can be decomposed by equation (6-3).

$$J = USV^T \quad (6-3)$$

where U is column-orthogonal ($U^T U = I$), S diagonal and V orthogonal ($V^T V = V V^T = I$). This results in the relation $(J^T J) J^T = V S^{-1} U^T$, which illustrates why the Gauss-Newton method may be suffering from difficulties, since the matrix of singular values S may contain zeros. This happens when there is linear dependence, and in that case the matrix inversion is impossible. For small singular values the corresponding change of model input parameters becomes very large, which leads to numerical instability.

The ill-posed problem of the model inversion can be further reduced if a priori data are used (Kimes *et al.*, 2000; Verhoef, 2007; van der Tol *et al.*, 2009a). The addition of a priori information transforms the original Newtonian update rule of equation (6-1) into equation (6-4).

$$\Delta p = V(S^2 + I)^{-1} [S U^T \Delta r + V^T \Delta p_a] \quad (6-4)$$

where Δp_a denotes the difference between the current parameter set (p_m) and the a priori values (p_a), and Δr denotes the difference

between the measurements (r) and modelled observations (r_m). The variables are normalized by the respective standard deviations of the parameters, assuming a Gaussian distribution. The variable Δr is normalized using the sensor noise.

The final solution of the inversion is then given by equation (6-5). It can be seen that when the sensitivity of the model is high the model solution will dominate the solution and when it is low, the a priori solution will dominate.

$$p_s = V(S^2 + I)^{-1} [S^2 V^T p_m + V^T p_a] \quad (6-5)$$

The algorithm has been programmed as a Matlab script. The data flow of this program is presented in Figure 6-1.

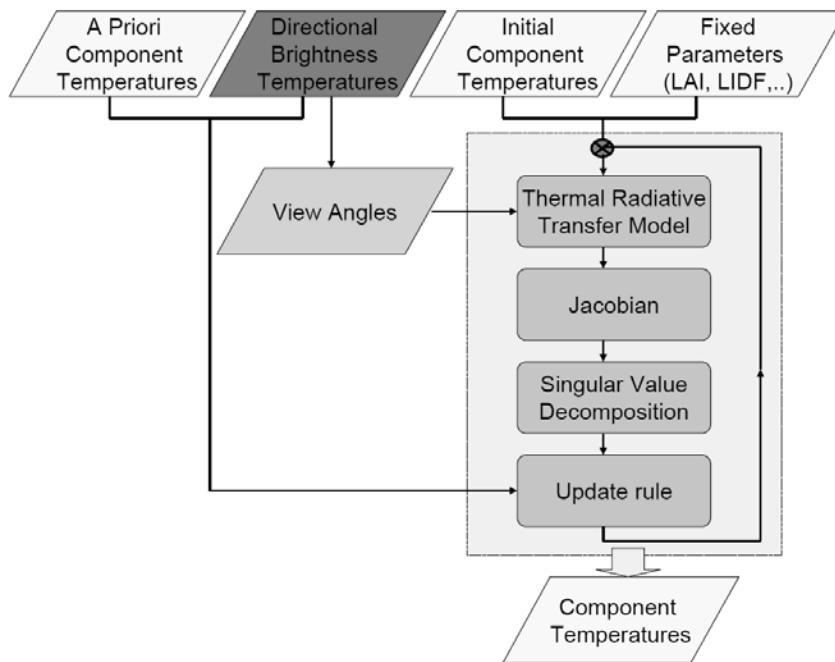


Figure 6-1: Bayesian Inversion Scheme

The a priori information is extracted from the shape of the directional thermal brightness temperature. The path length through the canopy depends on the viewing angle; for oblique viewing angles θ_o , the optical path length will be large and the measured brightness

temperature will depend mainly on the vegetation itself: $T_v = T_b(\theta_o = \max(\theta_o))$; and for nadir looking angles, the optical path length is at a minimum and the measured brightness temperature will depend more on the soil: $T_v = T_b(\max(\theta_o))$.

The standard deviation used to normalize this a priori information was calculated using the upper and lower limit for vegetation and soil, assuming a Gaussian distribution. The lower and upper limits for soil were set to -5°C and 100°C , and for vegetation to 0°C and 42°C .

As shown by Verhoef (Verhoef, 2007) using the Bayesian update rule of equation (6-5) not only solves the ill-posedness of the inversion problem, but also takes into account the sensitivity of the model and uncertainties in input/output parameters. The sensitivity of the radiative transfer model to the input parameters is captured by the diagonal matrix S . The uncertainty of the model and measurements is captured by the normalization of Δr and Δp_a . For example, if the sensitivity is low, the values in S will become nearly singular. In that case the update rule will be largely dependent on the a priori values.

6.2.2 Sensitivity analysis

Simulations of the directional brightness temperatures were performed for different sensors and for different temperature profiles. The total number of simulations came to 3840. These scenarios consisted of 8 skin temperature profiles, 10 solar zenith angles, 8 sensors, and 6 noise profiles. Note that in reality the skin temperature profiles were the result of the surface energy balance and consequently the solar zenith angles. However in this case the temperatures were set independently for the sensitivity analysis.

Retrieval of skin temperatures

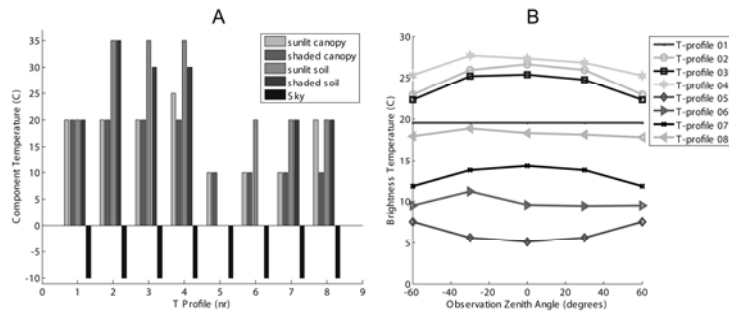


Figure 6-2: Skin and Brightness temperature profiles of different scenarios.
Panel A depicts the temperature profiles. Panel B depicts the corresponding directional brightness temperatures.

Table 6-1: Input parameters for the Sensitivity analysis of the Inversion algorithm.

	Symbol	Value	Unit
Leaf spectra			
Chlorophyll a and b content	C_{ab}	60.000	$\mu\text{g}/\text{cm}^2$
Water Content	C_w	0.009	cm
Dry matter	C_{dm}	0.012	g/cm^2
Senescent material	C_s	0.000	-
Mesophyll structure	N	1.400	-
Leaf emissivity	ε_c	0.99	-
Soil spectra			
Soil reflectivity	ρ_s	DART database	-
Soil emissivity	ε_s	0.95	-
Canopy Parameter			
Leaf Area Index	LAI	1.50	m^2/m^2
Hotspot parameter	q	0.05	m
Leaf Inclination distr.	$LIDF$	Spherical	-
Soil emissivity	ε_s	0.95	-
Sun zenith angle	θ_s	[0-60]	$^\circ$
Observer zenith angle	θ_o	sensor dependant	$^\circ$
Relative azimuth angle	φ	sensor dependant	$^\circ$

The soil reflectance was not measured/modelled but a standard spectrum (gravelly soil) was taken from the DART spectral database (Gastellu-Etchegorry *et al.*, 2004) and a Lambertian reflectance was assumed. The thermal emittance of soil and leaves were calculated using Planck's law for sunlit and shaded contact temperatures.

Note that the current method assumes that the skin temperatures are homogeneous per component. However the temperature of individual sunlit leaves varied about 5 to 10 K around the average temperature. This variation in temperature depends on the biophysical processes in the leaf and the orientations of individual leaves with respect to the sun. As the inversion method would only be used in the radiative transfer part, these biophysical processes did not need to be taken into account, and the "mean" skin temperatures of the four components sufficed.

6.2.2.1 Sensor simulator

The outgoing hyperspectral radiances were converted to sensor band observations, using a newly created sensor simulator. In this simulator sensor characteristics, such as band sensitivity (Figure 6-3), were used to calculate the recorded radiances by the sensor. Ultimately these observations were converted into band reflectances, and band brightness temperatures.

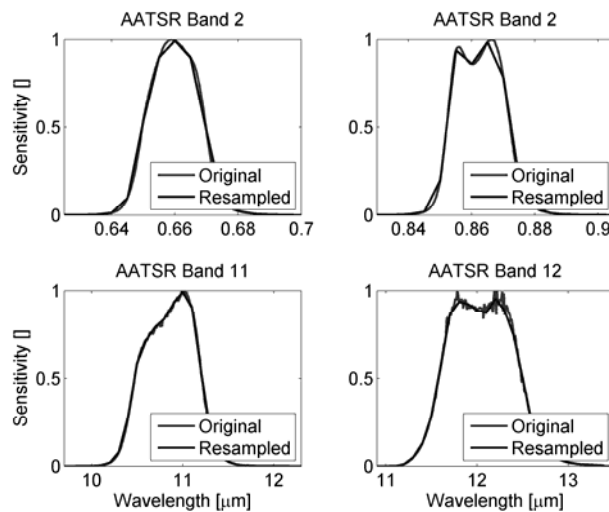


Figure 6-3: AATSR sensor sensitivities as modeled by the sensor simulator.

Different satellite sensors were simulated for the same scenarios with different noise levels. These simulated observations could then be used to investigate the potential of the retrieval algorithm of using multiple viewing angles instead of a single view (nadir) sensors.

The sensors that were simulated are listed in Table 6-2. These instruments ranged from broadband ground instruments, such as the Irisys 1011 (Su *et al.*, 2005b), to multispectral solo-directional satellite sensors, such as ASTER (Yamaguchi (Yamaguchi *et al.*, 1998) and multispectral multidirectional satellite sensors, such as AATSR (Prata *et al.*, 1990).

Table 6-2: Overview of simulated sensors for inversion of the SCOPE model.**Sensor characteristics of thermal bands.**

Sensor	Bands [-]	Range ⁵ [μm]	Accuracy [K]	Obs. Angles
Irisys 1011	1	08.0 – 14.0	0.5	1 (nadir)
Landsat 7	1	10.4 – 12.5	0.6	1 (nadir)
AATSR	2	10.4 – 12.5	0.1	1 (nadir)
ASTER	5	08.1 – 11.7	1.0	1 (nadir)
MODIS	5	08.4 – 14.4	0.5	1 (nadir)
AATSR	2	10.4 – 12.5	0.1	2
SPECTRA	2	10.3 – 12.8	1.0	7
Irisys 1011 (Goniometer)	8	08.0 – 14.0	0.5	9 ⁶

6.2.2.2 Noise levels

The errors in the retrieved variables depend on: 1) the inversion method, 2) the number of independent observables, 3) the number of parameters to be retrieved, and 4) the sensitivity of the modelled remotely sensed data to surface properties.

In order to investigate the potential of the SCOPE inversion, a) the number of variables to be retrieved was increased and b) the noise levels in the observed radiances were changed. The number of variables to be retrieved was increased from 4 (skin temperature sunlit/shaded leaves/soil) to 5 (including air temperature), and to 6 variables (additionally including LAI).

The directional behaviour of the brightness temperatures may be lost if the noise level in the measurements is too high. Therefore the effect of different levels of noise on the retrieval algorithm should be investigated. Different levels of sensor noise were added to the directional brightness temperatures in order to investigate the success of the retrieval algorithm as shown in equations (6-6) and (6-7). In this research the model was assumed to be perfect (although in the previous chapter some shortcomings were identified), and consequently no model uncertainty was added.

⁵ The thermal bands shown here are those with a wavelength > 8 μm .

⁶ The Irisys 1011 radiometer is attached to the goniometric system (explained in chapter 11). However only 1 run was used for the inversion.

$$T_{bm}(i_{band}, i_{obs}) = T_{bt}(i_{band}, i_{obs}) + dT_{bn}(i_{band}, i_{obs}) \quad (6-6)$$

$$dT_{bn}(i_{band}, i_{obs}) = N_l A_s(i_{band}) \mathfrak{R}(i_{band}, i_{obs}) \quad (6-7)$$

The measured brightness temperature T_{bm} at band i_{band} and observation angle i_{obs} , was calculated as the sum of the “true” brightness temperature T_{bt} and the noise dT_{bn} . The noise was calculated as the product of a noise level N_l , the sensor accuracy A_s and a random value \mathfrak{R} . The random values were generated with a normal distribution ($\text{std}(\mathfrak{R})=1$ and $\text{mean}(\mathfrak{R})=0$).

Note that most research simulates sensor noise by using the specified noise equivalent temperature difference (NEdT) that is given in the sensor documentations. This study aimed to investigate the success rate of the algorithm for other than sensor noise as well. For this reason, the NEdT approach was considered too limited for this study.

6.2.2.3 Success rate

The success of the retrieval was evaluated in this sensitivity analysis using the ratio of $RMSE_m$ and $RMSE_i$, see equations (6-8), (6-9) and (6-10).

$$S_r = \frac{RMSE_m}{RMSE_i} \quad (6-8)$$

$$RMSE_m = \sqrt{\frac{1}{N} \sum_i^N (p_m(i) - p_t(i))^2} \quad (6-9)$$

$$RMSE_i = \sqrt{\frac{1}{N} \sum_i^N (p_a(i) - p_t(i))^2} \quad (6-10)$$

where S_r is the success rate, $RMSE_m$ is the root mean square error between the retrieved parameters p_m , and true parameters p_t ; $RMSE_i$ is the root mean square error between the a priori parameters p_a , and true parameters. Values for S_r lower than 1 denote that the inversion has improved compared to the a priori estimates of the

parameters; values for S_r higher than 1 denote that the inversion has deteriorated from the a priori estimates; values of 1 denote that the inversion has neither improved nor deteriorated from the a priori estimates.

Note that the success rate uses averages of the separate errors for the different parameters. As the algorithm is based on the Gauss-Newton method, it optimizes the overall error, resulting in larger errors for components that are less frequent (such as sunlit soil in the case of high LAI).

6.2.3 Field measurements

As shown in chapter 5 the SCOPE model can be used for all vegetation types except clumped vegetation. SCOPE was therefore able to characterize all the measured crops listed in chapter 2 with the exception of the vineyard. Inversion of these vegetation types is shown after the analysis of the sensitivity study. The inversion was performed using the Everest 3000 radiometer data.

6.3 Results

6.3.1 Sensitivity study

The success rate S_r is shown in Figure 6-4 for the different sensors, temperature profiles and noise levels. Using monodirectional sensors the values for the skin temperatures of the different components were not improved, with the exception of temperature profile 1. In all other scenarios, the success rate deteriorated with increasing noise level. An explanation can be found in the fact that the observations were too unique to run the algorithm. Improvement in the estimation depends on the number of unique measurements.

In most scenarios the values of the skin temperatures were improved using the retrieval algorithm with the multidirectional sensors. Although the success rate was reduced with increasing noise levels, the success rate only became unacceptable for certain scenarios with very high noise levels:

- The improvement of the retrieval ($S_r < 1.0$) was apparent for all profiles with $N_l < 1.0$. Even for very high noise levels ($N_l = 0.8$), the success rate was acceptable ($S_r < 1.0$).

- The success rate of multi directional sensors for profile 1 was not acceptable. For this scenario, the retrieval of the skin temperatures was actually worse than with monodirectional sensors. For profile 1 the directional brightness temperature was uniform over the viewing angles (Figure 6-2). The shape of the added noise dominated the shape of the directional brightness temperature. The retrieval algorithm tried to fit this shape, and consequently did not find the correct skin temperatures. In reality the skin temperatures will never be completely homogeneous.
- For the scenario with the highest noise level ($N_i = 1.0$) the success rate predominantly depended on the shape of the random values, \mathfrak{R} , which was unacceptable. Note that the added noise in this scenario was of the same order as the sensor sensitivity. This was an order of magnitude higher than usual sensor noise. The best average success rate for profiles 2-7 was achieved by multi-directional sensors: the Goniometric setup ($S_r = 0.3$), the SPECTRA sensor ($S_r = 0.3$), and the AATSR ($S_r = 0.5$). The retrieval with Goniometric setup had a slightly higher success rates than the SPECTRA sensor.

In addition to the retrieval of the four parameters, two other inversions were performed, retrieving five and six parameters each. The extra parameters to be retrieved were sky temperature and leaf area index (LAI). The overall success rate of these runs is shown in Figure 6-5.

The success rate of the inversion remained acceptable when increasing the number variables to be retrieved. Only a slight deterioration in success rate was observed when retrieving six parameters. The overall success rates for the retrieval of sky temperature were unacceptable ($S_r > 1.0$) with AATSR and MODIS. The overall success rates for the retrieval of LAI were promising ($S_r \leq 1.0$). As LAI is usually retrieved using optical measurements this algorithm may be used to enhance this value with the extra information of thermal measurements upon the a priori estimates found ($S_r \sim 1$). The inversion was only unacceptable for unrealistically high noise profiles. As success rates of 1 denote no deterioration compared to a priori estimates, the algorithm may be run as a post-processor on Level 3 satellite imagery without concern about deterioration of the product. The retrieval of skin temperatures

of four components was performed successfully ($S_r < 1.0$) for all multidirectional simulated observations.

Of all possible viewing angles, the along-track configuration proved to have the best potential. The SPECTRA and goniometric configuration had the same success rate. The additional cross solar plane angles did not contribute significantly. In the field a goniometric setup was preferred.

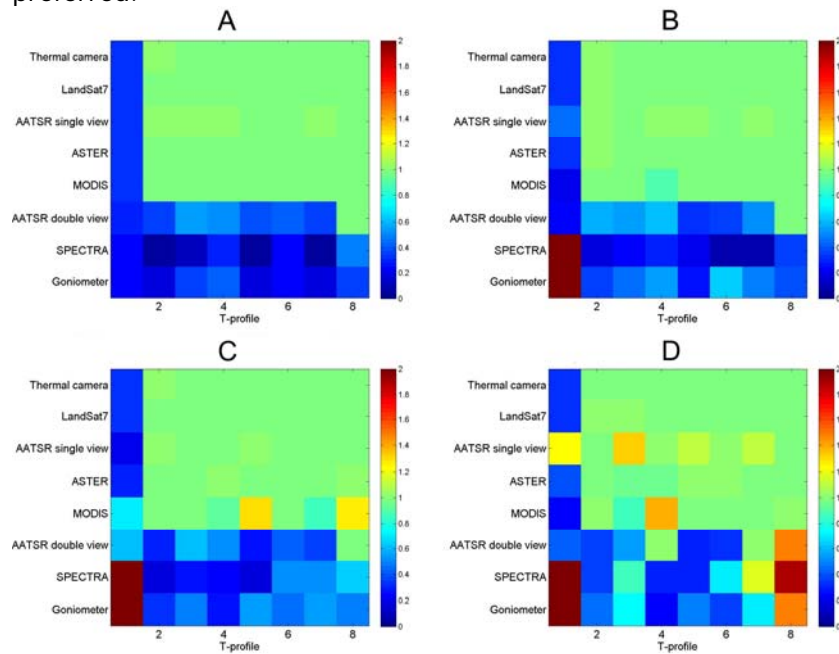


Figure 6-4: Success rate for different scenarios, satellites and noise levels.
The solar zenith angle for these simulations was 46.7 degrees.
The panels A-D show a noise level of 0.0, 0.4, 0.8 and 1.0, respectively.

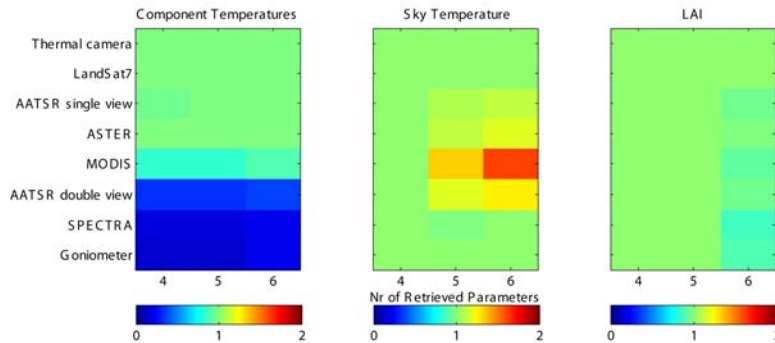


Figure 6-5: Success rate variability for different numbers of retrieved parameters.

In the case of 4 variables only skin temperatures (of four components) are retrieved, in the case of 5 variables, the skin temperatures and air temperature are retrieved, and for 6 variables, LAI is also included.

The potential of the Bayesian inversion applied to multidirectional imagery has been demonstrated. For monodirectional sensors no improvement was found. The retrieval of other variables (sky temperature and LAI) produced mixed results. Inversion of the model was not successful ($S_r > 1.0$) for sky temperature and moderately successful for LAI ($0.5 < S_r < 1.0$). The algorithm failed to retrieve this sky temperature, because sensitivity of directional radiation to this radiation is very low. The better retrieval of LAI was due to high sensitivity of directional radiation to LAI (as was also proven in the AGRISAR field measurements). Note that LAI is usually retrieved using optical measurements. Consequently the need for retrieval of this parameter through thermal measurements is low. However in the absence of optical measurements, for example at night time, this procedure could be useful.

6.3.2 Inversion of goniometric measurements

Three time series were made with the goniometer during the EAGLE 2006 field campaign. Of the three time series two were made over tall grass and one over maize (Figure 6-6 and Figure 6-7). The lines represent the mean measured brightness temperature. The error bars denote the RMSE between the measured and the retrieved directional brightness temperature. The RMSE for grass is about 0.5 K and for maize 2.5 K.

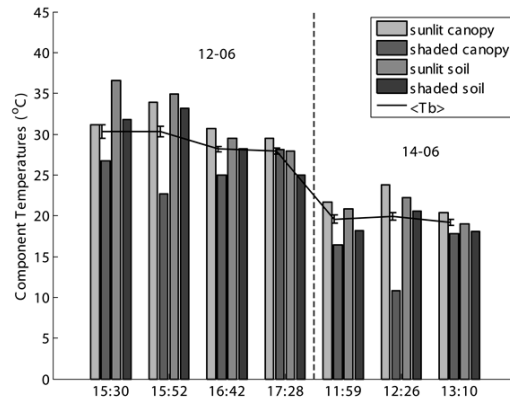


Figure 6-6: Retrieved skin temperatures of four components of grassland.

The lines represent the mean directional brightness temperature; the error bars represent the RMSE between the measured and modeled brightness temperatures. The measurements have been performed on 12 June 2006 and 14 June 2006 during the EAGLE campaign.

The measured brightness temperatures over grass were performed during two separate days, 12 June 2006 and 14 June 2006. The brightness temperatures were higher on the first day than on the second day: on the first day the measurements were performed in the afternoon with clear skies, while on the second day the measurements were performed early in the morning under overcast conditions.

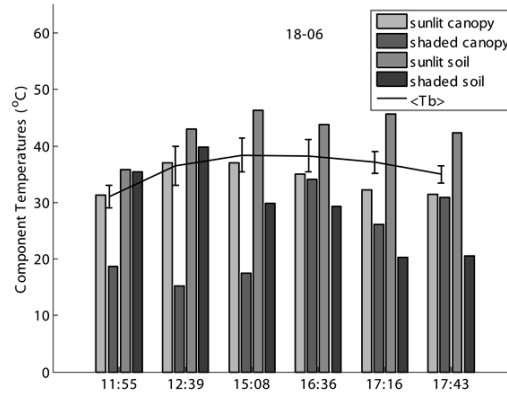


Figure 6-7: Retrieved skin temperatures of four components of young maize.

The lines represent the mean directional brightness temperature; the error bars represent the RMSE between the measured and modeled brightness temperatures. The measurements have been performed on 18 June 2006 during the EAGLE campaign

The grass leaf temperatures at 15h30 and 15h52 on the first day were lower than the soil temperatures. The soil temperature decreased during the day, while the leaf temperature remained relatively constant. This was caused by the sun directly illuminating the different components. As the sun reached lower angles, the soil was shaded by the canopy, whereas the leaves high in the canopy still received sunlight.

The maize leaf temperature was always lower than the temperature of the soil. Both sunlit maize leaves and sunlit soil displayed the same temporal behaviour as the directional brightness temperature. However shaded maize leaves and shaded soil did not display the same temporal behaviour. This was caused by the structural parameters of the maize. As the maize was very young the vegetation height was about 10cm and the LAI 0.2. For high elevation sun angles the thermal image was dominated by the sunlit soil, as the amount of shaded soil was very small due to the height of the canopy. For very low sun angles the thermal image was dominated by sunlit vegetation. The sensitivity of the shaded components was therefore very low for these sparse low canopies.

During the AGRISAR campaign the emphasis of the measurements was on the effect of structural differences between crops on the directional brightness temperatures. Therefore the measurements were performed over more vegetation types, but with less temporal resolution (Figure 6-8). The points/lines represent the mean measured brightness temperature. The error bars denote the RMSE between the measured and the retrieved directional brightness temperatures. The RMSE for maize, wheat, sugar beet and barley was 2.85 K, 0.29 K, 0.75 K and 0.67 K, respectively. The measurements of the maize were left out for further investigation because of the high RMSE for maize, and the absence of more (temporal) measurements.

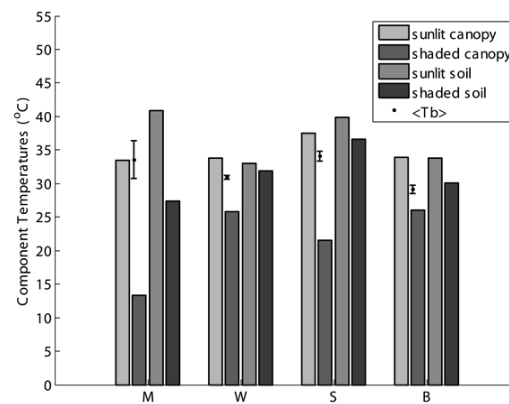


Figure 6-8: The retrieved skin temperatures of four components of different crops. The crops are maize (M), wheat (W), sugar beet (S) and barley (B). The dots represent the mean directional brightness temperature; the error bars represent the RMSE between the measured and modeled brightness temperatures. The measurements have been performed during different days in the AGRISAR field campaign.

The variation in the observed skin temperature differed between the crops. The largest variation between the component temperatures was found for sugar beet. Wheat and barley displayed similar behaviour. Both wheat and barley were considered very homogeneous as they were fully developed, had a large LAI, with similar leaves in terms of leaf angle scattering and absorption. The relatively small variations in the vegetation temperatures were caused by a high level of homogeneity. As the measurements were

performed during midday the soil temperatures were higher than the shaded vegetation temperatures.

The retrieval of skin temperatures of the different components by measured thermal directional brightness temperatures was successful for all crops except mature maize, for which the retrieval resulted in a large RMSE between the retrieved and the measured directional brightness temperature.

The values of the RMSE between retrieved and directional brightness temperature were influenced by the goniometric setup. In some of the thermal images the aluminium tracks of the goniometer were visible, and contaminated the measurements. These tracks had a significant lower brightness temperature than the vegetation or soil. The amount of track visible was much higher for low LAI with low vegetation height than for high LAI with high vegetation height. In the case of the mature maize (AGRISAR) a gap in the canopy caused the visibility of the tracks, even though the canopy had a high LAI and vegetation height. As the tracks usually have a significantly different temperature to the soil or canopy, the images may be filtered. As this is beyond the scope of this research it has not been considered.

6.4 Conclusion

A method was presented to retrieve up to four canopy component temperatures from directional measurements. The method inverted the SCOPE model to retrieve the four component temperatures (sunlit/shaded vegetation/ soil). The inversion was based on a modified Gauss-Newton optimization scheme. The modification incorporated the use of a priori knowledge to regularize the inversion problem.

The results of these sensitivity analyses proved that the algorithm is capable of using the extra information in the directional brightness temperature to retrieve the four component temperatures, and to a lesser extent the leaf area index. The retrieval of the sky temperature failed using this method. Only an improvement on the a priori information was observed when using multidirectional imagery. Here the success rate of the inversion was good for all solar zenith angles, most temperature profiles and all but the highest noise levels. When the temperature profile was completely homogeneous, the success rate was unsatisfactory. For homogeneous temperature profiles the added noise introduced a shape in the 'homogeneous' brightness temperature. The retrieval algorithm would then try to model this

shape resulting in a worse estimation of the component temperatures. Fortunately such a scenario is rarely observed, as sunlit components will almost always have a higher temperature than shaded components. In the case of cloudy days this scenario may occur, however the satellite will not be able to observe it. In reality therefore, this problem will not occur, and consequently the algorithm can still be used safely.

The method was finally tried, using the datasets from two field campaigns. These datasets included a temporal dataset over grass and maize, and a multi-crop dataset over maize, wheat, sugar beet and barley. The method produced good results for the component temperature. However the RMSE between the measured and retrieved directional brightness temperature exceeded sensor accuracy levels for certain scenarios. This was caused by the aluminium track of goniometric setup having a different temperature to the four canopy components. As these temperatures were not filtered out of the thermal images, they produced an RMSE of between 0.5K and 2.5K, depending on the LAI. As these errors were not present in the sensitivity analysis, which was performed with a low LAI, filtering the images to remove these tracks will certainly increase the efficiency of the inversion method.

7 Applying SCOPE for SEBS evaluation

Based on

Timmermans, J., Van der Tol, C., Verhoef, A., Verhoef, W., Su, Z. Van Helvoirt, M., Wang, L., Quantifying the Uncertainty in Estimates of Surface Atmosphere Fluxes by evaluation of SEBS and SCOPE models (in preparation),

Abstract

In this chapter, the Soil Canopy Observation, Photochemistry and Energy fluxes (SCOPE) model is applied to evaluate the Surface Energy Balance System (SEBS) model. For this purpose the SCOPE model was employed to both simulate remote sensing observations and act as a validation tool. The advantages of using the SCOPE model for this validation were a) the temporal continuity of the data, and b) the possibility of comparing different components of the energy balance.

The evaluation of the SEBS algorithm was performed over tall vegetation, as SEBS has not been validated over such a vegetation type yet. The data used in this research were obtained by the Reading University over their maize field in Sonning, United Kingdom. This dataset comprised a whole growth season of the maize crop. After the maize had reached its maximum LAI, the crop was thinned progressively during several stages.

The original SEBS algorithm produced large uncertainties in the turbulent flux estimations. The reason for these uncertainties was the misparameterization of the roughness height for heat transfer. Extra parameterizations for tall vegetation were implemented in the SEBS algorithm to correct for this. This improved the correlation between the SEBS and the SCOPE algorithm from -0.05 to 0.69, and decreased the flux magnitude error from 123 W m^{-2} to 94 W m^{-2} for latent heat, with SEBS latent heat being consistently lower than the SCOPE reference.

The diurnal stability of the evaporative fraction was also investigated. The evaporative fraction estimated by SCOPE over the maize field increased during the day. Consequently the daily evaporative fraction was higher than the evaporative fraction estimated at overpass time. As the evaporative fraction by SEBS was of the same order as the daily average value calculated by SCOPE, the temporal upscaling in SEBS did not cause extra uncertainty.

7.1 Introduction

Several interesting potential applications have been listed in the original Soil Canopy Observation, Photochemistry and Energy fluxes (SCOPE) paper (van der Tol *et al.*, 2009c). These applications range from estimating carbon uptake to directly characterising the photosynthesis. By monitoring the biochemical constituents (through inversion of the optical part of the SCOPE model) carbon uptake may be estimated. The presence of fluorescence in the model will greatly help to correctly estimate photosynthesis in future missions such as FLEX (Rascher *et al.*, 2008). In this chapter another very interesting application is considered, namely the testing of energy balance models and the interpolation of satellite imagery data between overpasses.

Accurate estimation of global evapotranspiration, ET, is considered to be of importance, due to its key role in hydrology and meteorology. Accurate estimation of ET is important for applications such as irrigation management, weather forecasting, and climate model simulations. Despite the importance of accurate ET estimates, no validated global evapotranspiration product exists that meets all spatial and temporal requirements for a comprehensive water cycle analysis. The SCOPE model presented in chapter 4 is able to estimate the evapotranspiration with great accuracy, but the model is too detailed and consequently too computationally demanding for global use. It is a challenge to try and find an algorithm suitable for a global scale, considering the spatial and temporal requirements.

Such an algorithm should include the most important exchange processes while retaining a minimum required number of input parameters. Remote sensing based evapotranspiration algorithms, such as Two Source Energy Balance (TSEB) and Surface Energy Balance Algorithm for Land (SEBAL), cannot be used to estimate global evapotranspiration because they either require local calibration (SEBAL) (Bastiaanssen *et al.*, 1998) or need too many input parameters (TSEB) (Kustas and Norman, 2000; Timmermans *et al.*, 2007). The Surface Energy Balance System SEBS (Su, 2002) circumvents the calibration problem by using a more physically based parameterization of the turbulent heat fluxes for different states of the land surface and the atmosphere (Su *et al.*, 2001). This is accomplished through implementation of the similarity theory (Monin and Obukhov, 1954; Obukhov, 1971; Brutsaert, 1999). Of the different available models, SEBS provides the best compromise between the level of detail of the model description on the one hand,

and the input requirements on the other. The SEBS algorithm has been validated locally for many low vegetation types (Jia *et al.*, 2003b; Su *et al.*, 2005a; Timmermans *et al.*, 2005; McCabe and Wood, 2006; Shan *et al.*, 2008).

Further validation of SEBS is problematic due to differences in spatial and temporal resolution between remote sensing observations and field measurements. Long time series of ET by remote sensing sensors are uncommon due to cloud contamination. Ground measurements are continuous and provide the desired temporal resolution. However spatial footprints of remote sensing sensors such as the Moderate Resolution Imaging Spectroradiometer (MODIS) and the Advanced Along-Track Scanning Radiometer (AATSR) are approximately 1 km², while footprints of ground measurements range between 100 m² to 250 m² for Bowen ratio stations (Pauwels and Samson, 2006; Pauwels *et al.*, 2008) and 0.1 km² to 0.3 km² for scintillometer stations (Hartogensis, 2006). Validation of the various heat fluxes using long time series of remote sensing imagery is therefore very difficult.

The objective of this research was to develop a methodology for evaluating SEBS (or any other remote sensing-based evapotranspiration algorithms for that matter) for 1 km² spatial and daily temporal resolutions. The application of a Soil Vegetation Atmosphere Transfer (SVAT) model (Oliso *et al.*, 1999) would be ideal for such an evaluation. In order to create long time series, the input for this SVAT model should be based mostly on meteorological parameters and other field data.

The recently developed Soil Canopy Observation of Photochemistry and Energy fluxes process, SCOPE, see chapter 4, presents us with the possibility of estimating turbulent heat fluxes and radiative transfer using only a limited amount of data. This SVAT model combines accurate estimates radiative transfer of optical and thermal radiation, through the unified SAIL radiative transfer model (Verhoef *et al.*, 2007), with a detailed representation of the biophysical processes through an extensive aerodynamic resistance model (Verhoef *et al.*, 1999) and a leaf-level energy balance. This SCOPE model was used to calculate the turbulent heat fluxes and the hyperspectral outgoing radiances. These radiances were converted into sensor bands using a sensor simulator (Timmermans, 2009). These band observations were then fed through the SEBS pre-processor for the calculation of Land Surface Temperature (LST), albedo and emissivity (Sobrino *et al.*, 2004). Finally turbulent heat

fluxes estimated by the SEBS algorithm was compared to those simulated by the SCOPE model

7.1.1 Methodology

In this investigation the SCOPE model was coupled to the SEBS model. SCOPE was used to estimate both the turbulent fluxes and the hyperspectral radiative transfer. Through a sensor simulator and the SEBS pre-processor the input variables for the SEBS algorithm were calculated using these observations. This way the SCOPE model acted as a forcing and validation tool for the SEBS algorithm. This methodology is illustrated in Figure 7-1.

The advantage of simulating top-of-canopy AATSR radiances instead of using top-of-atmosphere measurements is that uncertainties in the atmospheric correction are circumvented. Instead of simulating TOA radiances (and applying atmospheric correction to estimate the TOC radiances), TOC radiances are directly simulated forgoing the atmospheric correction and its related uncertainties. Therefore, only the mismatch in parameterizations between SEBS and SCOPE contributes to the errors in the daily evapotranspiration. Also, this methodology enables estimation of evapotranspiration beneath clouds and is therefore suitable for creating long time series. This capability in combination with a sensor simulator enables the model to reproduce past, current and future satellite sensors observations (Verhoef, 2008; Timmermans *et al.*, 2009).

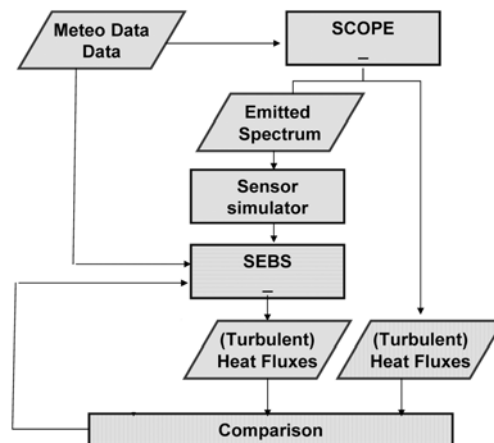


Figure 7-1: Methodology flowchart for comparing SEBS with SCOPE

In this research the investigation into the SEBS uncertainties focuses mainly on the effect of high/dense vegetation types on the daily evapotranspiration, because SEBS has so far only been validated for low and sparse vegetation types (Jia *et al.*, 2003b; Su *et al.*, 2005a; Timmermans *et al.*, 2005; McCabe and Wood, 2006; Shan *et al.*, 2008). For high vegetation types some of the parameterizations in SEBS might fail due to the complex nature of the turbulent heat exchange. Of special interest in this chapter are the height dependence of the aerodynamic resistance estimation and its dependence on the roughness height for heat, and the diurnal stability of the evaporative fraction.

7.1.2 Surface Energy Balance

The Surface Energy Balance System, SEBS, was developed by Su (Su, 2002) for the estimation of atmospheric turbulent fluxes using satellite earth observation data. SEBS is a remote sensing algorithm for estimating (daily) evapotranspiration. It consists of a set of tools for the determination of the land surface physical parameters and variables, such as albedo, emissivity, surface temperature, and vegetation coverage, from spectral reflectance and radiance data (Su, 1996; Su *et al.*, 1999). It includes an extended model for the determination of the roughness height for heat transfer (Su *et al.*, 2001) and for the estimation of the evaporative fraction on the basis of the energy balance in limiting cases.

SEBS makes use of the energy balance, equation (7-1), to estimate the latent heat flux at the time of overpass. In order to scale from the instantaneous to the daily time scale the evaporative fraction, EF, is used in equation (7-2). This EF is assumed to be constant over the course of a day.

$$R_n = G_0 + H + \lambda E, \quad (7-1)$$

$$\Lambda = \frac{\lambda E}{R_n - G} = \frac{\Lambda_r \cdot \lambda E_{wet}}{R_n - G}, \quad (7-2)$$

$$\Lambda_r = 1 - \frac{H - H_{wet}}{H_{dry} - H_{wet}}, \quad (7-3)$$

where, R_n is the net radiation [W m^{-2}]; G_0 the soil heat flux [W m^{-2}]; H , H_{dry} , and H_{wet} are the actual, dry limit and wet limit sensible heat [W m^{-2}] flux, respectively; λE and λE_{wet} are the actual latent heat [W m^{-2}] fluxes at overpass and at the hypothetical wet limit; and

Λ and Λ_r are the evaporative fraction ($\lambda E/(R_n-G)$ [-]) and the relative evaporation [-].

In the original formulation, SEBS calculates evapotranspiration based on the net radiation, the ground heat flux and the evaporative fraction. The net radiation is calculated using incoming shortwave radiation, albedo, air and land surface temperature, and emissivity. The ground heat flux is estimated based on the weighted average of ground heat flux over vegetated (Monteith, 1973) and bare soil (Kustas and Daughtry, 1989). The evaporative fraction is estimated through the relative evaporation using the sensible heat fluxes (Eqs. 7-2 and 7-3). This sensible heat flux is calculated iteratively through the use of the Obukhov length and the friction velocity. The equations required to calculate the evapotranspiration, ground heat flux and the sensible heat flux are shown in equations (7-4), (7-5), (7-6) and (7-7).

$$\lambda E = \Lambda(R_n - G_0) \quad (7-4)$$

$$G_0 = R_n(\Gamma_c + (1 - f_c)(\Gamma_s - \Gamma_c)) \quad (7-5)$$

$$H = \rho_a C_p \frac{(\theta_o - \theta_a)}{r_a} \quad (7-6)$$

$$r_a = \frac{[\ln(h_c/z_{0h}) - C_w]}{ku_*} \quad (7-7)$$

where f_c is the fractional vegetation cover [-]; Γ_c and Γ_s are the values of the ratio of ground heat flux to the net radiation in the case of a full canopy and bare soil, respectively; ρ_a is the density of air [kg m^{-3}]; C_p is the specific heat coefficient of air [$\text{J kg}^{-1} \text{K}^{-1}$]; r_a is the aerodynamic resistance [s m^{-1}]; k is the von Karman constant; u_* is the friction velocity [m s^{-1}]; θ_o and θ_a are the potential temperatures of, respectively, the land surface and the air [K]; h_c is the height of the vegetation [m]; C_w is the atmospheric stability correction term, and z_{0h} is the roughness height for heat [m].

The atmospheric stability correction depends on the state of the atmosphere and the measurement height. In SEBS C_w is calculated using the Monin-Obukhov Similarity theory (MOS) if the measurements are performed within the atmospheric surface layer,

and Bulk Atmospheric Similarity theory BAS is used if the measurements are performed above this surface layer. The roughness height for heat is calculated based on the roughness height for momentum, z_{0m} , through the $kB^{-1} = \ln(z_{0m}/z_{0h})$. This kB^{-1} (Massman, 1999; Su *et al.*, 2001) is calculated based on the weighted average between limiting values of soil and full canopy, as is shown in equation (7-8).

$$kB^{-1} = kB_c^{-1} f_c^2 + kB_m^{-1} f_s f_c + f_c^2 kB_s^{-1} \quad (7-8)$$

where, f_s is the fractional soil coverage. The bare soil contribution is calculated as $kB_s^{-1} = 2.46(\text{Re}_*)^{1/4} - \ln(7.4)$, with Re_* being the roughness Reynolds number. The full canopy contribution is given by $kB_c^{-1} = kC_d / [4C_t \beta (1 - e^{-n/2})]$, with C_d being the drag coefficient of the leaves, C_t the heat transfer coefficient of the leaves [$\text{W m}^{-1} \text{K}^{-1}$], β the ratio between the friction velocity and the wind speed at canopy height, and n the cumulative leaf drag area. Finally, the soil-canopy interaction contribution is calculated using $kB_m^{-1} = k\beta z_{0m} / (C_t^* h_c)$, with C_t^* being the heat transfer coefficient of the soil [$\text{W m}^{-1} \text{K}^{-1}$].

7.1.3 Evaporative Fraction

The EF in SEBS is calculated based on the relative evapotranspiration. Therefore the EF depends on the actual sensible heat flux, and on the sensible heat flux at the hypothetical dry and wet limit. The sensible heat flux at these limits is based on the maximum available energy for the dry scenario, while for the wet scenario H is calculated from $R_n - G_0 - \lambda E$, with λE being derived from the Penman Monteith equation. The evaporative fraction is calculated by SEBS at the time of overpass and considered to be constant during the rest of the day. However several researchers have reported a diurnal dependence of the evaporative fraction (Farah *et al.*, 2004; Li *et al.*, 2008; Lu and Zhuang, 2010).

7.2 Experimental Setup

The meteorological data used for the forcing of the SCOPE model was obtained at the University of Reading Crops Research Unit experimental site (Sonning, United Kingdom). The data set comprised

of several micrometeorological variables, such as the air temperature T_a , the wind speed U_a , and actual vapour pressure E_a (see van der Tol et al., 2009b, for a detailed overview of the site, and sensors used) and radiation measurements.

The advantage of this particular dataset, and the reason why it was chosen, was the fact that the canopy was thinned out after the maximum canopy height and LAI (3.7) were achieved. The LAI values obtained after this thinning were approximately 2.0, 1.0, 0.5 and 0.25. Leaves were systematically removed from the canopy, without modifying the height of the crop. This change showed up clearly in the different surface parameters measured (Figure 7-2). The stepwise change in leaf area density provided a perfect dataset for testing the quality of the LAI retrieval methods and the effect on the surface energy balance.

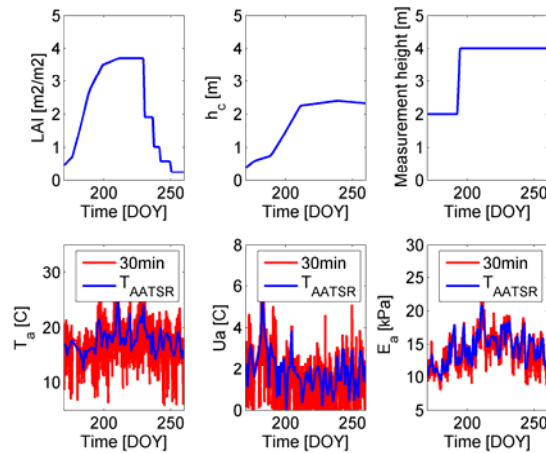


Figure 7-2: SCOPE input parameters measured at the Sonning site, 2002.

The red lines depict half hourly in situ measured data, and the blue lines depict the values at AATSR overpass time (T_{aatsr}).

7.3 Results

7.3.1 Roughness heights

The sensible heat flux in SEBS was calculated using equations (7-6) and (7-7), employing the aerodynamic resistance and the difference

in potential temperature between the land surface and the atmosphere at measurement height. This resistance was shown in the previous section to depend on the roughness height for heat, the friction velocity and the logarithmic profile of the wind speed. (Jacobs *et al.*, 1989; Liu *et al.*, 2007b) found that the value of aerodynamic resistance for maize ranged from 20 to 50 s/m. However, using the original SEBS parameterizations, this research found the resistance to vary between 80 and 200 s/m, resulting in an unrealistically low sensible heat flux compared to the measured maize H -values.

The error in the aerodynamic resistance appeared to be caused by the parameterization of the roughness height for heat. In the original SEBS parameterization this roughness height was estimated based on kB^{-1} . In SEBS this variable is usually higher than 8.0, as the roughness height for momentum is always higher than the roughness height for heat, except for bare soils, for which negative values of kB^{-1} have been found (see Verhoef *et al.*, 1997b). However, kB^{-1} values may be calculated from the direct measurements (Liu *et al.*, 2007b) or in this case from SCOPE simulations. This method is shown in equation (7-9).

$$kB^{-1} = \rho_a C_p \frac{(T_s - T_a)}{H} k u_* - \ln\left(\frac{z_{ref} - d_0}{z_{0m}}\right) + \Psi_h\left(\frac{z_{ref} - d_0}{L}\right) \quad (7-9)$$

where T_s and T_a are the temperatures for land surface and the atmosphere [K], z_{ref} is the measurement height [m], d_0 is the displacement height [m], and Ψ_h is the MOS atmospheric stability function for heat [-]. As shown in Figure 7-3 the minimum value for kB^{-1} was -0.5. This low value was attributed to the height of the canopy. In high, dense vegetation the incoming radiation only affects the leaf temperature in the upper parts of the canopy, in the lower region the radiation is absorbed too much to play a significant role in the temperature of the leaves (Jia, 2004; Liu *et al.*, 2007b). However these leaves or twigs still play a role as part of the sink for momentum. This process is well represented in the SCOPE model, as the radiative transfer in this model is more accurately represented than in the SEBS model. Instead of the original parameterization in SEBS the method of (McNaughton and van den Hurk, 1995; Bosveld *et al.*, 1999) for kB^{-1} was used for high values of LAI and h_c , see equation (7-10).

$$kB^{-1} = 52 \frac{\sqrt{u_* l}}{LAI} - 0.69 \quad (7-10)$$

where l is the characteristic length for the canopy; in the maize canopy this corresponds to a leaf width of 0.03 m. The temporal variability in kB^{-1} according to this method is shown in Figure 7-3, along with the temporal variability of kB^{-1} calculated using the original method employed in SEBS, and with the values based on the SCOPE estimations.

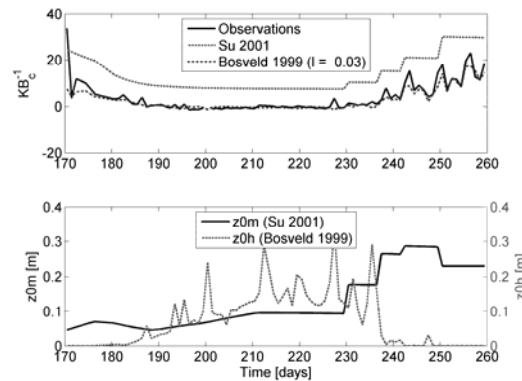


Figure 7-3: Variation of kB^{-1} over a whole growth season of maize.

In the top panel, three kB^{-1} values are shown: measured, calculated from the observations, estimated from using parameterizations of Su (2001) and Bosveld et al. (1999). In the bottom panel the roughness momentum for heat and momentum in SEBS (Su, 2001) is shown together with the roughness height for heat calculated from the new kB^{-1} parameterization (Bosveld et al. 1999)

It is obvious that the new parameterization of kB^{-1} correlated much better with observed values than the original SEBS parameterization. Even the thinning of the LAI was clearly characterized using this method, as is illustrated by the good fit of kB^{-1} at the end of the measurement period. However the method is only applicable to closed canopies, and is less accurate for low vegetation. Therefore it was opted to use this method only when the LAI was above the threshold value of 1.5 and only when $h_c > 1\text{m}$.

7.3.2 Instantaneous heat fluxes

Finally, after implementation of the new parameterizations for high canopy types, the surface heat fluxes could be calculated. The results of these calculations are shown in Figure 7-4. In this figure the net radiation, ground heat flux, sensible heat flux and the latent heat fluxes are shown.

All SEBS estimated fluxes had a high correlation with the SCOPE estimated values for the fitted values.

- The net radiation of SEBS and SCOPE were strongly correlated and fitted with a slope of 0.81 and a RMSE = 54W/m^2 . The (optical) reflected and thermal radiation as measured for the maize canopy, were very similar to those predicted by SCOPE (not shown); this implied that the LST, albedo and emissivity were retrieved correctly from the SCOPE simulations. The difference in net radiation arose because SEBS uses air temperature to calculate the longwave incoming radiation (Brutsaert, 2009). However, the variation in the downwelling diffuse radiation for medium cloud coverage could not be taken into account using solely the air temperature. Instead incoming thermal radiation should be based on measurements. This was observed most clearly for day 186 when the differences in net radiation were the highest.

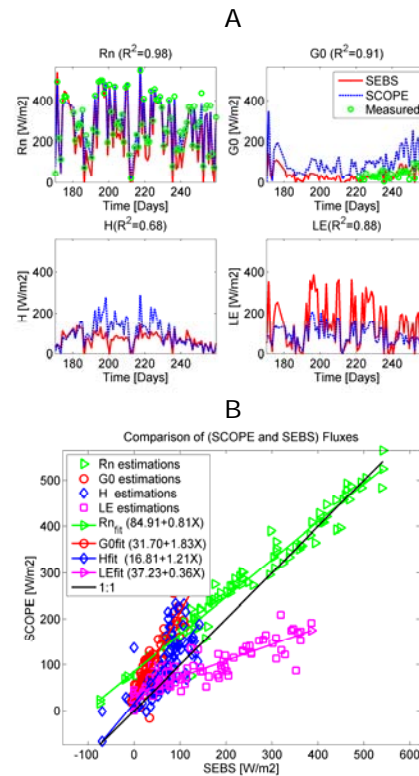


Figure 7-4: Comparison of surface heat fluxes predicted by SEBS and SCOPE.

In panel A the diurnal measurements and estimations are shown. There were no measurements of sensible heat and latent heat over the thinned maize field. In panel B the scatter plot between SEBS and SCOPE estimated heat fluxes is shown. The instantaneous surface heat fluxes from SEBS show a high correlation with the SCOPE estimated surface heat fluxes. SEBS underestimates the sensible heat flux for a fully developed maize canopy (between day 200 and 220).

- The ground heat flux calculated by SEBS was much lower than the SCOPE estimated ground heat flux, because SCOPE estimated the ground heat flux using the Force-Restore method to close the energy balance. Consequently the soil temperatures can be too high. The differences between the measurements and the SEBS derived ground heat flux were acceptable (RMSE=18 W/m²), while the difference between SCOPE and SEBS was not (RMSE= 84 W/m²).

- The estimation by SEBS of the sensible heat flux was much improved using the new parameterization for the roughness height of heat. The differences between SEBS and SCOPE decreased using the new parameterization, from 100 W/m² to 56 W/m²; the correlation increased from -0.07 to 0.68. Only for high *LAI* values was SEBS underestimating the sensible heat. This indicates that additional processes, not covered by this new parameterization in SEBS, played a role.
- The latent heat flux calculated by SEBS was higher than the latent heat flux predicted by SCOPE. The new parameterizations improved the estimation of λE , as illustrated by the reduction in RMSE from 123 W/m² to 94 W/m². This difference is mainly due to the overestimation of the evaporative fraction for very high *LAI* s. In Figure 7-4 this can be clearly observed, as the slope of the sensible heat flux deviates as much from the 1:1 line as the slope of the latent heat flux (but in opposite directions). This is investigated further in the next section.

7.3.3 Evaporative fraction

In order to scale the estimates at overpass time up to a daily (24-hour) value, a method was needed to characterize the diurnal cycle of the fluxes (Rauwerda *et al.*, 2002; Shan *et al.*, 2008). In the SEBS model it is assumed that the evaporative fraction is constant over the day, and consequently can be used to scale up from instantaneous to daily values.

Combining SCOPE and SEBS allowed the investigation of not only the diurnal pattern of EF, but also the uncertainties of EF at overpass time and the daily average of EF. The results of the comparison are shown in Figure 7-5. Here, the diurnal pattern of the evaporative fraction is shown for the complete growing season, for all individual days (the left panel), and for a 10-day average.

As expected, the evaporative fraction at night was much lower than the evaporative fraction during the day, as the latent heat was close to zero. Most days the evaporative fraction varied (i.e. was not constant) during the day time, with the exception of days showing low *LAI* values. This was most clear in studying the diurnal variation of the 10-day average EF values. The 10-day average EF remained stable for the days 170-180, 240-250 and 250-260. These days corresponded to low *LAI* values of 0.25, 0.5 and 0.25, respectively. For days 230-240, (*LAI* = 1.0) the evaporative fraction started to

vary diurnally. For all other days (i.e. those with a $LAI > 1.0$) EF had a pronounced diurnal pattern. For $LAI > 2.0$ EF had the same pattern: with EF being lower in the morning than later in the day. Therefore the average evaporative fraction was higher than the instantaneous evaporative fraction.

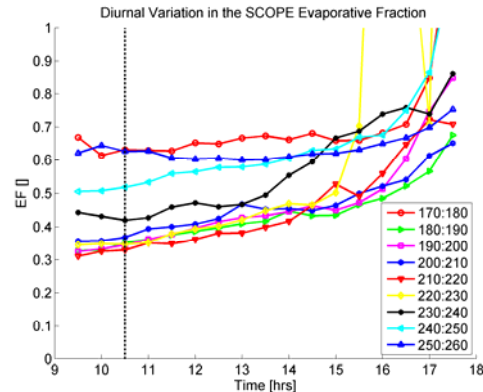


Figure 7-5: Diurnal evaporative fraction variation during maize growing season.

The 10-day average of the diurnal evaporative fraction is shown as calculated with SCOPE. The dotted line represents the overpass time of AATSR.

Figure 7-6 shows both the instantaneous evaporative fractions at overpass time calculated by SEBS and SCOPE and the daily average values of the evaporative fraction calculated by SCOPE. In all cases the daily evaporative fraction was higher than the instantaneous EF by SCOPE, except for the low LAI classes (at the very start and end of the period), as shown in Figure 7-5. This originates because the sensible heat decreases during the day in comparison to the latent heat.

The comparison between instantaneous/daily average evaporative fractions by SEBS and SCOPE was hampered by the large variation in the SEBS evaporative fraction. This variation occurred when net radiation was very low. In these cases the evaporative fraction predicted by SEBS was very low. The explanation for this low net radiation was given in the previous paragraph. When only taking the medium values into account, the instantaneous evaporative fraction by SEBS was much higher than the instantaneous evaporative fraction of SCOPE. As shown in Figure 7-4 this was due to an underestimation by SEBS of the sensible heat for high LAI values, which should be further explored in future. Fortunately, when the

instantaneous evaporative fraction values were compared with the daily averaged ones they were of the same order.

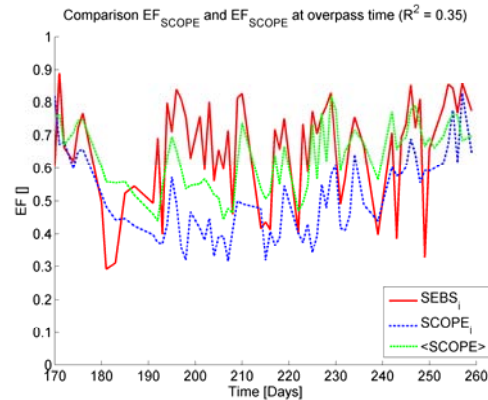


Figure 7-6: Variation in evaporative fraction for a maize whole growing season. Evaporative fractions at overpass time calculated by SEBS and SCOPE are shown, as well as the daily average values of the evaporative fraction by SCOPE.

7.4 Conclusions

In this chapter a method was successfully presented for validation/investigation of the SEBS model. This method used the SCOPE model to estimate the turbulent heat fluxes from a canopy and the band radiances. These radiances were then fed through the SEBS pre-processor in order to obtain surface variables such as LST, albedo and emissivity. The data used for this comparison comprised micrometeorological driving and verification data for a complete growth season of maize. After the maximum *LAI* was reached, leaves were removed from the canopy, without altering the height of the vegetation. This thinning of the canopy resulted in an ideal dataset for investigation of the impact of different *LAI* classes. Accordingly, the fractional vegetation cover was inversely related to this thinning.

It was shown that the parameterization in SEBS for tall vegetation produced large uncertainties in the actual sensible heat and (consequently) the latent heat. In high dense canopies most of the radiation was absorbed by the leaves at the top of the canopy. Therefore the virtual source of the sensible heat, as expressed by z_{0h} , was relatively high in the canopy compared to in low vegetation.

This physical process was not characterized correctly in the original parameterization undertaken. In order to take this effect into account, a simple parameterization based on *LAI* and friction velocity was implemented in SEBS. This change in parameterization resulted in an improvement of the correlation between the SEBS and the SCOPE modelled sensible heat flux from -0.07 to 0.68. After implementing the new parameterization, the different heat fluxes and the evaporative fraction were calculated. Even though the roughness height for heat was improved greatly using the new parameterizations, SEBS still underestimated the sensible heat flux for high *LAI* values. This means that some processes were still not characterized well enough with the new parameterizations and further investigation will be required.

Finally the (instantaneous and daily) evaporative fraction, EF, calculated by SEBS and SCOPE were compared. SCOPE showed an increase in the diurnal pattern in the evaporative fraction. Therefore the daily average of EF by SCOPE was higher than the values obtained at overpass time. EF from SEBS, on the other hand, was of the same order as the SCOPE daily averaged evaporative fraction. This originated from the low values of the SEBS estimated instantaneous sensible heat. Although this SEBS characterization of the sensible heat flux over tall vegetation could be improved, estimations by SEBS could still be used for daily evapotranspiration estimations because the obtained value for the evaporative fraction appeared to represent the daily average correctly.

In conclusion, the methodology presented in this chapter has enabled a thorough investigation in the different parameterizations of SEBS. The advantage of the method presented in this chapter, i.e. combining SEBS with SCOPE, is that for days where there are no acquisitions we can still continue. Although no actual remote sensing imagery was used, the methodology, using the sensor simulator, proved the viability of using the AATSR sensor for calculating the different land surface fluxes. At the moment the SCOPE model overestimates the ground heat flux, a problem that should be addressed with the development of its next version.

8 Concluding Remarks

8.1 *Synthesis*

Over the past few years both the quality and availability of detailed remote sensing data have increased remarkably. The spatial, temporal, and spectral resolutions of the data products have all increased greatly over the past decades. In addition, several satellites have been launched offering the possibility of acquiring images from multiple viewing directions. Together these improved observations provide the potential of estimating the land surface processes with higher accuracy than can be performed with single view nadir observations. However this potential is only partially used, as current remote sensing algorithms have been built on concepts that were created several years before the idea of these new satellites was conceived.

Remote sensing algorithms for estimating biophysical processes and detailed radiative transfer can be improved if both processes are integrated. Current remote sensing algorithms use biophysical parameters, which are estimated a priori and are based on inversion of radiative transfer models. Most remote sensing algorithms were built with the assumption of a homogeneous land surface; only few remote sensing algorithms recognise the difference in the processes in the soil and the vegetation part of the land surface. More advanced radiative transfer models and corresponding inversion algorithms are lacking. Consequently the spectral and angular signatures present in the remotely sensed data can only partially be exploited by the available remote sensing algorithms.

The increase in our understanding of the biophysical land surface processes has shown that more accurate estimations of the photosynthesis and evapotranspiration are needed. For this purpose several surface vegetation atmosphere transfer models have been produced in the past decades. However, these SVAT models oversimplify the radiative transfer within the canopy, or only use specific wavelengths out of the total spectrum. In short, a SVAT model that incorporates hyperspectral radiances for the estimation of turbulent fluxes and outgoing (directional) radiances does not exist.

The objective of this study was to develop a new SVAT model that integrates directional radiative transfer and complex biophysical/biochemical processes. The most important aspect of such a model is that it should be capable of estimating the exchange

of heat, water vapour and carbon fluxes at the land-atmosphere interface directly from directional observations.

8.2 Field measurements

As a dataset with ground based directional radiative measurements did not exist at the start of the study, such a database needed to be created. In **Chapter 2** the goniometric system is presented that was used in this research. Modification to the system enabled reliable and fast observations of directional radiative signatures in both the optical and thermal spectrum. This goniometric system was employed in different field campaigns over eight land surface types in total: short and tall grassland, young and mature maize, barley, wheat, sugar beet and vineyard. Concurrently to these directional radiative measurements, skin temperature measurements were taken of different land surface components. These measurements were intended partly for identification of the most important components of the land surface and partly for validation of future retrieval algorithms.

Identification of the most important components of the land surface was performed in **Chapter 3**, on the basis of both directional radiative measurements and skin temperature measurements. First the most complex vegetation type was identified. Two parameters were defined in order to identify the most complex vegetation type in the database objectively. These parameters were: the optical structure parameter (calculated for the visible, near infrared and mid infrared part of the spectrum) and the thermal separation parameter for the thermal infrared part of the spectrum. The vineyard crop proved to be the most complex vegetation type in the database.

Using the skin temperature measurements of different components within the vineyard crop the most important land surface components were defined. These were: sunlit soil, shaded soil, sunlit leaves and shaded leaves. Vertical variation within the sunlit and shaded leaves was also identified in the observed skin temperatures, but was of a lower order than the variation resulting from the difference between sunlit and shaded leaves. Consequently the SVAT model to be constructed needed to be able to distinguish between sunlit/shaded soil/canopy. In some scenarios the effect of light extinction within the canopy might arguably start to play a larger role. Therefore the possibility of incorporating vertical leaf temperature also needed to be investigated.

In **Chapter 3** a simple retrieval method was applied to retrieve skin temperature, using optical data to distinguish between the different components. This method made it only possible to retrieve the skin temperatures of soil and leaf components, without further distinction between sunlit and shaded parts. Variation in the retrieved soil temperature values showed that the soil could have been divided into a sunlit and a shaded component. It is also shown that the method could not be used to distinguish between individual sunlit and shaded leaves.

8.3 Modelling

Using the conclusions from **Chapter 3**, an integrated SVAT model was constructed, which not only identified the four components (sunlit/shaded soil/leaves), but was also able to characterise a vertical temperature distribution. This integrated model, called SCOPE and presented in **Chapter 4**, was able to estimate biophysical and biochemical processes. The model combined detailed radiative transfer within the canopy and biophysical processes through the use of an energy balance at leaf level. This made it able to distinguish not only between sunlit and shaded leaf components, but also between leaves high and low in the canopy, and to account for the various leaf orientations with respect to the sun. Using the different sub-models, the turbulent fluxes at different positions within the canopy and the outgoing hyperspectral radiances were calculated. While most of the sub-models had been validated in previous research, the discrete radiative transfer model was newly developed and hence needed to be validated.

8.4 Validation

The validation of the discrete radiative transfer part of the SCOPE model was performed in **Chapter 5**. For this purpose the radiative transfer part of the SCOPE model was compared with the architecturally more complex SLC and DART models. Although the radiative transfer part of the discrete SCOPE model is based on the same principle as the analytical SLC radiative transfer model, differences between the two were found. These differences were due to the finite size of the discrete layers within the SCOPE model. A modification was implemented in the model that solved this error.

After this modification the SCOPE model was compared with the DART 3D radiative transfer model. Several scenarios were tested, ranging from very simple (bare soil) to very complex (extremely

Concluding Remarks

clumped vegetation). The data needed for constructing the scenarios were obtained by terrestrial laser scanning and several 3D filter operations. Parameters obtained were tree position, trunk diameter, vertical LAI distribution, and crown cover. The comparison between DART and SCOPE showed good agreement between the two models for all but the more complex clumping scenarios. The two models were in agreement for all observations except for the near-hotspot viewing angles. As DART employs the same hotspot effect parameterization as the SCOPE model, further analysis is needed to solve this discrepancy. As the other viewing angles showed good agreement, this analysis was not performed as part of this study.

In addition to the comparison between SCOPE and DART, a comparison between the SLC radiative transfer model and the DART model was performed in **Chapter 5**. This was done to show the potential for introducing clumping and shape factors into the model. The SLC model showed better agreement with the more complex DART scenarios. Only when the canopy became extremely sparse, and DART BRDFs started showing azimuthal dependence did the differences between SLC and DART become unacceptable. Future implementations of clumping parameterizations such as implemented in the SLC model will improve the SCOPE model to the required level.

8.5 Applications

Applications of the SCOPE model are described in **Chapter 6 and 7**. In **Chapter 6**, the retrieval of skin temperatures of different components through inversion of the SCOPE model is presented for the characterisation of the biophysical/biochemical processes. This inversion used both a priori Bayesian information and singular value decomposition to reduce and diagnose the ill-posedness of the inversion problem. A sensor simulator was developed to convert the hyperspectral (thermal) radiances into sensor observations. In a sensitivity analysis several sensors, skin temperature scenarios and noise levels were simulated. This way the potential of multi-directional observations was tested.

Skin temperatures of the four components could successfully be retrieved from multi-directional observations for noise levels well exceeding real-life values. Using these directional observations, air temperature and LAI were also retrieved. Although the LAI retrieval showed promising results, the air temperature retrieval failed, due to low sensitivity of the directional thermal signature to this variable. The addition of extra variables to be retrieved did not result in a significant decrease in the success rate for the retrieval of the four

skin temperatures. It was therefore concluded that this algorithm may be used as a post processing step for increasing the accuracy of the a priori estimated LAI. The skin temperatures of the different components could not be retrieved using mono-directional observations, proving the potential multi-directional observations have over mono-directional observations.

For computational efficiency the leaf energy balance was not included in this inversion. Consequently no vertical profile of sunlit and shaded leaves was retrieved. In real life applications, however, the energy balance may be used to accurately estimate these vertical distributions as well.

In **Chapter 7**, the SCOPE model was used to evaluate the SEBS remote sensing algorithm. In this chapter a methodology was described which used the SCOPE model as both forcing and evaluation tool for the SEBS algorithm. SCOPE was run on the basis of meteorological and radiative measurements over a maize field. The dataset used in this application comprised a full growing season of maize, which was progressively thinned once the vegetation had reached its highest LAI. The input variables for the SEBS algorithm were obtained through the radiative simulations of the SCOPE model, an upgraded version of the sensor simulator presented in chapter 6, and the SEBS pre-processor.

It was shown that SCOPE was able to characterise the processes within such a tall canopy correctly. SEBS on the other hand produced large uncertainties in the sensible heat due to a misparameterization of the roughness length for heat. Incorporating a new parameterization in the SEBS algorithm partly solved this problem. However, errors in the SEBS estimations remained high, and more investigation into the SEBS parameterizations will need to be performed in the future.

In addition, the evaporative fractions as calculated by both SCOPE and SEBS were compared. While SEBS can only estimate the evaporative fraction during the overpass time of the satellite, SCOPE is able to estimate this variable for a half hourly temporal resolution. It was found, in contradiction to public assumption, that the evaporative fraction calculated by SCOPE displayed a diurnal pattern; the evaporative fraction increased during the day over the maize field. Consequently the daily evaporative fraction by SCOPE was larger than the evaporative fraction calculated by SCOPE at satellite overpass time. SEBS overestimated the evaporative fraction at overpass time in comparison with SCOPE. This SEBS value was,

fortunately, of the same order as the SCOPE daily value, and therefore did not introduce extra uncertainty in the SEBS daily evapotranspiration estimations.

8.6 Limitations

The research in this manuscript is based under several assumptions. Consequently the model will not be applicable to all scenarios. In this section the complete list of limitations is discussed.

- The acquisition of the directional signatures was performed under the assumption of constant direct and diffuse illumination of the canopy and its thermodynamic stability. While no radiative measurements were performed to verify this, the skin temperature measurements showed that for the vineyard, tall grass and young maize this assumption was met for acquisition times between 09h00 and 18h00. For the other directional radiative measurements such skin temperatures were not measured and consequently thermal equilibrium might not be assured. We are, however, confident that the variations are minimum, as the brightness temperatures of the thermal images showed little variation between the beginning and end of the acquisitions.
- Identification of the most important land surface components was performed for the vineyard. In this crop the vertical distribution of leaf temperature is low compared to the difference between sunlit and shaded leaves. In a crop with less clumping, the incoming radiation is vertically more affected, and consequently the vertical distribution will be larger. While in tall grass this effect was found to be only minor, in more dense vegetation (for instance barley) this could play a significant role. As the SCOPE model is also able to estimate the radiative transfer within the canopy, it is also able to describe the vertical temperature distribution within the canopy, and consequently this limitation is only minimal.
- The built-in radiative transfer part of the SCOPE model was compared with different scenarios simulated by DART. In this case DART was used as a reference, and consequently assumed to be perfect. However, other studies have shown that DART does not always estimate the radiative transfer correctly. A better way to validate the radiative transfer model would be to use real data. However, this would have been complicated as a dataset similar to the scenarios used in the comparison does not exist.
- It was stated that the use of a clumping parameterization similar to the SLC implementation would greatly improve the

SCOPE model. However, such a parameterization will be very difficult, as no SLC model exists that takes thermal radiation into account.

8.7 Related to the Objectives

In retrospect, the objectives set at the beginning of this research were successfully achieved. An integrated model, SCOPE, was presented (Objectives 1 & 4). SCOPE was constructed, on the detailed (Objective 3) understanding of directional radiative transfer in canopies, and their effect on photosynthesis, evaporation, transpiration. This understanding was obtained by thorough investigation of several directional observations (Objective 2) and skin temperature measurements over different crops with varying complexity. SCOPE identified four canopy components directly, and by incorporating a leaf energy balance, also a vertical distribution. Comparing SCOPE with the more complex SLC and DART radiative transfer models (Objective 5) showed good agreement even for even slight crown clumping, and potential future solutions in the case of more extreme crown clumping. The skin temperatures of the different components were retrieved using an inversion algorithm (Objective 6), using a priori information and the multi-directional radiative measurements in the database. SCOPE was capable of retrieving a vertical distribution of the skin temperatures and estimating biophysical/biochemical processes where meteorological data were also available. Finally (Objective 7), the potential of the model for evaluating remote sensing energy balance models was presented.

8.8 Outlook

Some applications of the SCOPE model have already been indicated in this research. Other, potential applications of the SCOPE model are:

- **Estimation of plant physiology.** SCOPE uses the PROSPECT model to couple biochemical concentrations in the leaf, such as chlorophyll and water content, to the radiative transfer of the canopy. Inversion of the SCOPE model enables the estimation of plant physiology and carbon uptake. However, the variables used in the PROSPECT model currently are not coupled to the biochemical processes, and this will need to be performed prior to such an inversion.
- **Validation/simulation of future satellites.** At present SCOPE is the only SVAT model available able to integrate the effect of biophysical processes into simulated remote sensing observations. The effect of evaporation and transpiration is

Concluding Remarks

most clearly observed in the thermal part of the spectrum, while photosynthesis has a large effect on the fluorescence signal. Therefore SCOPE is an ideal tool for the simulation/validation of the future FLEX mission.

- **Synergistic use of current multiple sensors.** As SCOPE is able to simulate different satellite sensors, it is ideal for combining different satellite observations. Currently most of the remote sensing algorithms do not have a radiative transfer model embedded for retrieval purposes. Instead they use a priori retrieved variables from other models (mostly using vegetation indices such as NDVI). Because these vegetation indices are band-dependent, combining different satellites is difficult. The SCOPE model is able to directly estimate biophysical processes on the basis of incoming radiation, and can consequently be run sensor-independent. Combining different satellites not only increases the temporal resolution of the data product, but also increases the accuracy. Some sensors have a high spatial resolution, but only provide limited spectral resolution, and vice versa.

9 Bibliography

- Review of Canopy Reflectance Modelling.
- Allen, R.G., PEREIRA, L.S., Raes, D., Smith, M., 1998. FAO Irrigation and Drainage Paper. Rome, Italy.
- Anderson, M.C., Norman, J.M., Kustas, W.P., Houborg, R., Starks, P.J., Agam, N., 2008. A thermal-based remote sensing technique for routine mapping of land-surface carbon, water and energy fluxes from field to regional scales. *Remote Sens. Environ.* 112, 4227-4241.
- Anderson, M.C., Norman, J.M., Mecikalski, J.R., Torn, R.D., Kustas, W.P., Basara, J.B., 2004. A multiscale remote sensing model for disaggregating regional fluxes to micrometeorological scales. *JOURNAL OF HYDROMETEOROLOGY* 5, 343-363.
- Asner, G.P., 1998. Biophysical and Biochemical Sources of Variability in Canopy Reflectance. *Remote Sens. Environ.* 64, 234-253.
- Babatunde, E.B., Akoshile, C.O., Falaiye, O.A., Willoughby, A.A., Ajibola, T.B., Adimula, I.A., Aro, T.O., 2009. Observation bio-effect of SW-global solar radiation in Ilorin in the tropics. *Advances in Space Research* 43, 990-994.
- Baldocchi, D., Falge, E., Gu, L.H., Olson, R., Hollinger, D., Running, S., Anthoni, P., Bernhofer, C., Davis, K., Evans, R., Fuentes, J., Goldstein, A., Katul, G., Law, B., Lee, X.H., Malhi, Y., Meyers, T., Munger, W., Oechel, W., U, K.T.P., Pilegaard, K., Schmid, H.P., Valentini, R., Verma, S., Vesala, T., Wilson, K., Wofsy, S., 2001. FLUXNET: A new tool to study the temporal and spatial variability of ecosystem-scale carbon dioxide, water vapor, and energy flux densities. *Bulletin of the American Meteorological Society* 82, 2415-2434.
- Baldocchi, D.D., 2003. Assessing the eddy covariance technique for evaluating carbon dioxide exchange rates of ecosystems: past, present and future. *Glob. Change Biol.* 9, 479-492.
- Bastiaanssen, W.G.M., Menenti, M., Feddes, R.A., Holtslag, A.A.M., 1998. A remote sensing surface energy balance algorithm for land (SEBAL). 1. Formulation. *Journal of Hydrology* 37(4), 439-451.
- Berk, A., Bernstein, L.S., Anderson, G.P., Acharya, P.K., Robertson, D.C., Chetwynd, J.H., Adler-Golden, S.M., 1998. MODTRAN cloud and multiple scattering upgrades with application to AVIRIS. *Remote Sens. Environ.* 65, 367-375.
- Bhumralkar, C.M., 1975. Numerical Experiments on computation of ground surface-Temperature in An Atmospheric General Circulation Model. *Journal of Applied Meteorology* 14, 1246-1258.

- Bosveld, F., Holtslag, A.A.M., Van den Hurk, B., 1999. Interpretation of crown radiation temperatures of a dense douglas fir forest with similarity theory. *Bound.-Layer Meteor.* 92, 429-451.
- Bréon, F.-M., Maignan, F., Leroy, M., Grant, I., 2002. Analysis of hot spot directional signatures measured from space. *Journal of Geophysical Research* 107, .
- Brunsell, N.A., Gillies, R.R., 2003. Scale issues in land-atmosphere interactions: implications for remote sensing of the surface energy balance. *Agric. For. Meteorol.* 117, 203-221.
- Brutsaert, W., 1999. Aspects of Bulk Atmospheric Boundary Layer Similarity Under Free-Convective Conditions. *Rev. Geophys.* 37.
- Brutsaert, W., 2009. *Hydrology, an Introduction*. Cambridge University Press, Cambridge, UK.
- Buschmann, C., 2007. Variability and application of the chlorophyll fluorescence emission ratio red/far-red of leaves. *Photosynth. Res.* 92, 261-271.
- Campbell, P.K.E., Middleton, E.M., Corp, L.A., Kim, M.S., 2008. Contribution of chlorophyll fluorescence to the apparent vegetation reflectance. *Sci. Total Environ.* 404, 433-439.
- Carter, G.A., Knapp, A.K., 2001. Leaf optical properties in higher plants: Linking spectral characteristics to stress and chlorophyll concentration. *Am. J. Bot.* 88, 677-684.
- Choudhury, B.J., 2000. Seasonal and interannual variations of total evaporation and their relations with precipitation, net radiation, and net carbon accumulation for the Gediz basin area. *Journal of Hydrology* 229, 77-86.
- Collatz, G.J., Ribas-Carbo, M., Berry, J.A., 1992. Coupled Photosynthesis Stomatal Conductance Model for Leaves of C4 plants. *Aust. J. Plant Physiol.* 19, 519-538.
- Combal, B., Baret, F., Weiss, M., Trubuil, A., Macé, D., Pragnère, A., Myneni, R.B., Knyazikhin, Y., Wang, L., 2002. Retrieval of Canopy biophysical variables from bidirectional reflectance using prior information to solve the ill-posed inverse problem. *Remote Sensing of Environment* 84, 1-15.
- Cowan, I., 1977. Stomatal behaviour and environment. *Adv. Bot. Res.* 4.
- D'Urso, G., Dini, L., Vuolo, F., Alonso, L., Guanter, L., 2004. Retrieval of Leaf area index by inverting hyper-spectral, multi-angular. CHRISPROBA Data from SPARC 2003. 2nd CHRIS/Proba Workshop,. ESA/ESRIN, Frascati, Italy.
- Destouni, G., Darracq, A., Jarsjö, J., Prieto, C., Shibuo, Y., 2009. Evapotranspiration in a warming climate. model uncertainty and role for climate adaptation. In: Publishing, I. (Ed.),

- Climate Change: Global Risks, Challenges and Decisions. IOP Publishing.
- Devices, A.S., 2000. FieldSpec Pro, User guide. Analytical Spectral Devices (ASD) Inc. Boulder, USA.
- Disney, M., Lewis, P., Saich, P., 2006. 3D modelling of forest canopy structure for remote sensing simulations in the optical and microwave domains. *Remote Sens. Environ.* 100, 114-132.
- Easterling, D.R., Meehl, G.A., Parmesan, C., Changnon, S.A., Karl, T.R., Mearns, L.O., 2000. Climate extremes: Observations, modeling, and impacts. *Science* 289, 2068-2074.
- Entekhabi, D., Asrar, G.R., Betts, A.K., Beven, K.J., Bras, R.L., Duffy, C.J., Dunne, T., Koster, R.D., Lettenmaier, D.P., McLaughlin, D.B., Shuttleworth, W.J., van Genuchten, M.T., Wei, M.-Y., Wood, E.F., 1999. An Agenda for Land Surface Hydrology Research and a Call for the Second International Hydrological Decade. *Bulletin of the American Meteorological Society* 80, 2043-2058.
- Farah, H.O., Bastiaanssen, W.G.M., Feddes, R.A., 2004. Evaluation of the temporal variability of the evaporative fraction in a tropical watershed. *International Journal of Applied Earth Observation and Geoinformation* 5, 129-140.
- Farquhar, G.D., Caemmerer, S., Berry, J.A., 1980. A biochemical model of photosynthetic CO₂ assimilation in leaves of C₃ species. *Planta* 149, 78-90.
- Fox, J., 1997. Applied regression analysis, linear models and related methods. Sage Publications, Teller Road, Thousand Oaks, California.
- Gascon, F., Gastellu-Etchegorry, J.P., Lefevre, M.J., 2001. Radiative transfer model for simulating high-resolution satellite images. *IEEE Trans. Geosci. Remote Sensing* 39, 1922-1926.
- Gastellu-Etchegorry, J.P., 2008. 3D modeling of satellite spectral images, radiation budget and energy budget of urban landscapes. *Meteorology and Atmospheric Physics* 102, 187-207.
- Gastellu-Etchegorry, J.P., Gascon, F., Esteve, P., 2003. An interpolation procedure for generalizing a look-up table inversion method. *Remote Sens. Environ.* 87, 55-71.
- Gastellu-Etchegorry, J.P., Martin, E., Gascon, F., 2004. DART: a 3D model for simulating satellite images and studying surface radiation budget. *Int. J. Remote Sens.* 25, 73-96.
- Gastellu-Etchegorry, J.P., Demarez, V., Pinel, V., Zagolski, F., 1996. Modeling radiative transfer in heterogeneous 3-D vegetation canopies. *Remote Sens. Environ.* 58, 131-156.

- Gerstl, S.A.W., 1990. Physics concepts of optical and radar reflectance signatures A summary review. *Int. J. Remote Sens.* 11, 1109-1117.
- Gillespie, A., Rokugawa, S., Matsunaga, T., Cothorn, J.S., Hook, S., Kahle, A.B., 1998. A temperature and emissivity separation algorithm for Advanced Spaceborne Thermal Emission and Reflection Radiometer (ASTER) images. *IEEE Trans. Geosci. Remote Sensing* 36, 1113-1126.
- Giorgi, F., Avissar, R., 1997. Representation of heterogeneity effects in earth system modeling: Experience from land surface modeling. *Rev. Geophys.* 35, 413-437.
- Gitelson, A.A., Wardlow, B.D., Keydan, G.P., Leavitt, B., 2007. An evaluation of MODIS 250-m data for green LAI estimation in crops. *Geophys. Res. Lett.* 34.
- Glenn, E.P., Huete, A.R., Nagler, P.L., Hirschboeck, K.K., Brown, P., 2007. Integrating remote sensing and ground methods to estimate evapotranspiration. *Critical Reviews in Plant Sciences* 26, 139-168.
- Gobron, N., Pinty, B., Verstraete, M.M., Martonchik, J.V., Knyazikhin, Y., Diner, D.J., 2000. Potential of multiangular spectral measurements to characterize land surfaces: Conceptual approach and exploratory application. *J. Geophys. Res.-Atmos.* 105, 17539-17549.
- Gorte, B., Pfeifer, N., 2004. Structuring Laser-Scanned Trees Using 3D Mathematical Morphology. *INTERNATIONAL ARCHIVES OF PHOTOGRAMMETRY REMOTE SENSING AND SPATIAL INFORMATION SCIENCES* 35, 929-933.
- Gowda, P.H., Chavez, J.L., Colaizzi, P.D., Evett, S.R., Howell, T.A., Tolk, J.A., 2007. Remote sensing based energy balance algorithms for mapping ET: Current status and future challenges. *Transactions of the Asabe* 50, 1639-1644.
- Hall, F.G., Huemmrich, K.F., Goetz, S.J., Sellers, P.J., Nickeson, J.E., 1992. Satellite Remote Sensing of Surface Energy Balance - Success, Failures and Unresolved Issues in FIFE. *J. Geophys. Res.-Atmos.* 97, 19061-19089.
- Hapke, B., 1981. Bidirectional Reflectance Spectroscopy 1. Theory. *J. Geophys. Res.* 86, 3039-3054.
- Hartogensis, O., 2006. Exploring Scintillometry in the Stable Atmospheric Surface Layer. *Meteorologie en Luchtkwaliteit. Wageningen Universiteit, Wageningen*, p. 240.
- Jacobs, A.F.G., Halbersma, J., Przybula, C., 1989. Behaviour of crop resistance of maize during a growing season. Estimation of Areal Evapotranspiration. *IAHS, Vancouver, Canada*, pp. 165-175.

- Jacquemoud, S., Bacour, C., Poilve, H., Frangi, J.P., 2000. Comparison of four radiative transfer models to simulate plant canopies reflectance: Direct and inverse mode. *Remote Sens. Environ.* 74, 471-481.
- Jacquemoud, S., Baret, F., 1990. PROSPECT - A Model of Leaf Optical Properties Spectra. *Remote Sens. Environ.* 34, 75-91.
- Jacquemoud, S., Ustin, S.L., Verdebout, J., Schmuck, G., Andreoli, G., Hosgood, B., 1996. Estimating leaf biochemistry using the PROSPECT leaf optical properties model. *Remote Sens. Environ.* 56, 194-202.
- Jacquemoud, S., Verhoef, W., Baret, F., Bacour, C., Zarco-Tejada, P.J., Asner, G.P., Francois, C., Ustin, S.L., 2009. PROSPECT plus SAIL models: A review of use for vegetation characterization. *Remote Sens. Environ.* 113, S56-S66.
- Jia, L., 2004. Modeling heat exchanges at the land-atmosphere interface using multi-angular thermal infrared measurements. Wageningen University, Wageningen, p. 199.
- Jia, L., Li, Z.L., Menenti, M., Su, Z., Verhoef, W., Wan, Z., 2003a. A practical algorithm to infer soil and foliage component temperatures from bi-angular ATSR-2 data. *Int. J. Remote Sens.* 24, 4739-4760.
- Jia, L., Menenti, M., Nerry, F., Najjar, G., Stoll, M.P., Su, Z., 2001. Evaluation of the Surface Energy Balance Index with the field and airborne data collected at Hartheim and Colmar. DAISEX final results Workshop. ESA/ESTEC, ESTEC, Noordwijk, the Netherlands.
- Jia, L., Su, Z.B., van den Hurk, B., Menenti, M., Moene, A., De Bruin, H.A.R., Yrisarry, J.J.B., Ibanez, M., Cuesta, A., 2003b. Estimation of sensible heat flux using the Surface Energy Balance System (SEBS) and ATSR measurements. *Phys. Chem. Earth* 28, 75-88.
- Jimenez-Munoz, J.C., Sobrino, J.A., Gillespie, A., Sabol, D., Gustafson, W.T., 2006. Improved land surface emissivities over agricultural areas using ASTER NDVI. *Remote Sens. Environ.* 103, 474-487.
- Kalma, J.D., McVicar, T.R., McCabe, M.F., 2008. Estimating Land Surface Evaporation: A Review of Methods Using Remotely Sensed Surface Temperature Data. *Surveys in Geophysics* 29, 421-469.
- Kimes, D.S., Knyazikhin, Y., Privette, J.L., AbuelGasim, A.A., Gao, F., 2000. Inversion Methods for Physically-Based Models. *Remote Sensing Reviews* 18, 381-439.
- Király, G., Brolly, G., 2007. Tree height estimation for terrestrial laser scanning in a forest reserve. *IAPRS*, pp. 211-215.

- Knyazikhin, Y., Martonchik, J.V., Diner, D.J., Myneni, R.B., Verstraete, M., Pinty, B., Gobron, N., 1998a. Estimation of vegetation canopy leaf area index and fraction of absorbed photosynthetically active radiation from atmosphere-corrected MISR data. *J. Geophys. Res.-Atmos.* 103, 32239-32256.
- Knyazikhin, Y., Martonchik, J.V., Myneni, R.B., Diner, D.J., Running, S.W., 1998b. Synergistic algorithm for estimating vegetation canopy leaf area index and fraction of absorbed photosynthetically active radiation from MODIS and MISR data. *J. Geophys. Res.-Atmos.* 103, 32257-32275.
- Koster, R.D., Suarez, M.J., Heiser, M., 2000. Variance and Predictability of Precipitation at Seasonal-to-Interannual Timescales. *J. Hydrometeorology* 1, 26-46.
- Kustas, W., Anderson, M., Norman, J., Li, F., 2007. Utility of Radiometric-aerodynamic Temperature Relations for Heat Flux Estimation. *Bound.-Layer Meteor.* 122, 167-187.
- Kustas, W.P., Daughtry, C.S.T., 1989. Estimation of the soil heat flux/net radiation ratio from spectral data. *Agric. For. Meteorol.* 49, 205-223.
- Kustas, W.P., Norman, J.M., 1999. Evaluation of soil and vegetation heat flux predictions using a simple two-source model with radiometric temperatures for partial canopy cover. *Agric. For. Meteorol.* 94, 13-29.
- Kustas, W.P., Norman, J.M., 2000. A Two-Source Energy Balance Approach Using Directional Radiometric Temperature Observations for Sparse Canopy Covered Surfaces. *Agron J* 92, 847-854.
- Kustas, W.P., Norman, J.M., Anderson, M.C., French, A.N., 2003. Estimating subpixel surface temperatures and energy fluxes from the vegetation index-radiometric temperature relationship. *Remote Sens. Environ.* 85, 429-440.
- Kuusik, A., 1991. Determination of vegetation canopy parameters from optical measurements. *Remote Sens. Environ.* 37, 207-218.
- Kuusik, A., 1998. Monitoring of vegetation parameters on large areas by the inversion of a canopy reflectance model. *Int. J. Remote Sens.* 19, 2893-2905.
- Legrand, M., Pietras, C., Brogniez, G., Haeffelin, M., Abuhassan, N.K., Sicard, M., 2000. A high-accuracy multiwavelength radiometer for in situ measurements in the thermal infrared. Part I: Characterization of the instrument. *J. Atmos. Ocean. Technol.* 17, 1203-1214.

- Leinonen, I., Jones, H.G., 2004. Combining thermal and visible imagery for estimating canopy temperature and identifying plant stress. *Journal of Experimental Botany* 55, 1423-1431.
- Leuning, R., 1995. A critical appraisal of a combined stomatal-photosynthesis model for C3 plants. *Plant, Cell and Environment* 18, 339-355.
- Li, S., Kang, S., Li, F., Zhang, L., Zhang, B., 2008. Vineyard evaporative fraction based on eddy covariance in an arid desert region of Northwest China. *Agricultural Water Management* 95, 937-948.
- Li, Z.L., Zhang, R., Sun, X., Su, H., Tang, X., Zhu, Z., Sobrino, J.A., 2004. Experimental system for the study of the directional thermal emission of natural surfaces. *Int. J. Remote Sens.* 25, 195-204.
- Liang, S., 2003. *Quantitative Remote Sensing of Land Surfaces*. Wiley-Interscience.
- Liang, S., Strahler, A.H., Barnsley, M.J., Borel, C.C., Gerstl, S.A.W., Diner, D.J., Prata, A.J., Walthall, C.L., 2000. Multiangle remote sensing: Past, present and future. *Remote Sensing Reviews* 18, 83 - 102.
- Lindenmayer, A., 1968. Mathematical Models For Cellular Interactions In Development .I. Filaments With 1-Sided Inputs. *Journal of Theoretical Biology* 18, 280-&.
- Liu, Q.H., Huang, H.G., Qin, W.H., Fu, K.H., Li, X.W., 2007a. An extended 3-D radiosity-graphics combined model for studying thermal-emission directionality of crop canopy. *IEEE Trans. Geosci. Remote Sensing* 45, 2900-2918.
- Liu, S., Lu, L., Mao, D., Jia, L., 2007b. Evaluating parameterizations of aerodynamic resistance to heat transfer using field measurements. *Hydrol. Earth. Syst. Sci.* 11, 769-783.
- Lu, X.L., Zhuang, Q.L., 2010. Evaluating evapotranspiration and water-use efficiency of terrestrial ecosystems in the conterminous United States using MODIS and AmeriFlux data. *Remote Sens. Environ.* 114, 1924-1939.
- Malenovsky, Z., Martin, E., Homolova, L., Gastellu-Etchegorry, J.P., Zurita-Milla, R., Schaepman, M.E., Pokorny, R., Clevers, J., Cudlin, P., 2008. Influence of woody elements of a Norway spruce canopy on nadir reflectance simulated by the DART model at very high spatial resolution. *Remote Sens. Environ.* 112, 1-18.
- Martonchik, J.V., Bruegge, C.J., Strahler, A.H., 2000. A review of reflectance nomenclature used in remote sensing. *Remote sens. Rev.* 19, 9-20.

- Massman, W.J., 1999. A model study of kBH-1 for vegetated surfaces using 'localized near-field' Lagrangian theory. *Journal of Hydrology* 223, 27-43.
- McCabe, M.F., Balick, L.K., Theiler, J., Gillespie, A.R., Mushkin, A., 2008. Linear mixing in thermal infrared temperature retrieval. *Int. J. Remote Sens.* 29, 5047-5061.
- McCabe, M.F., Wood, E.F., 2006. Scale influences on the remote estimation of evapotranspiration using multiple satellite sensors. *Remote Sens. Environ.* 105, 271-285.
- McNaughton, K.G., van den Hurk, B.J.J.M., 1995. A 'LAGRANGIAN' REVISION OF THE RESISTORS IN THE TWO-LAYER MODEL FOR CALCULATING THE ENERGY BUDGET OF A PLANT CANOPY. *Bound.-Layer Meteor.* 74, 261-288.
- Menenti, M., Jia, L., Li, Z.-L., 2008. Multi-angular Thermal Infrared Observations of Terrestrial Vegetation. pp. 51-93.
- Meroni, M., Colombo, R., Panigada, C., 2004. Inversion of a radiative transfer model with hyperspectral observations for LAI mapping in poplar plantations. *Remote Sens. Environ.* 92, 195-206.
- Miller, J., Berger, M., Goulas, Y., Jacquemoud, S., Louis, J., Mohamed, G., Moise, N., Moreno, J., Moya, I., Pedrós, R., Verhoef, W., Zarco-Tejada, P.J., 2005. Development of a Vegetation Fluorescence Canopy Model. *ESTEC*, p. 138.
- Milton, E.J., Schaepman, M.E., Anderson, K., Kneubuhler, M., Fox, N., 2009. Progress in field spectroscopy. *Remote Sens. Environ.* 113, S92-S109.
- Monin, A.S., Obukhov, A.M., 1954. Osnovnye zakonomernosti turbulentnogo peremesivaniya v prizemnom sloe atmosfery. *Trudy geofiz. inst. AN SSSR* 24 (151), 163-187.
- Monteith, J.L., 1973. *Principles of environmental physics*. Edward Arnold Press.
- Moré, J.J., Wright, S.J., 1993. *Optimization software guide*. Society for Industrial and Applied Mathematics (SIAM), Philadelphia.
- Naesset, E., 1997. Determination of mean tree height of forest stands using airborne laser scanner data. *ISPRS-J. Photogramm. Remote Sens.* 52, 49-56.
- Nikolov, N., Zeller, K., 2006. Efficient retrieval of vegetation leaf area index and canopy clumping factor from satellite data to support pollutant deposition assessments. *Environmental Pollution* 141, 539-549.
- Norman, J.M., 1979. Modeling the complete crop canopy. In: Barfield, B.J., Gerber, J.F. (Eds.), *Modification of the aerial environment of plants*. ASAE Monogr. Am. Soc. Agric. Eng., St. Joseph, MI., pp. 249-277.

- Norman, J.M., Becker, F., 1995. Terminology in thermal infrared Remote Sensing of Natural Surfaces. *Agric. For. Meteorol.* 77, 153-166.
- Norman, J.M., Kustas, W.P., Humes, K.S., 1995. SOURCE APPROACH FOR ESTIMATING SOIL AND VEGETATION ENERGY FLUXES IN OBSERVATIONS OF DIRECTIONAL RADIOMETRIC SURFACE-TEMPERATURE. *Agric. For. Meteorol.* 77, 263-293.
- North, P.R.J., 2002. Estimation of Aerosol opacity and land surface bidirectional reflectance from ATSR-2 dual angle imagery: operational method and validation. *Journal of Geophysical Research* 107.
- Obukhov, A.M., 1971. Turbulence in an atmosphere with a non-uniform temperature. *Bound.-Layer Meteor.* 2, 7-29.
- Olioso, A., Chauki, H., Wigneron, J., Bergaoui, K., Bertuzzi, P., Chanzy, A., Bessemoulin, P., Clavet, J.C., 1999. Estimation of energy fluxes from thermal infrared, spectral reflectances, microwave data and SVAT modeling. *Physics and Chemistry of the Earth, Part B: Hydrology, Oceans and Atmosphere* 24, 829-836.
- Oude Elberink, S., Vosselman, G., 2006. 3D Modeling of Topographic Objects by Fusing 2D Maps and Lidar Data. *International Archives of Photogrammetry Remote Sensing and Spatial Information Sciences* 36, on CDROM.
- Pauwels, V.R.N., Samson, R., 2006. Comparison of different methods to measure and model actual evapotranspiration rates for a wet sloping grassland. *Agricultural Water Management* 82, 1-24.
- Pauwels, V.R.N., Timmermans, W., Loew, A., 2008. Comparison of the estimated water and energy budgets of a large winter wheat field during AgriSAR 2006 by multiple sensors and models. *Journal of Hydrology* 349, 425-440.
- Payan, V., Royer, A., 2004. Analysis of Temperature Emissivity Separation (TES) algorithm applicability and sensitivity. *Int. J. Remote Sens.* 25, 15-37.
- Perez-Gutierrez, C., Martinez-Fernandez, J., Sanchez, N., Alvarez-Mozos, J., 2007. Modeling of soil roughness using terrestrial laser scanner for soil moisture retrieval. *International Geoscience and Remote Sensing Symposium, IGARRS. IEEE*, pp. 1877 – 1880.
- Pfeifer, N., Briese, C., 2007. Geometrical aspects of Airborne Laser Scanning and Terrestrial Laser Scanning. *IAPRS* pp. 311-319.
- Pfeifer, N., Gorte, B., D., W., 2004. Automatic reconstruction of single trees from terrestrial laser scanner data. *ISPRS XXth Congress, Istanbul, Turkey*, pp. 1-6.
- Picton, P., 2000. *Neural Networks*. Palgrave, New York.

- Pielke, S.R.A., 2001. Influence of the spatial distribution of vegetation and soil on the prediction at seasonal to interannual timescale. *J. Hydrometeorology* 1, 26-46.
- Pinty, B., Gobron, N., Widlowski, J.L., Gerstl, S.A.W., Verstraete, M.M., Antunes, M., Bacour, C., Gascon, F., Gastellu, J.P., Goel, N., Jacquemoud, S., North, P., Qin, W.H., Thompson, R., 2001. The Radiation transfer model intercomparison (RAMI) exercise. *J. Geophys. Res.-Atmos.* 106, 11937-11956.
- Pinty, B., Widlowski, J.L., Taberner, M., Gobron, N., Verstraete, M.M., Disney, M., Gascon, F., Gastellu, J.P., Jiang, L., Kuusk, A., Lewis, P., Li, X., Ni-Meister, W., Nilson, T., North, P., Qin, W., Su, L., Tang, S., Thompson, R., Verhoef, W., Wang, H., Wang, J., Yan, G., Zang, H., 2004. Radiation Transfer Model Intercomparison (RAMI) exercise: Results from the second phase. *J. Geophys. Res.-Atmos.* 109.
- Prata, A.J.F., Cechet, R.P., Barton, I.J., Llewellynjones, D.T., 1990. THE ALONG TRACK SCANNING RADIOMETER FOR ERS-1 - SCAN GEOMETRY AND DATA SIMULATION. *IEEE Trans. Geosci. Remote Sensing* 28, 3-13.
- Press, W.H., Flannery, B.P., Teukolsky, S.A., Vetterling, W.T., 2007. *Numerical Recipes in C*. University Press, Cambridge.
- Qin, W., Liang, S., 2000. Plane-parallel canopy radiation transfer modeling: Recent advances and future directions. *Remote Sensing Reviews* 18, 281-305.
- Rascher, U., Gioli, B., Miglietta, F., 2008. FLEX — Fluorescence Explorer: A Remote Sensing Approach to Quantify Spatio-Temporal Variations of Photosynthetic Efficiency from Space. . In: Allen, J.F., Gantt, E., Golbeck, J.H., Osmond, B. (Eds.), *Photosynthesis. Energy from the Sun*, 14th International Congress on Photosynthesis. Springer, Netherlands.
- Rautiainen, M., 2005. Retrieval of leaf area index for a coniferous forest by inverting a forest reflectance model. *Remote Sens. Environ.* 99, 295-303.
- Rauwerda, J., Roerink, G.J., Su, Z., 2002. Estimation of evaporative fractions by the use of vegetation and soil component temperatures determined by means of dual-looking remote sensing. *Alterra, Wageningen*, p. 149.
- Schneider, T., Zimmermann, S., Manakos, I., 2004. Field goniometer system for accompanying directional measurements. 2nd CHRIS/Proba Workshop. ESA/ESRIN, Frascati, Italy.
- Schopfer, J., Dangel, S., Kneubuhler, M., Itten, K.I., 2008. The improved dual-view field goniometer system FIGOS. *Sensors* 8, 5120-5140.

- Sellers, P.J., Dickinson, R.E., Randall, D.A., Betts, A.K., Hall, F.G., Berry, J.A., Collatz, G.J., Denning, A.S., Mooney, H.A., Nobre, C.A., Sato, N., Field, C.B., Henderson-Sellers, A., 1997. Modeling the Exchanges of Energy, Water, and Carbon Between Continents and the Atmosphere. *Science* 275, 502-509.
- Seneviratne, S.I., Stöckli, R., 2007. The Role of Land-Atmosphere Interactions for Climate Variability in Europe. pp. 179-193.
- Shan, X., van de Velde, R., Wen, J., He, Y., Verhoef, W., Su, Z., 2008. Regional Evapotranspiration over the arid inland heihe river basin in northwest China. *Dragon 1 Programme Final Results*. ESA, Beijing.
- Shimoda, S., Oikawa, T., 2006. Temporal and spatial variations of canopy temperature over a C3-C4 mixture grassland. *Hydrological Processes* 20, 12.
- Sobrino, J.A., Caselles, V., 1993. A Field Method for Measuring the Thermal Infrared Emissivity. *ISPRS-J. Photogramm. Remote Sens.* 48, 24-31.
- Sobrino, J.A., Jimenez-Munoz, J.C., 2005. Land surface temperature retrieval from thermal infrared data: An assessment in the context of the Surface Processes and Ecosystem Changes Through Response Analysis (SPECTRA) mission. *J. Geophys. Res.-Atmos.* 110.
- Sobrino, J.A., Jimenez-Munoz, J.C., Gomez, M., Barella-Ortiz, A., Soria, G., Julien, Y., Zaragoza-Ivora, M.M., Gómez, J.A., de Miguel, E., Jiménez, M., Su, Z., Timmermans, W.J. and ... [et al.] (2007) 2007 Application of high - resolution thermal infrared remote sensing to assess land surface temperature and emissivity in different natural environments. . In: Schaeppman, M.E. (Ed.), 10th international symposium on physical measurements and spectral signatures in remote sensing, *ISPMSRS'07*. International Society for Photogrammetry and Remote Sensing (ISPRS), Davos, Switzerland
- Sobrino, J.A., Li, Z.L., Stoll, M.P., Becker, F., 1994. IMPROVEMENTS IN THE SPLIT-WINDOW TECHNIQUE FOR LAND-SURFACE TEMPERATURE DETERMINATION. *IEEE Trans. Geosci. Remote Sensing* 32, 243-253.
- Sobrino, J.A., Romaguera, M., Sòria, G., Zaragoza, M.M., Gómez, M., Cuenca, J., Julien, Y., Jiménez-Muñoz, J.C., Su, Z., Jia, L., Gieske, A.S.M., Timmermans, W.J., Van der Kwast, H., Oliso, A., Nerry, F., Sabol, D., Moreno, J., 2005. Thermal Measurements in the framework of SPARC. *SPARC final workshop*. ESA, Enschede.

- Sobrino, J.A., Soria, G., Prata, A.J., 2004. Surface temperature retrieval from Along Track Scanning Radiometer 2 data: Algorithms and validation. *J. Geophys. Res.-Atmos.* 109.
- Strahler, A.H., 1997. Vegetation canopy reflectance modeling—recent developments and remote sensing perspectives. *Remote Sensing Reviews* 15, 179-194.
- Su, H., McCABE, M.F., Wood, E.F., 2005a. Modeling Evapotranspiration during SMACEX: Comparing Two Approaches for Local- and Regional-Scale Prediction. *JOURNAL OF HYDROMETEOROLOGY* 6, 910-922.
- Su, Z., 1996. Remote sensing applied to hydrology: the Sauer river Basin Study. Hydrology/ Wasserwirtschaft, Faculty of Civil Engineering. Ruhr University, Bochum.
- Su, Z., 2002. The Surface Energy Balance System (SEBS) for estimation of turbulent heat fluxes. *Hydrol. Earth Syst. Sci.* 6, 85-99.
- Su, Z., Jia, L., Gieske, A., Timmermans, W., Jin, X., Elbers, J.A., van der Kwast, H., Olioso, A., Sobrino, J.A., Nerry, F., Sabol, D., Moreno, J.F., 2005b. IN-SITU MEASUREMENTS OF LAND-ATMOSPHERE EXCHANGES OF WATER, ENERGY AND CARBON DIOXIDE IN SPACE AND TIME OVER THE HETEROGENEOUS BARRAX SITE DURING SPARC2004. In: ESA (Ed.), SPARC workshop ESA, Enschede, p. 8.
- Su, Z., Pelgrum, H., Menenti, M., 1999. Aggregation effects of surface heterogeneity in land surface processes. *Hydrol. Earth Syst. Sci.* 3, 549-563.
- Su, Z., Schmugge, T., Kustas, W.P., Massman, W.J., 2001. An evaluation of two models for estimation of the roughness height for heat transfer between the land surface and the atmosphere. *Journal of Applied Meteorology* 40, 1933-1951.
- Su, Z., Timmermans, W., Gieske, A., Jia, L., Elbers, J.A., Olioso, A., Timmermans, J., Van Der Velde, R., Jin, X., Van Der Kwast, H., Nerry, F., Sabol, D., Sobrino, J.A., Moreno, J., Bianchi, R., 2008. Quantification of land-atmosphere exchanges of water, energy and carbon dioxide in space and time over the heterogeneous Barrax site. *Int. J. Remote Sens.* 29, 5215-5235.
- Su, Z., Timmermans, W.J., van der Tol, C., Dost, R., Bianchi, R., Gomez, J.A., House, A., Hajnsek, I., Menenti, M., Magliulo, V., Esposito, M., Haarbrink, R., Bosveld, F., Rothe, R., Baltink, H.K., Vekerdy, Z., Sobrino, J.A., Timmermans, J., van Laake, P., Salama, S., van der Kwast, H., Claassen, E., Stolk, A., Jia, L., Moors, E., Hartogensis, O., Gillespie, A., 2009. EAGLE 2006-Multi-purpose, multi-angle and multi-

- sensor in-situ and airborne campaigns over grassland and forest. *Hydrol. Earth Syst. Sci.* 13, 833-845.
- Suits, G.W., 1972. The calculation of the directional reflectance of a vegetative canopy. *Remote Sens. Environ.* 2, 117-125.
- Tang, S., Chen, J.M., Zhu, Q., Li, X., Chen, M., Sun, R., Zhou, Y., Deng, F., Xie, D., 2007. LAI inversion algorithm based on directional reflectance kernels. *J. Environ. Manage.* 85, 638-648.
- Tarantola, A., 2005. *Inverse Problem Theory and Methods for Model Parameter Estimation.* Society of Industrial and Applied Mathematics (SIAM).
- Timmermans, J., Van Der Tol, C., Verhoef, W., Su, Z., 2008. Contact and directional radiative temperature measurements of sunlit and shaded land surface components during the SEN2FLEX 2005 campaign. *Int. J. Remote Sens.* 29, 5183-5192.
- Timmermans, J., van der Tol, C., Verhoef, A., Wang, L., van Helvoirt, M.D., Verhoef, W. and Su, Z. (2010) Quantifying the uncertainty in estimates of surface atmosphere fluxes by evaluation of sebs and scope models. , 2009. Quantifying the uncertainty in estimates of surface atmosphere fluxes by evaluation of sebs and scope models. In: *Proceedings of the symposium earth observation and water cycle science.* In: (ESA), H.L.-F.-N.E.S.A. (Ed.), *Proceedings of the symposium earth observation and water cycle science, Frascati, Italy*
- Timmermans, J., Verhoef, W., van der Tol, C., Su, Z., 2009. Retrieval of canopy component temperatures through Bayesian inversion of directional thermal measurements. *Hydrol. Earth Syst. Sci.* 13, 1249-1260.
- Timmermans, W.J., Kustas, W.P., Anderson, M.C., French, A.N., 2007. An intercomparison of the surface energy balance algorithm for land (SEBAL) and the two-source energy balance (TSEB) modeling schemes. *Remote Sens. Environ.* 108, 369-384.
- Timmermans, W.J., van der Kwast, J., Gieske, A.S.M., Su, Z., Olioso, A., Jia, L., Elbers, J.A., 2005. Intercomparison of Energy Flux Models using Aster Imagery at the SPARC 2004 site (Barrax, Spain). SPARC final workshop. ESA, Enschede.
- Tuzet, A., Perrier, A., Leuning, R., 2003. A coupled model of stomatal conductance, photosynthesis and transpiration. *Plant, Cell and Environment* 26, 1097-1116.
- van der Tol, C., van der Tol, S., Verhoef, A., Su, B., Timmermans, J., Houldcroft, C., Gieske, A., 2009a. A Bayesian approach to estimate sensible and latent heat over vegetated land surface. *Hydrol. Earth Syst. Sci.* 13, 749-758.

- van der Tol, C., Verhoef, W., Rosema, A., 2009b. A model for chlorophyll fluorescence and photosynthesis at leaf scale. *Agric. For. Meteorol.* 149, 96-105.
- van der Tol, C., Verhoef, W., Timmermans, J., Verhoef, A., Su, Z., 2009c. An integrated model of soil-canopy spectral radiances, photosynthesis, fluorescence, temperature and energy balance. *Biogeosciences* 6, 3109-3129.
- van Olden, A.P., Wiring, J., 1996. Atmospheric Boundary Layer Research at Cabauw. *Bound.-Layer Meteor.* 78, 39-69.
- Vekerdy, Z., van Laake, P.E., Timmermans, J., Dost, R.J.J., 2007. Canopy structural modeling based on laser scanning. AGRISAR and EAGLE campaigns, final workshop. ESA/ESTEC, Noordwijk, the Netherlands, p. 8.
- Verhoef, A., Allen, S.J., 2000. A SVAT scheme describing energy and CO₂ fluxes for multi-component vegetation: calibration and test for a Sahelian savannah. *Ecological Modelling* 127, 245-267.
- Verhoef, A., McNaughton, K.G., Jacobs, A.F.G., 1999. A parameterization of momentum roughness length and displacement height for a wide range of canopy densities. *Hydrol. Earth Syst. Sci.* 1, 81-91.
- Verhoef, W., 1984. Light Scattering by Leaf Layers with Application to Canopy Reflectance Modeling: The SAIL Model. *Remote Sens. Environ.* 16, 16.
- Verhoef, W., 2000. Simultaneous retrieval of soil, leaf, canopy and atmospheric parameters from hyperspectral information in the red edge through model inversion. National Aerospace Laboratory (NLR).
- Verhoef, W., 2007. A Bayesian optimisation approach for model inversion of hyperspectral - multidirectional observations : the balance with A Priori information. In: Schaeppman, M.E. (Ed.), 10th international symposium on physical measurements and spectral signatures in remote sensing. ISPRS, Davos, Switzerland, pp. 208-213.
- Verhoef, W., 2008. A Bayesian optimisation approach for model inversion of hyperspectral - multidirectional observations : the balance with A Priori information. In: Schaeppman, M.E. (Ed.), 10th international symposium on physical measurements and spectral signatures in remote sensing. ISPRS, Davos, Switzerland, pp. 208-213.
- Verhoef, W., Bach, H., 2003. Simulation of hyperspectral and directional radiance images using coupled biophysical and atmospheric radiative transfer models. *Remote Sens. Environ.* 87, 23-41.

- Verhoef, W., Bach, H., 2007. Coupled soil-leaf-canopy and atmosphere radiative transfer modeling to simulate hyperspectral multi-angular surface reflectance and TOA radiance data. *Remote Sens. Environ.* 109, 166-182.
- Verhoef, W., Jia, L., Xiao, Q., Su, Z., 2007. Unified optical-thermal four-stream radiative transfer theory for homogeneous vegetation canopies. *IEEE Trans. Geosci. Remote Sensing* 45, 1808-1822.
- Wallace, J.S., Verhoef, A., 2000. Modelling interactions in mixed plant communities: light, water and carbon dioxide. In: Marshall, B., Roberts, J.A. (Eds.), *Leaf Development and Canopy growth*. Sheffield Academic Press, UK.
- Wang, J., Li, X., Sun, X., Liu, Q., 2000. Component temperatures inversion for remote sensing pixel based on directional thermal radiation model. *Science in China Series E: Technological Sciences* 43, 41-47.
- Wehr, A., 2008. LIDAR: Airborne and terrestrial sensors. In: Li, C.a.B. (Ed.), *Advances in Photogrammetry, Remote Sensing and Spatial Information Sciences*. ISPRS, London, pp. 73-84.
- Wetzel, P.J., Chang, J.-T., 1988. Evapotranspiration from Nonuniform Surfaces: A First Approach for Short-Term Numerical Weather Prediction. *Monthly Weather Review* 116, 600-621.
- Widlowski, J.L., 2001. EXTRACTING QUANTITATIVE SUB_PIXEL HETEROGENEITY INFORMATION FROM OPTICAL REMOTE SENSING DATA. Faculty of Sciences. University of Fribourg, Fribourg, p. 173.
- Widlowski, J.L., Taberner, M., Pinty, B., Bruniquel-Pinel, V., Disney, M., Fernandes, R., Gastellu-Etchegorry, J.P., Gobron, N., Kuusk, A., Lavergne, T., Leblanc, S., Lewis, P.E., Martin, E., Mottus, M., North, P.R.J., Qin, W., Robustelli, M., Rochdi, N., Ruiloba, R., Soler, C., Thompson, R., Verhoef, W., Verstraete, M.M., Xie, D., 2007. Third Radiation Transfer Model Intercomparison (RAMI) exercise: Documenting progress in canopy reflectance models. *J. Geophys. Res.-Atmos.* 112.
- Yamaguchi, Y., Kahle, A.B., Tsu, H., Kawakami, T., Pniel, M., 1998. Overview of Advanced Spaceborne Thermal Emission and Reflection Radiometer (ASTER). *IEEE Trans. Geosci. Remote Sensing* 36, 1062-1071.
- Yan, G.J., Friedl, M., Li, X.W., Wang, J.D., Zhu, C.G., Strahler, A.H., 2001. Modeling directional effects from nonisothermal land surfaces in wideband thermal infrared measurements. *IEEE Trans. Geosci. Remote Sensing* 39, 1095-1099.

Bibliography

Yin, X., van Laar, H.H., 2005. Crop Systems Dynamics: An Ecophysiological Model of Genotype-by-Environment Interactions (GECROS); . Wageningen.

10 Summary

In this dissertation I have investigated the potential of using optical and thermal multi-directional remote sensing observations to estimate biophysical processes. Monitoring the processes within the earth's biosphere is extremely important. Remote sensing is probably the only tool for monitoring such processes at regional to continental scale. Presently several initiatives exist to estimate evapotranspiration and photosynthesis using remote sensing algorithms. Most of these algorithms have not been developed recently, and may already exist for some years. This has the advantage that these algorithms have been tested and validated in several ways during the past couple of years. However, using older models also limits the potential of using new innovative approaches in satellite sensors.

In the last few years the quality, availability and innovations of remote sensing sensors have increased remarkably. Remote sensing products can now be produced with higher spatial, temporal, and spectral resolutions than previously thought possible. All these innovations offer the possibility to estimate biophysical processes at higher accuracies. In addition, some of these new satellite sensors even offer the option of acquiring observations from different viewing directions.

Even though new satellite sensors have an increased spatial resolution, pixel resolutions are still several orders above that of individual canopy components. The radiation observed by the satellite sensor is therefore an aggregate of the (reflected / thermal emitted) radiation by these components. This aggregate depends on the structure of the canopy, the spectral characteristics of the components, and the observation/solar angles. Consequently this aggregate will have an angular signature, such as the bidirectional reflectance factor, which may be measured. Knowledge about sub-pixel processes can therefore be obtained on the basis of these angular signatures. Radiative transfer models are required to characterise the behaviour of an angular signature on the basis of different canopy parameters. Because current remote sensing algorithms do not employ complex radiative transfer models, they are not yet suited to making use of multi-directional observations.

In this dissertation a model is presented, which is able to simulate the biophysical processes, the radiative transfer within the canopy and the outgoing hyperspectral optical and thermal radiances in

Summary

parallel. This Soil Canopy Observation of Photochemistry and Energy fluxes (SCOPE) model combines a discrete version of the Scattering by Arbitrary Inclined Leaves (SAIL) 1D radiative transfer model, with a photosynthesis model, and an evaporation/transpiration model. The coupling of radiative transfer model with the biophysical process model is performed using the skin temperatures of four different canopy components, which are vertically distributed in the canopy. The fluxes are then calculated iteratively by solving an energy balance approach which integrated the emitted fluxes of sunlit and shaded leaves for all layers.

Identification of the components was based on the radiative and contact measurements of different vegetation types, i.e. short and tall grass, young and mature maize, wheat, barley and vineyard. Based on the directional radiative signatures the most complex vegetation type was found to be vineyard. In this crop the most important components were sunlit soil, shaded soil, sunlit leaves and shaded leaves. Vertical variation of these temperatures was of a lower order than the differences between the individual temperatures.

The radiative transfer part of the model was evaluated by comparing it to more complex radiative transfer models. Validation of the other sub models was not performed in this research. First a comparison was made between the Soil Leaf Canopy (SLC) 1D radiative transfer model and SCOPE. The SCOPE and SLC both have evolved from the SAIL radiative transfer model. However, SLC provides an analytical solution to the radiative transfer problem while SCOPE solves it numerically, in order to estimate leaf temperatures at different vertical positions within the canopy. The SLC model is also capable of simulating crown clumping effects within the canopy. The comparison between SCOPE and SLC showed that in SCOPE the finite size of the layers caused large errors for large oblique viewing angles. A modification was made to the SCOPE model, which solved this problem.

A second comparison was performed between SCOPE and the very complex Discrete Anisotropic Radiative Transfer (DART) 3D radiative transfer model. Several scenarios were simulated by the DART model with increasing structural complexity. The input data required by DART were obtained through a terrestrial laser scan of the Speulderbos forested area. To provide these input data for DART several 3D filter operations were performed on the point cloud data of this laser scan. The SCOPE DART comparison showed a good agreement between the two models for all scenarios but the ones with more extreme clumping. While for higher clumping (lower crown

coverage) the SCOPE model failed to approximate the DART results the correctly, the SLC model was able to simulate bidirectional reflectance factors more in agreement with DART. Only when the crown cover was so low that the DART BRDF started to have solar azimuth angle dependencies, the SLC model could not reproduce this artefact of DART.

After the validation, the SCOPE model was used to estimate the skin temperatures of the different canopy components. For this a sensor simulator was created to convert SCOPE top-of-canopy radiances into sensor observations. A sensitivity analysis proved that single-view (nadir) observations could not be used to estimate the skin temperatures of the different components; instead multi-directional observations were required. Using these simulated multi-directional observations, the skin temperatures of all four components could be retrieved successfully. Application of this algorithm with the multi-directional radiative field measurements also provided good results.

Finally, SCOPE was used to evaluate the Surface Energy Balance System (SEBS) remote sensing algorithm over tall vegetation. SCOPE was used here both to provide reference estimations of the turbulent heat flux and to simulate sensor bands required by the SEBS pre-processor. Comparison showed that SEBS underestimated the evapotranspiration, because the parameterization of the roughness length for heat was not suitable for tall vegetation. A modification was incorporated in the SEBS model that solved this problem. In addition, the evaporative fractions of SEBS and SCOPE were examined. It was found that the evaporative fraction calculated by SCOPE increased over the course of a day. Consequently the values of the evaporative fraction estimated using remote sensing observations can vary depending on the overpass time. Fortunately, the largest variation occurs very early in the morning. It was found that the mean evaporative fraction estimated by SCOPE matched the evaporative fraction estimated by SEBS at overpass time (between 9 h00 and 12h00).

It was a good run!

11 Samenvatting

In deze dissertatie heb ik het potentieel van het gebruik van meerdere observatie hoeken in optische en thermische aard observatie onderzocht. Het doel hierin was de accuratesse van het bepalen van biofysische processen, zoals verdamping, te verbeteren.

Het bepalen van deze processen is zeer belangrijk. Aard observatie is waarschijnlijk het enige hulpmiddel om zulke processen te in kaart te brengen op regionale en globale schaal. Op dit moment zijn er verschillende projecten bezig met het bepalen van verdamping en fotosynthese met behulp van aard observatie algoritmes. De meeste van deze algoritmes zijn echter gedateerd. Dit heeft zowel positieve en negatieve kanten. Aan de ene kant betekent dit dat deze algoritmes zeer goed getest en gevalideerd zijn; aan de andere kant betekent het ook dat de mogelijkheden die nieuwe satellieten bieden niet door deze algoritmes gebruikt kunnen worden.

Gedurende de laatste jaren is de kwaliteit, beschikbaarheid en mogelijkheden van aard observatie sensoren zeer sterk verbeterd. Satelliet beelden zijn nu beschikbaar op een hogere spatiale, temporale en spectrale resolutie die voorheen onmogelijk werden geacht. Een andere innovatie die nog in de kinderschoenen staat is het maken van satelliet beelden met verschillende observatie hoeken. Al van deze innovaties hebben de mogelijkheid om biofysische processen nog beter in kaart te brengen.

Ondanks de hierboven genoemde innovatie stappen in aard observatie is de spatiale resolutie van de satelliet sensors niet groot genoeg om individuele componenten van het gewas, zoals bladeren, waar te nemen. De straling die wordt waargenomen door de satelliet sensor is daardoor een mengsel van straling gereflecteerd door zon beschenen en beschaduwde bladeren/grond. De mate van samensmelting hangt af de structuur van het gewas, de spectrale eigenschappen van de verschillende componenten en de observatie/zonnen hoek. Hierdoor verschilt de gemeten straling door satelliet sensor per kijkhoek. Om dit te in kaart te brengen worden de hoekafhankelijkheid per gewas, zoals de bi-directionele reflectie factor (BRDF), gemeten. Processen die op bladniveau plaats vinden kunnen zo in kaart gebracht worden door multi-directionele metingen te koppelen aan zulke directionele signaturen.

Stralingsmodellen zijn vereist om het gedrag van zulke directionele signaturen om te zetten naar de eigenschappen van het gewas. Omdat de modellen die op dit moment gebruikt worden om

verdamping te bepalen in aard observatie deze stralingsmodellen niet gebruiken zijn ze niet geschikt om gebruik te maken van zulke directionele signaturen.

In deze dissertatie wordt een model gepresenteerd die tegelijkertijd de stralingsoverdracht binnen het gewas en de biofysische processen kan simuleren. Dit 'Soil Canopy Observation of Photochemistry and Energy fluxes' (SCOPE) model is een combinatie van biofysische (fotosynthese en verdamping) modellen en van het 'Scattering by Arbitrary Inclined Leaves' (SAIL) 1D stralingsmodel. De koppeling tussen het stralingsmodel en de biofysische modellen wordt gedaan op basis van de oppervlakte temperatuur van vier componenten in het gewas. De verdamping kan dan iteratief worden berekend door het oplossen van de energie balans over het gehele gewas.

Er is tijdens dit onderzoek onderzocht welke componenten in het gewas nu het meest representatief zijn. Dit is gedaan door verschillende gewassen te onderzoeken, namelijk: kort en lang gras, jong en volwassen mais, tarwe, graan, suikerbiet en wijngaard. In dit onderzoek bleek de wijngaard de meest complexe directionele signaturen te hebben. In dit gewas waren de meest belangrijke componenten: zon geschoten bladeren, beschaduwde bladeren, zon beschenen grond en beschaduwde grond. Verticale distributie van temperaturen was aanwezig maar de variatie hierin was veel minder.

Het stralingsmodel in het SCOPE model is geëvalueerd tegen complexe stralingsmodellen. Eerst werd de het stralingsmodel vergeleken met het 'Soil Leaf Canopy' (SLC) 1D model. Zowel SLC als het stralingsmodel in SCOPE zijn gebaseerd op het SAIL stralingsmodel. Echter is SLC over de jaren meer complex geworden dan de originele SAIL model, onder andere door het toevoegen van clumping (clustering) van het gewas. SCOPE bevat deze clumping parameterizatie niet, maar heeft als voordeel boven SLC dat het thermische straling meeneemt in haar simulaties, welke belangrijk zijn om biofysische processen te modelleren. Tijdens de vergelijking tussen SLC en SCOPE bleek dat in SCOPE niet rekening werd gehouden met de dikte van de lagen binnenin het model. Na aanpassing van het SCOPE model blijken beide modellen goed te vergelijken voor simpele gewassen.

Het SCOPE model is daarna vergeleken met het zeer complexe Discrete Anisotropic Radiative Transfer (DART) 3D stralingsmodel. In dit gedeelte van mijn onderzoek zijn verschillende scenario's, met toenemende complexiteit, naast elkaar vergeleken. Deze scenario's zijn met DART gemaakt op basis van data die was verkregen door

gebruik te maken van 3D grond laser metingen van het Speulderbos. De vergelijking tussen SCOPE en DART toonde goede overeenkomst tussen de twee modellen voor alle scenario's behalve voor de scenario met extreme clumping. Bij zulke hoge clumping waarden behaalde SCOPE geen goede resultaten. Het SLC model was wel in staat om goede resultaten in de vergelijking neer te zetten tot de op een na hoogste clumping factor. In dat scenario bleek de directionele reflectie een niet lineaire afhankelijkheid te krijgen met betrekking tot de zon azimut hoek.

Na de validatie is het SCOPE model gebruikt om de oppervlakte temperaturen van de verschillende componenten van het gewas te vinden. Om dit mogelijk te maken is een sensor simulator gemaakt om de straling van het SCOPE model om te zetten naar sensor observaties. Een sensitiviteitsanalyse toonde aan dat aard observaties die met een enkele observatie stand worden gemaakt niet gebruikt kunnen worden om de oppervlakte temperaturen van de gewas componenten te herleiden; hiervoor zijn meerdere observaties nodig die onder verschillende hoeken zijn gemaakt. Wanneer er gebruikt gemaakt wordt van deze observaties kunnen alle temperaturen van de vier componenten worden herleid. Het toepassen van dit algoritme op gemeten straling toonde ook aan dat de oppervlakte temperaturen van de gewas componenten te herleiden zijn.

Uiteindelijk is SCOPE gebruikt om het 'Surface Energy Balance System (SEBS)' verdampingsalgoritme te evalueren boven dicht en hoog gewas. Hierbij werd SCOPE gebruikt om zowel referentie metingen van verdamping te generen als aard observatie beelden. De vergelijking van de verschillende termen in de energie balans door het SEBS algoritme en het SCOPE model toonde aan dat het SEBS algoritme een te lage verdamping vind. Dit komt doordat de parameterizaties voor de ruwheid binnen het SEBS algoritme niet zijn ontwikkeld met oog op hoge en dichte vegetatie. Dit werd opgelost door het aanpassen van de parameterizaties

Hierna zijn de evaporative fracties van SEBS en SCOPE met elkaar vergeleken. Waar de evaporative fractie van SCOPE toenam gedurende de dag, word er in het SEBS algoritme aangenomen dat deze parameter stabiele is gedurende de dag. Doordat de grootste toename van de evaporative fractie vroeg in de ochtend plaats vind, en meeste satellieten over komen vliegen rond 10.30 bleek dit geen groot probleem.

It was a good run!

12 ITC Dissertation List

http://www.itc.nl/research/phd/phd_graduates.aspx